Cyclin J–CDK complexes limit innate immune responses by reducing proinflammatory changes in macrophage metabolism*

Yee Kien Chong[1]†, Sarang Tartey[1,8]†, Yuki Yoshikawa[2], Koshi Imami[2], Songling Li[3], Masanori Yoshinaga[1], Ai Hirabayashi[4], Guohao Liu[1], Alexis Vandenbon[5], Fabian Hia[1], Takuya Uehata[1], Takashi Mino[1], Yutaka Suzuki[6], Takeshi Noda[4], Dominique Ferrandon[7], Daron M. Standley[3], Yasushi Ishihama[2] and Osamu Takeuchi[1]*

[1]Department of Medical Chemistry, Graduate School of Medicine, Kyoto University, Kyoto, Japan
[2]Department of Molecular and Cellular BioAnalysis, Graduate School of Pharmaceutical Sciences, Kyoto University, Kyoto, Japan.
[3]Research Institute for Microbial Diseases, Osaka University, Suita, Japan
[4]Laboratory of Ultrastructural Virology, Institute for Frontier Life and Medical Sciences, Kyoto University, Kyoto, Japan
[5]Institute for Frontier Life and Medical Sciences, Kyoto University, Kyoto, Japan
[6]Department of Computational Biology and Medical Sciences, Graduate School of Frontier Sciences, The University of Tokyo, Chiba, Japan
[7]IBMC UPR 9022, CNRS, Strasbourg, France
[8]IGM Biosciences, Inc., CA, USA
*Corresponding author. Email: otake@mfour.med.kyoto-u.ac.jp
†These authors contributed equally to this work

Abstract

Toll-like receptor (TLR) stimulation induces glycolysis and the production of mitochondrial reactive oxygen species (ROS), both of which are critical for inflammatory responses in macrophages. Here, we demonstrated that cyclin J, a TLR-inducible member of the cyclin family, reduced cytokine production in macrophages by coordinately controlling glycolysis and mitochondrial functions. Cyclin J interacted with cyclin-dependent kinases (CDKs), which increased the phosphorylation of a subset of CDK substrates, including the transcription factor FoxK1 and the GTPase Drp1. Cyclin J–dependent phosphorylation of FoxK1 decreased the transcription of glycolytic genes and Hif-1α activation, whereas hyperactivation of Drp1 by cyclin J–dependent phosphorylation promoted mitochondrial fragmentation and impaired the production of mitochondrial ROS. In mice, cyclin J in macrophages limited the growth of tumor xenografts and protected against LPS-induced shock but increased the susceptibility to bacterial infection. Collectively, our findings indicate that cyclin J–CDK signaling promotes antitumor immunity and the resolution of inflammation by opposing the metabolic changes that drive inflammatory responses in macrophages.

Introduction

Macrophages are critical for inflammatory responses to microbial infection, resolution of inflammation, tissue regeneration, and modulation of tumor immunity through multiple pathogen sensors, such as Toll-like receptors (TLRs) (*1-4*). For instance, recognition of lipopolysaccharide (LPS) by TLR4 triggers intracellular signaling cascades that ultimately lead to transcriptional activation of myriad genes necessary for innate immune responses, including proinflammatory cytokines and chemokines. TLR signaling and other stimuli trigger a dynamic cellular metabolism shift from oxidative phosphorylation (OXPHOS) toward aerobic glycolysis (*5*), triggering events like cytosolic accumulation of citrate that aids efficient inflammatory mediator production by inducing epigenetic changes through ATP-citrate lyase (*6*). Furthermore, LPS-mediated succinate accumulation activates hypoxia-inducible factor-1 α (HIF-1α), an essential transcriptional factor for genes required for glycolysis as well as angiogenesis (*7-9*). LPS also reprograms mitochondria and serves an essential role in innate immune signaling in macrophages through the production of mitochondrial reactive oxygen species (mtROS) (*10-12*). These contemporaneous events require tight regulation, both transcriptionally and post-transcriptionally, in order to resolve activation and prevent excessive inflammation, which can have pathological consequences, such as septic shock and autoimmune diseases (*13*).

Cyclins are a family of more than 30 evolutionarily conserved proteins harboring cyclin box domains (CBDs) and known to bind to cyclin-dependent kinases (CDKs) (*14*). Beyond cell cycle regulation, cyclins and CDKs have been documented to play diverse tissue-specific roles in processes such as energy metabolism, spermatogenesis, apoptosis, cell differentiation, neuron homeostasis, viral replication, and immune regulation (*15-17*). Accumulating evidence has demonstrated that activated CDKs support inflammation by enhancing proinflammatory gene

induction through regulators such as nuclear factor κB (NF-κB) and the transcription factor AP-1 (*18, 19*). Also, cyclins and CDK promote interferon β (IFN-β) production through the regulation of translation machinery during immune activation or virus encounter (*20*). Such proinflammatory roles of cyclin-CDK signaling occur through the control of gene expression (*15-17*), suggesting that this is largely independent from their role in cell cycle regulation in macrophages and neutrophils. Because CDK functions largely depend on their cyclin partner for substrate recognition (*21, 22*), it is therefore reasonable to hypothesize that cyclins serve as *de facto* regulators of CDK activity in immune responses.

In this study, we provide findings on a TLR- and IFN-inducible atypical cyclin family member, cyclin J, that functions as a negative regulator of inflammatory responses in macrophages through its CDK-binding domains. Using phosphoproteomic analysis, we revealed that the immunoregulatory function of cyclin J was modulated by CDK-mediated phosphorylation of target substrates, including the transcription factor forkhead box protein K1 (FoxK1) and dynamin-related protein 1 (Drp1), which control glycolysis and mitochondrial dynamics, respectively. We also document that cyclin J was required for controlling tumor-associated macrophages (TAMs), thereby affecting tumor progression in vivo. These findings reveal an unexpected biological function of cyclin J in coordinately regulating macrophage metabolism, providing a new paradigm for cyclins and CDKs involved in immunity.

Results

Ccnj is a TLR- and IFN-inducible gene in macrophages

To evaluate how cyclins behave upon macrophage activation, we analyzed changes in the expression of genes encoding cyclins in LPS- or IL-4–stimulated murine bone marrow–derived macrophages (BMDMs) (GEO: GSE104641) (*23*) (Fig. 1A). Whereas IL-4 stimulation did not

alter the overall *cyclin* gene expression profile, LPS substantially reduced several transcripts for mitotic cyclins (*Ccna2*, *Ccne2*, and *Ccnd1*), consistent with the previous report that LPS suppresses cell cycling in macrophages (*24*). LPS stimulation induced the expression of other cyclin-encoding transcripts, such as *Ccnd2* and *Ccnj*. *Ccnd2* was previously shown to be induced by LPS in macrophages irrespective of its known function in cell cycle control (*25, 26*); however, there are no apparent reports of LPS-mediated induction of *Ccnj*, which encodes cyclin J. We confirmed that *Ccnj* was induced by LPS in primary murine macrophages and a murine macrophage cell line (RAW264.7), whereas its expression was not altered by other representative cytokines and mitogens (Fig. 1B and fig. S1A). Among TLR ligands, Poly (I:C), but not Pam_3CSK_4, increased *Ccnj* expression in a dose-dependent manner (fig. S1, B and C). Because MyD88 was dispensable for LPS-induced *Ccnj* expression (fig. S1, D and E), we asked if type I IFN signaling, a common pathway that can be triggered by LPS and Poly (I:C) in a manner that depends on the adaptor protein TRIF, could also induce *Ccnj*. IFN-α, but not IFN-γ, treatment induced *Ccnj* expression in both mouse and human macrophages (fig. S1, F to H). Unlike the expression of genes encoding mitotic cyclins in HeLa cells, the abundance of *Ccnj* mRNA did not fluctuate during cell cycle progression in RAW264.7 cells (fig. S1, I and J), suggesting that cyclin J is dispensable for cell cycle regulation in macrophages. Collectively, these data identified cyclin J as an atypical cyclin transcriptionally induced by TLR or type I IFN stimulation.

Cyclin J suppresses inflammatory responses in macrophages

To determine the potential function of cyclin J in macrophages, we generated RAW264.7 macrophages that stably express cyclin J using lentiviral transduction (fig. S2, A to C). Upon

LPS stimulation, macrophages stably expressing cyclin J exhibited suppressed expression of genes encoding proinflammatory cytokines compared to control cells, whereas the expression of *Il10*, which encodes an antiinflammatory cytokine, increased (Fig. 1C and fig. S2D). Consistent with this result, in cyclin J–expressing macrophages, LPS-induced production of IL-6 and IL-10 was suppressed and enhanced, respectively (Fig. 1D). Apart from proinflammatory genes, *Ifnb* and other IFN-stimulated genes (ISGs), such as *Cxcl10* and *Isg15*, were also suppressed in cyclin J–expressing macrophages when the cells were stimulated with LPS or Poly (I:C) (fig. S2, E and F). In contrast, cyclin J overexpression did not affect ISG induction in macrophages upon stimulation with type I and type II IFNs (fig. S2, G and H). These results demonstrate that cyclin J exerts a suppressive action on the induction of proinflammatory cytokine and type I IFN genes in macrophages in response to TLR stimulation.

We further investigated the role of cyclin J role in macrophages by generating myeloid cell–specific *Ccnj*-deficient (*Ccnj*$^{fl/fl}$LyzM-Cre^{+}) mice (fig. S3, A and B). Efficient depletion of *Ccnj* expression was observed in thioglycolate-elicited peritoneal macrophages (PMs), but not in lymphocytes from *Ccnj*$^{fl/fl}$LysM-Cre^{+} mice (Fig. 1E). Reciprocal to the observations made upon overexpression of cyclin J, *Ccnj*-deficient PMs and BMDMs showed enhanced expression of proinflammatory genes (*Il6*, *Ifnb,* and *Cxcl1*) upon LPS stimulation, whereas *Il10* expression was reduced in comparison to the wild-type (WT) counterparts (Fig. 1F and fig. S3C). The production of IL-6 and IL-12p40 was also induced in cyclin J–deficient macrophages in response to the TLR ligands LPS and Pam_3CSK_4 (Fig. 1G). In addition to macrophages, thioglycolate-elicited cyclin J–deficient peritoneal neutrophils also produced more IL-6 and less IL-10 in response to LPS and Pam_3CSK_4 (fig. S3, D and E). Notably, the proliferation of macrophages in response to a mitogen, macrophage colony-stimulating factor (M-CSF), was not altered in

myeloid cell–specific *Ccnj*-deficient mice (fig. S3F), nor was *Ccnj* induced in macrophages upon treatment with M-CSF (fig. S3G). These results demonstrate that cyclin J functions as a negative regulator of TLR-induced inflammatory responses, but not of mitosis, in macrophages.

Cyclin J suppresses glycolysis and mitochondrial ROS production in macrophages

We next asked how cyclin J negatively regulated inflammatory responses in macrophages. When we examined the LPS-triggered signaling cascades in both cyclin J–expressing RAW264.7 cells and cyclin J–deficient PMs, the activation of the mitogen-activates protein (MAP) kinases Jun N-terminal kinase (JNK) and p38 and the degradation of the NF-κB inhibitor IκBα were indistinguishable from those events in the control cells (fig. S4, A and B), suggesting that cyclin J suppressed TLR-mediated inflammatory responses independently of the canonical signaling pathways inducing nuclear translocation of transcription factors such as NF-κB and AP-1.

These results prompted us to investigate whether cyclin J mediates transcriptomic changes in macrophages. For this purpose, we performed RNA-sequencing (RNA-seq) analysis comparing control and cyclin J–expressing RAW264.7 cells (data file S1). Whereas 283 genes were differentially induced, 426 genes were suppressed in response to constitutive expression of cyclin J. Gene set enrichment analysis (GSEA) identified suppression of genes related to carbohydrate metabolism in cyclin J–expressing cells, particularly in glycolysis and hypoxia-related pathways (Fig. 2, A and B, and fig. S5A). We used RT-qPCR to validate the reduction in the expression of a set of genes encoding glycolytic enzymes (*Pgk1*, *Slc2a1*, *Hk2*, *Ldha*, *Pfkfb3*, *Pfkl*, and *Pkm2*) and the lack of change in cell cycle–related genes (*E2f1* and others) in macrophages constitutively expressing cyclin J (Fig. 2C). In agreement with the gene expression data, bioenergetics analysis confirmed a reduction in glycolysis, indicated by a decrease in

extracellular acidification rate (ECAR), in cyclin J–expressing macrophages (Fig. 2D). Consistent with this, we also observed a decrease in HIF-1α abundance in cyclin J–expressing macrophages and an increase in HIF-1α in cyclin J–deficient macrophages upon LPS stimulation (Fig. 2, E and F). This suggests that cyclin J could suppress LPS-induced glycolysis and HIF-1α activity.

Cyclin J expression also substantially reduced maximal respiratory capacity and spare respiratory capacity (Fig. 2, G and H). Given that the expression of genes involved in tricarboxylic acid (TCA) cycle and fatty acid oxidation (FAO) pathways was not affected by constitutive cyclin J expression (Fig. 2A), we hypothesized that cyclin J might alter macrophage mitochondrial activity irrespective of metabolic changes. We observed a mild reduction in mitochondrial membrane potential ($m\Delta\psi$) (Fig. 2I) and a slight decrease in ATP production in cyclin J–expressing macrophages despite no changes in mitochondrial biogenesis, as measured by mtDNA copy number (fig. S5, B and C). Given changes in $m\Delta\psi$ are closely related to the production of mtROS, we measured LPS-induced production of mtROS and cellular ROS in these cells by MitoSox and dichlorodihydrofluorescein diacetate (DCFDA), respectively. Cyclin J expression in macrophages decreased both mitochondrial and cytoplasmic ROS production in LPS-treated macrophages, without affecting the expression of genes encoding key antioxidant enzymes (Fig. 2, J and K, and fig. S5D). Collectively, these results suggest that cyclin J limits macrophage activation by suppressing glycolysis and mitochondrial ROS production.

Cyclin J associates with CDK to suppress inflammatory gene expression

Cyclin J is highly similar to typical mitotic cyclins with the presence of two CBDs, referred to as the N-terminal domain (NTD) and C-terminal domain (CTD), although it lacks a destruction box

(D-box), a mitotic cyclin interacting domain (MRAIL), and a nuclear localization signal (NLS) (Fig. 3A) (*27*). To further investigate the molecular mechanism by which cyclin J affects macrophage metabolism and inflammatory responses, we sought to identify protein(s) that coimmunoprecipitated with Flag-tagged cyclin J from HEK293T and HeLa cells using mass spectrometry. We identified a group of CDK proteins as the top interactors of cyclin J (Fig. 3B and Table S1). Cyclin J was able to bind CDK2 as efficiently as the known CDK2 interactor cyclin A2 (Fig. 3C). Other CDKs, including CDK3 and CDK5 but not CDK1, also coimmunoprecipitated with cyclin J (Fig. 3D and fig. S6A). The cyclin J–CDK interaction was not influenced by CDK kinase activity, as demonstrated by using dominant negative (DN) constructs in coimmunoprecipitation experiments (fig. S6A). We further examined cyclin J binding to CDK2 by co-expressing CDK2 with forms of cyclin J in which one of both of the CBD domains were deleted in HEK293T cells, which revealed that both the NTD and the CTD were critical for interaction with CDK2 (Fig. 3, E and F). We tested the effect of deleting the CBDs of cyclin J on inflammatory gene expression in RAW264.7 macrophages upon LPS stimulation. Macrophages expressing cyclin J lacking CBDs failed to alter inflammatory gene expression upon LPS stimulation compared to cells expressing full-length cyclin J (Fig. 3G), indicating that the CBDs of cyclin J are required for both its interaction with CDK and its immunoregulatory function in macrophages.

Previous studies of cyclins harboring two CBDs have shown that the NTD is mainly responsible for binding and activation of CDKs, whereas the CTD stabilizes the overall cyclin-CDK interaction (*28*). An immunofluorescence assay revealed that cyclin J is located in both the nucleus and cytoplasm, and the NTD is critical for its nuclear localization (fig. S6B). By structural modeling of mouse cyclin J and template-based docking to CDK2, we predicted that

cyclin J associates with CDK2 through conserved amino acids in the NTD (Fig. 3H). The NTD amino acid residues Asp^{15}, Lys^{95}, Phe^{96}, Glu^{97}, Glu^{98}, Leu106, Glu^{131}, Glu^{132}, and Trp^{140} were closely aligned to CDK2 in the model, with residues Lys^{95} to Glu^{98} containing a conserved lysine-glutamate pair motif (KxEE) that would be essential for the interaction (fig. S6C) (*29*). Consistent with this hypothesis, a point mutation in the KxEE sequence in the NTD (K95R) disrupted the cyclin J–CDK interaction in HEK293T cells (Fig. 3, I and J). Given that the cyclin J CTD is not predicted to directly interact with CDK2, we assumed that the CTD supports the cyclin J–CDK2 interaction indirectly by stabilizing the NTD fold. Together, these results clearly show that the cyclin J–CDK interaction is essential for regulating immune responses in LPS-activated macrophages.

The cyclin J–CDK interaction in macrophage induces phosphorylation of a set of CDK substrates

Cyclins binds CDKs and activate their kinase activities, thus promoting phosphorylation of CDK target substrates. We therefore explored if CDKs were activated in response to TLR4 signaling. Immunoblot analysis revealed an increase in CDK target phosphorylation over time after LPS activation of BMDMs (Fig. 4A). We further observed that constitutive expression of cyclin J in RAW264.7 macrophages enhanced the global phosphorylation of CDK substrates, as revealed by immunoblotting using two distinct antibodies recognizing phosphorylated CDK substrates (Fig. 4B). We then examined the effect of short-term cyclin J induction on CDK substrate phosphorylation by generating doxycycline (DOX)-inducible cyclin J–expressing RAW264.7 macrophages (Fig. 4, C and D). In agreement with the results from cells constitutively expressing cyclin J, DOX-mediated induction of cyclin J augmented the phosphorylation of CDK substrates

(Fig. 4E), suggesting that cyclin J directly controls CDK activity and promotes the phosphorylation of CDK substrates.

These findings prompted us to perform quantitative proteomic and phosphoproteomic analyses to identify CDK substrates whose phosphorylation was induced by cyclin J in macrophages and potentially exhibited immunoregulatory functions. We first verified our experimental design using nocodazole to arrest macrophages followed by treatment with chemical CDK inhibitors, flavopiridol (FVP) and roscovitine (ROS), to release the cells from mitotic arrest (fig. S7A). The synchronization induced global changes in phosphorylated CDK substrates that were suppressed by CDK inhibitors, as confirmed by immunoblotting (fig. S7B). The phosphopeptides whose expression increased upon Nocodazole treatment or decreased upon CDK inhibitor treatment included canonical CDK consensus motifs (pS/T-P-X-R/K) (fig. S7, C to E, and data file S2), indicating that the phosphoproteomic analysis properly captured the phosphorylation of CDK substrates.

We next performed proteomic and phosphoprotemic analyses using macrophages harboring DOX-inducible cyclin J (Fig. 4F). The proteome in DOX-treated macrophages was globally stable with cyclin J induction (Fig. 4G and data file S3). By contrast, comparative phosphoproteomes quantified 7662 unique phosphopeptides, of which 6115 were confirmed with high-confidence phosphorylation localization in cyclin J–expressing cells (Fig. 4H and data file S4). Among them, we found 61 phosphosites that were differentially increased in phosphorylation state upon cyclin J induction ($Log_2FC > 0.5$, p-value < 0.05), of which 27 (44.3%) contained canonical CDK substrate motifs (pS/T-P-X-R/K) that were highly enriched in motif analysis (Fig. 4I). The 27 proteins potentially phosphorylated by CDK in a cyclin J–dependent manner included transcriptional regulators (FoxK1, Nfat5, and Runx1) and proteins

that have organelle-specific functions, such as functions in the mitochondria (Drp1, also known as DNM1L) and Golgi apparatus (Gors2, Goga5), together with various uncharacterized proteins. Collectively, by the phosphoproteomic approach, we identified a set of candidate J–dependent CDK substrates in macrophages.

Cyclin J suppresses glycolysis and mitochondrial ROS production through FoxK1 and Drp1 phosphorylation, respectively

We hypothesized that cyclin J controls macrophage metabolic status and inflammatory responses depending on the phosphorylation of specific CDK substrates. Thus, we first checked if proteins with transcriptional regulation or organ-specific functions were involved in TLR-induced cytokine gene expression by generating stable knockdown RAW264.7 cells. Among the transcriptional regulators, we focused on FoxK1 and Nfat5, because a previous report showed that Runx1 is involved in the growth and survival of macrophages (*30*), which is distinct from the function of cyclin J. Although the cellular functions of Gors2 and Goga5 have not been clarified, we knocked down Gors2 as a representative protein localized to the Golgi apparatus. Whereas the knockdown (KD) of Nfat5 or Gors2 in RAW264.7 cells did not affect the expression of *Il6* and *Ifnb* in response to LPS stimulation, the reduction of FoxK1 or Drp1 substantially altered cytokine gene expression: FoxK1 KD suppressed and Drp1 KD increased them (Fig. 4J and fig. S8).

FoxK1 is a member of the K family of forkhead transcription factors known to induce aerobic glycolysis by increasing the expression genes encoding glycolytic enzymes (*31*), with its transcriptional activity being tightly regulated by phosphorylation at multiple sites that control its shuttling between the cytoplasm and nucleus (*32, 33*). In our phosphoproteomic analysis, cyclin J

preferentially phosphorylated FoxK1 at two previously uncharacterized sites, Ser^{199} and Ser^{209} (fig. S9, A and B). Whereas FoxK1 localized to both the nucleus and cytoplasm in control RAW264.7 macrophages, constitutive or inducible expression of cyclin J caused it to predominantly localize to the cytoplasm with no changes in its overall abundance (Fig. 5A and fig. S9C). To investigate if FoxK1 localization was affected by phosphorylation of Ser^{199} or Ser^{209}, we generated a mutant FoxK1 construct in which both residues were mutated (S199A and S209A). Although cyclin J overexpression inhibited the nuclear localization of WT FoxK1, it did not prevent the mutant form of FoxK1 from entering the nucleus in HEK293T cells (fig. S9D). Furthermore, LPS induced FoxK1 nuclear translocation in RAW264.7 macrophages (fig. S9E), and this was disrupted by cyclin J expression (Fig. 5B). These results demonstrate that cyclin J inhibits the nuclear translocation of FoxK1 by promoting its phosphorylation at Ser^{199} and/or Ser^{209}.

Given that glycolysis is critical in shaping macrophage immune responses, we hypothesized that cyclin J could reduce inflammation through a FoxK1-mediated glycolytic pathway. In addition to *Il6* and *Ifnb* (Fig. 4J), FoxK1 KD in RAW264.7 macrophages reduced the magnitude of the LPS-induced increase in *Il1b*, *Il23a* and *Cxcl10* expression (Fig. 5C). Furthermore, FoxK1 KD suppressed the increase in HIF-1α at both the protein and transcript levels in response to LPS (Fig. 5D and fig. S9F) and impaired the induction of HIF-1α target genes such as *Vegfa* and *Glut1* upon LPS stimulation (fig. S9G). However, cyclin J expression in FoxK1 KD RAW264.7 macrophages failed to further suppress *Il6* expression upon LPS treatment, implying that cyclin J functions upstream of FoxK1 in controlling inflammation (Fig. 5E and fig. S9H). Collectively, these results suggest that phosphorylation of FoxK1 by cyclin J–

CDK in response to TLR stimulation induces FoxK1 cytoplasmic translocation, thereby inhibiting its capacity to stimulate glycolysis and HIF-1α activity.

We also identified the cytosolic GTPase Drp1, encoded by the *dnm1l* gene, as one of substrates phosphorylated by cyclin J–CDK at evolutionally conserved amino acids Ser^{616} (corresponding to Ser^{622} in the human homolog) (fig. S10A). Drp1 is essential for regulating mitochondrial dynamics because it induces mitochondrial fission (*34*). The function of Drp1 is known to be regulated by phosphorylation, and the phosphorylation of Ser^{616} is primarily responsible for driving mitochondrial fission (*35*)**.** We confirmed that cyclin J expression induced phosphorylation of Drp1 at Ser^{616} in RAW264.7 and HEK293T cells by immunoblotting and that the phosphorylation required intact CBDs in cyclin J (fig. S10, B and C). Drp1 KD RAW264.7 macrophages displayed more elongated and filamentous mitochondria with high network interconnectivity, confirmed with both immunofluorescence and electron microscopy (Fig. 5F and fig. S10D). Drp1 KD macrophages also displayed increased respiration (fig. S10, E and F) and produced more mtROS and cellular ROS upon LPS stimulation (Fig. 5, G and H), reciprocal to the mitochondrial changes observed in cyclin J–expressing cells (Fig. 2). Consistent with the increase in ROS, the reduction of Drp1 in macrophages enhanced LPS-induced expression various pro-inflammatory cytokine genes, including *Il6* (Fig. 5I and fig. S10G), and increased HIF-1α abundance compared with control cells (Fig. 5J). Furthermore, cyclin J expression did not alter the increase in LPS-induced cytokine expression due to Drp1 KD (Fig. 5K and fig. S9H), suggesting that cyclin J also functions upstream of Drp1. We also observed that mitochondria in cyclin J–expressing macrophages were more fragmented and isolated, consistent with Drp1 activating mitochondrial fission in these cells (Fig. 5L and fig. S10H). These results suggest that cyclin J reduces inflammatory responses in macrophages by

concurrently suppressing glycolysis and mitochondrial functionality through the phosphorylation of FoxK1 and Drp1, respectively.

Macrophage cyclin J negatively regulates inflammation and antibacterial host defense in vivo

To address the functional roles of cyclin J in mediating macrophage functionality in vivo, we first studied the sepsis response elicited by LPS in mice (Fig. 6A). Mice lacking cyclin J in the myeloid lineage (*Ccnj*$^{fl/fl}$LyzM-Cre^{+}) mice were highly susceptible to LPS shock, with decreased survival rate compared to control *Ccnj*$^{fl/fl}$ mice (Fig. 6B). Proinflammatory cytokines were increased in serum collected from LPS-treated *Ccnj*$^{fl/fl}$LyzM-Cre^{+} mice compared to their *Ccnj*$^{fl/fl}$ counterparts (Fig. 6C), confirming that cyclin J in macrophages prevents excess LPS-induced inflammatory responses in vivo.

We also analyzed the function of macrophage cyclin J in host defense to systematic inoculation with the extracellular pathogen *Staphylococcus aureus* (Fig. 6D). Under these conditions, *Ccnj*$^{fl/fl}$LyzM-Cre^{+} mice were protected against systemic *S. aureus* bacterial infection, with lower fatality post-infection compared to *Ccnj*$^{fl/fl}$ mice (Fig. 6E). Indeed, the production of proinflammatory cytokines such as IL-6 and IL-12p40 were increased in serum collected from *Ccnj*$^{fl/fl}$LyzM-Cre^{+} mice compared to control animals (Fig. 6F). Consistent with enhanced protection from *S. aureus* infection, the bacterial burden in multiple organs (liver, spleen, and kidney) decreased in mice lacking cyclin J in myeloid cells (Fig. 6G). These results show that cyclin J in macrophages is critical for controlling innate immune responses against infection in vivo by preventing overt and potentially fatal inflammation.

Involvement of macrophage Cyclin J in restricting tumor progression

The metabolic status of macrophages is influenced by external conditions. Tumor-associated macrophages (TAMs) are heterogeneous and exert diverse effects on tumorigenesis and tumor progression in the hypoxic and acidic tumor microenvironment, and TAMs generally support tumor progression in part through the production of angiogenic factors in a manner that depends on the activation of HIF-1α (*36*-*38*). These features of TAMs prompted us to examine the expression of *Ccnj* in TAMs using a MC38 colorectal tumor xenograft mouse model. Isolated TAMs expressed a lower amount of *Ccnj* transcripts in comparison with BMDMs or PMs (fig S11, A and B). Because our evidence substantiated a role for cyclin J in reducing macrophage-mediated immune responses, we asked whether cyclin J in TAMs modulated tumor progression by performing a tumor xenograft model (fig. S11C). Following syngeneic MC38 tumor xenograft, *Ccnj*$^{fl/fl}$LyzM-Cre^{+} mice displayed faster tumor growth and bore larger tumors than control littermates (Fig. 7A). Similarly, cyclin J deficiency in macrophages allowed more rapid growth of B16-F10 melanoma tumor xenografts (Fig. 7B). We further utilized the azoxymethane -dextran sodium sulfate (AOM-DSS) mouse model of Colitis-associated cancer (CAC) to investigate whether cyclin J deficiency in macrophages promotes inflammation-mediated endogenous tumor progression (fig. S11D). *Ccnj*$^{fl/fl}$LyzM-Cre^{+} mice lost more body weight relative to control mice (fig. S11E), and, at the send of the experimental course, had a greater tumor burden in the colon in comparison to the controls (fig. S11, F and G). Taken together, these results demonstrate that cyclin J in macrophages is important for slowing tumor progression.

We next investigated how cyclin J in TAMs suppresses tumor progression. Although the proportion of $CD45^+$ immune cells in the MC38 tumor preparations was comparable between control and *Ccnj*$^{fl/fl}$LyzM-Cre^+ mice despite differences in tumor size (Fig. 7C), the abundance of $F4/80^+CD11b^+$ TAMs was increased in *Ccnj*$^{fl/fl}$LyzM-Cre^+ mice compared to controls (Fig. 7, D and E). In contrast, other immune subsets such as T cells, natural killer (NK) cells, natural killer T (NKT) cells, and neutrophils were not altered. Despite the increase in the TAM population, the proportions of $Ki67^+$ TAMs were comparable between control and *Ccnj*$^{fl/fl}$LyzM-Cre^+ mice (fig. S11H), suggesting that cyclin J controls recruitment, but not proliferation, of TAMs. Because cyclin J is deleted only in macrophages and neutrophils in *Ccnj*$^{fl/fl}$LyzM-Cre^+ mice, the increased tumor burden in *Ccnj*$^{fl/fl}$LyzM-Cre^+ mice might be solely due to the change in TAM functionality. In addition to the increased population of TAMs, isolated TAMs from *Ccnj*$^{fl/fl}$LyzM-Cre^+ mice showed increased expression of immunosuppressive genes such as *Fizz1*, *Mgl1*, *Mgl2*, and *Arg1* (Fig. 7F). We also observed increased expression of genes encoding protumorigenic cytokines such as *Il23a* and *Vegfa* in *Ccnj*$^{fl/fl}$LyzM-Cre^+ TAMs. To further understand how cyclin J affects TAMs in the global genomic landscape, we conducted RNA-seq analysis on isolated TAMs. We identified 485 differentially expressed genes (DEGs) (FC $\geq$1.75, $P_{adj} \leq$0.001) in *Ccnj*$^{fl/fl}$LyzM-Cre^+ TAMs in comparison to control TAMs, wherein 183 genes showed enhanced expression and 302 genes were suppressed (Fig. 7G and data file S5). GSEA also revealed that the gene sets for glycolysis and hypoxia were highly enriched in *Ccnj*$^{fl/fl}$LyzM-Cre^+ TAMs (Fig. 7H), which is consistent with cyclin J suppressing glycolysis and HIF-1α activation. Furthermore, we observed increased transcripts of HIF-1α targets in RNA-seq analysis, of which some are related to glycolysis and hypoxia such as *Hk2* and *Slc2a1* (Glut1) (fig. S11, I and J). We confirmed an increase in intracellular Glut1 abundance in *Ccnj*$^{fl/fl}$LyzM-

Cre^+ TAMs compared to control TAMs (Fig. 7I). Collectively, these results suggest a critical role for cyclin J–mediated metabolic control in governing TAM homeostasis, which potentially inhibits tumor progression.

Discussion

Cyclin J was initially discovered as a CDK interactor in *Drosophila melanogaster* using a yeast two-hybrid screen (*27*). Like other cyclin proteins, cyclin J is highly evolutionally conserved. Cyclin J is expressed in early *Drosophila* embryos, and it is essential for mediating intestinal epithelial cell recovery from bacterial pore-forming toxin attack in both *Drosophila* and mice (*39*). In this study, we clarified the role of cyclin J in regulating the macrophage immune response (Fig. 8). Upon TLR and IFN stimulation, cyclin J restrained macrophage inflammatory responses irrespective of the cell cycle control or the general promotion of gene transcription. Cyclin J interacted with CDKs and facilitated the phosphorylation of a set of CDK substrates, including FoxK1 and Drp1. Phosphorylation inhibited FoxK1-mediated expression of glycolytic genes by reducing FoxK1 nuclear localization. Cyclin J–CDK-dependent Drp1 phosphorylation also resulted in mitochondrial fission and the suppression of ROS production. Thus, cyclin J coordinately controls metabolism and thereby suppresses inflammatory responses in macrophages.

Even in their roles in regulating cell proliferation, cyclin and CDKs contribute to the control of cellular metabolism. One example is direct phosphorylation and inhibition of glycolytic enzymes such as 6-phosphofructokinase and pyruvate kinase M2 by cyclin D3-CDK6 in human cancer cells (*40*). In contrast, CDK4 is reported to inhibit AMP-activated protein kinase (AMPK) in mouse embryonic fibroblasts through direct phosphorylation, thereby

enabling CDK4 to promote glycolysis (*41, 42*). In hepatocytes, CDK4, together with cyclin D1, increase GCN5 acetyltransferase activity through phosphorylation and suppress hepatic glucose production (*41*). In the present study, we identified FoxK1, but not enzymes involved in glycolysis, as phosphoproteins differentially phosphorylated by the presence of cyclin J. Because FoxK1 is a transcription factor critical for the expression of glycolytic genes as well as *hif1a (43)*, the role of cyclin J is to indirectly control cellular metabolic status. Consistent with this, cyclin J suppressed *hif1a* expression and the accumulation of HIF-1α, suggesting that cyclin J–mediated suppression of HIF-1α contributes to the regulation of the expression of cytokine genes in macrophages.

We found FoxK1 as a target of cyclin J–CDK–mediated phosphorylation at two phosphosites (Ser^{199} and Ser^{209}) and observed that this phosphorylation localized FoxK1 to the cytoplasm. FoxK1 is also reported to be phosphorylated by glycogen synthase kinase 3 (GSK3) at distinct phosphosites (Ser^{402} and Ser^{406}), and this phosphorylation is also critical for regulating nuclear localization (*43, 44*). Downstream of insulin signaling, GSK3 kinase activity was suppressed by the Akt-mechanistic target of rapamycin (mTOR) pathway, enhancing the transcriptional role of FoxK1. Thus, FoxK1 transcriptional activity is suggested to be regulated by phosphorylation of multiple sites by distinct kinases depending on the external stimuli. Notably, we did not detect any change in the phosphorylation of mTOR target proteins (AKT1S1, RPS6, EIF4EBP1, EIF4EBP2, and MDM2) by the expression of cyclin J. Nevertheless, it will be intriguing to further investigate the relationship between cyclin J–CDK and other kinases in the regulation of FoxK1.

Metabolic adaptation involves a dynamic cellular adjustment during macrophage activation in order to support associated immune responses (*45*). Of particular interest,

mitochondria have emerged as a critical component instrumental to immunometabolism regulation; therefore disruption of mitochondrial integrity may deeply impact cellular processes including ion homeostasis, oxidative metabolism, and cytokine production in macrophages upon activation (*46*). Drp1 is a GTPase that maintains mitochondrial homeostasis by regulating mitochondrial fission events, and has been identified as playing a crucial role in controlling macrophage and T cell homeostasis by regulating migration, proliferation, and metabolic rewiring (*47, 48*). In this study, we observed notable changes in mitochondrial fitness upon cyclin J overexpression, including extended fragmentation and reduced $m\Delta\psi$. These phenomena were potentially attributed to Drp1 hyperactivation driven by cyclin J–CDK–mediated phosphorylation. Such altered mitochondrial functionality led to changes in the production of mtROS, a result of partial reduction of molecular oxygen due to electron leakage, subsequently hampering immune responses in macrophages. mtROS is required in activated macrophages for bacteria-killing responses by activating downstream transcriptional programs including supporting production of anti-bacterial micropeptides and assisting phagocytosis (*11*). Our findings are in agreement with reported increases in mitochondrial fragmentation leading to impairment in mtROS production in macrophages upon LPS stimulation, thereby substantially affecting macrophage function against pathogens and cancerous cells (*49, 50*), shedding light on the link between mitochondria morphology and macrophage inflammatory responses.

Mice lacking cyclin J in myeloid cells were more resistant to *S. aureus* infection as compared to control mice, although they succumbed to LPS-induced shock due to high pro-inflammatory cytokine production. Cyclin J was also important in restraining the protumorigenic activities of macrophages in vivo: TAMs lacking cyclin J promoted tumorigenesis in xenograft and spontaneous intestinal tumor models. TAMs are suggested to be generally protumorigenic,

and, the absence of cyclin J in TAMs enhanced their protumor activity by increasing the expression of glycolytic genes as well as both M1 and M2 type macrophage markers such as *Il23a*, *Arg1*, and *Vegfa* . Furthermore, genes involved in glycolysis and hypoxia were highly enriched in cyclin J–deficient TAMs, suggesting that cyclin J controls HIF-1α activity in TAMs, too. Indeed, HIF-1α in macrophages is reported to promote tumor progression by suppressing T cell function (*51*). These results demonstrate that cyclin J acts as a rheostat determining the strength of antibacterial and antitumor immunity in macrophages. Notably, *Ccnj* expression was lower in TAMs compared to BMDMs or PMs. Therefore, cyclin J modulation in macrophages or TAMs might by a potential therapeutic target for regulating infectious diseases or anticancer immunity, respectively.

In summary, we provide a new perspective of cyclin-CDK–mediated immunoregulation by identifying a role for cyclin J in controlling macrophage function through immunometabolism. Our evidence showed that global inhibition or activation of CDKs can broadly affect cellular functions such as cell cycling and transcription in addition to the immunoregulation. Therefore, these findings provide a new perspective for the potential development of therapeutic approaches using small molecules targeting cyclin-mediated modulation of CDK activity in macrophages for the control of both infectious diseases and tumor progression.

Materials and Methods

Study design

The aim of this study was to investigate the role of cyclin J in mediating macrophages inflammation and anti-tumor activity. We used both cyclin J expressing macrophage and

myeloid-specific cyclin J deficient mouse with in vitro stimulation assays and multiple in vivo models to determine if cyclin J exhibit potential immune regulation function on macrophages. The mechanism on how cyclin J modulate inflammation in macrophage was further examined using multiple approaches, including mass spectrometry, RNA-sequencing, and phosphoproteomic analysis. We also performed metabolic seahorse analysis, immunofluorescent assays and flow cytometry to illuminate how cyclin J target respective substrate via phosphorylation and affect immuno-metabolic status of macrophage.

Molecular cloning of related genes

The genes studied in this paper were obtained from mouse macrophage cDNA through RT-PCR and were subsequently cloned into respective target vectors using In-Fusion® HD Cloning Kit (Takara Bio USA, Inc.). Each construct was confirmed by sequencing. Mutagenesis was performed using QuickChange Lightning Site-Directed Mutagenesis Kit (Agilent Technologies). All the following vectors were obtained from Addgene.

Reagents and Antibodies

Recombinant Mouse IFN-α, IFN-γ, IFN-β, and M-CSF were purchased from BioLegend. LPS (LPS-SM), Pam_3CSK_4, Poly (I:C), R848, D-(+)-Glucose (Glu), Blasticidin and Puromycin were purchased from InvivoGen. Propodium Iodide was from Nacalai Tesque, Japan. Mouse GM-CSF, IL-10, and IL-6 were purchased from R&D Systems. Collegenase D, Complete Mini (EDTA-free), DNase I and PhoSTOP were purchased from Roche. Azoxymethane, Flavopiridol HCl (FVP), Oligomycin (OM), 2-Deoxy- D -glucose (2-DG), Roscovitine (ROS), Thymidine,

Nocodazole (NOC), FCCP, Doxyxycline hyclate (DOX), Rotenone (Rot) and Antimycin A (AA) were obtained from Sigma-Aldrich. Hoechst 33258, Pentahydrate was purchased from Invitrogen™. Lipofectamine™ 2000 and Lipofectamine™ LTX, MitoSpy™ NIR DiIC1(5), MitoSpy™ Green FM, MitoSpy™ Red CMXRos, MitoSOX™ Red Mitochondrial Superoxide Indicator and H2DCFDA (DC-FDA) were obtained from Thermo Fisher Scientific (Waltham). Ammonium bicarbonate, sodium deoxycholate (SDC), sodium N-lauroylsarcosinate (SLS), tris(hydroxymethyl)aminomethane, dithiothreitol (DTT), iodoacetamide (IAA), lysyl endopeptidase (Lys-C), lactic acid, piperidine, ethyl acetate, acetonitrile (ACN), acetic acid, methanol and trifluoroacetic acid (TFA) were obtained from FUJIFILM Wako. Protease inhibitor cocktail and phosphatase inhibitor cocktail 2 and 3 were obtained from Sigma-Aldrich. BCA protein assay kit and Tandem mass tag (TMT) reagents were obtained from Thermo Fisher Scientific. Trypsin was obtained from Promega. Titanium dioxide particle (10 μm diameter) and SDB-XC Empore disks were obtained from GL Sciences.

The following antibodies were used for immunoblot, co-immunoprecipitation and Immunofluorescence: Mouse anti-FLAG M2 (F1804, Sigma-Aldrich), Mouse anti-Myc (SAB4700447, Sigma-Aldrich), Rabbit anti-HA (H6908, Sigma-Aldrich), Rabbit anti-FLAG (F2225, Sigma-Aldrich), Rabbit anti-Myc (SAB4301136, Sigma-Aldrich), Rabbit anti-RB (D20, CST), Rabbit anti-phospho-RB (S780, CST), Rabbit anti-phospho MAPK/CDK substrate (2325, CST), Rabbit anti-phospho CDK substrate (9477, CST), Rabbit anti- HIF-1α (GTX127309, GeneTex), Rabbit anti-FOXK1 (ab18196, Abcam), Rabbit anti-mouse Drp1 (CST), Rabbit anti-phospho-Drp1 (S616, CST), Rabbit anti-phospho-SAPK/JNK (T183/185) (CST), Rabbit anti-JNK (C-17, Santa Cruz), Rabbit anti-phospho-p38 MAPK (T180/182) (CST), Rabbit anti-p38 MAPK (C-20, Santa Cruz), Rabbit anti-IκBα (C-21, Santa Cruz), Chicken anti-β-actin HRP

(C4,sc-47778, Santa Cruz), Goat anti-Laminin B (C20,sc-6216, Santa Cruz), Rabbit anti-α/β Tubulin (2148, CST), Alexa Fluor 488 F(ab')2 fragment of goat anti-mouse IgG (H+L) (Invitrogen), Alexa Fluor 488 F(ab')2 fragment of goat anti-rabbit IgG (H+L (Invitrogen)), Alexa Fluor 568 F(ab')2 fragment of goat anti-mouse IgG (H+L) (Invitrogen), Alexa Fluor 568 F(ab')2 fragment of goat anti-rabbit IgG (H+L) (Invitrogen).

For FACS analysis, fluorescent-conjugated antibodies against F4/80 (BM8), CD11b (M1/70), CD3e (145-2C11), CD4 (GK1.5), CD49b (DX45), CD8a (53-6/7), CD45R/B220 (RA3-6B2), CD45.2 (104), Gr1 (RB6-8C5), Ly-6C (HK1.4), Ly-6G (1A8), Ki-67 (16A8), CD11c (N418) and Thy1.1 (OX-7) were purchased from BioLegend. Recombinant PE Anti-Glucose Transporter GLUT1 antibody [EPR3915] (ab209449) was purchased from Abcam.

Cells

B16-F10 melanoma and Murine MC38 colon adenocarcinoma cell lines were kindly provided by Dr. M Jinushi (Hokkaido University, Japan), and originally obtained from the American Tissue Culture Collection (ATCC) and Kerafast, respectively. B16-F10 and RAW264.7 were cultured in RPMI1640 supplemented with 10% fetal bovine serum (FBS), 100U/mL penicillin, 100 µg/mL streptomycin (Nacalai Tesque), and 50 µM 2-mercaptoethanol, while MC38, HEK293T, and HeLa cells were cultured in Dulbecco's modified Eagle's medium (DMEM) supplemented with 10% FBS, 100 U/mL penicillin, 100 µg/mL streptomycin, and 50 µM 2-mercaptoethanol. All cells were maintained in a humidified, 5% CO_2 incubator at 37^0C. All cell lines were tested for mycoplasma contamination.

Peritoneal exudate cells were collected from the peritoneal cavities of mice 6 hours (neutrophils) or 3 days (macrophages) post intra-peritoneal (i.p.) injection with 2 ml of 4.0% Brewer's

thioglycolate medium (Sigma-Aldrich) by washing with ice-cold Dulbecco's Phosphate-Buffered Saline (Nacalai Tesque). BMDMs were obtained by harvesting mouse bone marrow cells from tibia and femur, and culturing in RPMI1640 containing 10% FBS, 100 U/mL penicillin, 100 μg/mL streptomycin, 50 μM 2-mercaptoethanol and 20 ng/mL M-CSF (BioLegend) for 7 days. After differentiation, BMDMs were harvested and re-seeded for subsequent in vitro experiment. Cell suspensions from spleen, kidney and lung were prepared through smashing using frosted glass slides and filtered through 70 μm cell strainer (Falcon) for subsequent analyses.

Mice

Cyclin J floxed mice were generated using gene-targeting vector construct by two loxP sites between exon 3 of the *Ccnj* gene, and loxP site-flanked *neo*^{r} gene into intron 2 of the *Ccnj* gene. The targeted embryonic stem (ES) cells were transiently transfected with a plasmid encoding the *Cre* gene to excise the *neo*^{r} gene. The successful clones were injected into blastocytes derived from C57BL/6 mice and transferred to pseudo-pregnant females. Mating of chimeric male mice to C57BL/6 female mice resulted in the transmission of the floxed allele to the germline. Myeloid-specific *Ccnj*-deficient mice were generated by crossing *Ccnj* floxed mice with LyzM-Cre mice (*52*). *MyD88*$^{-/-}$ mice were obtained from Oriental Bioservice. Mice were housed in specific-pathogen-free conditions, and all animal experiments were done using 6 to 8 weeks old mice with the approval of the Animal Research Committee of the Research Institute of Kyoto University.

LPS shock induction

Mice were injected i.p. with 500 µg LPS (*Escherichia coli* O111:B4, Invivogen). Survival was monitored for extended time. Sera were collected at 0, 1, 3 and 6 hours after LPS injection and subjected to ELISA for TNF, IL-6, and IL-12p40 (R&D System) according to manufacturer's instructions.

Infection model with *Staphylococcus aureus*

Mice were infected with S. aureus [5 x 10^7 colony forming unit (c.f.u)/head] and the survival rate was monitored for 2 weeks. To measure cytokine production, sera were collected at 0, 24, 36 and 48 hours after infection and subjected to ELISA for TNF, IL-6, and IL-12p40 (R&D System) according to manufacturer's instruction. For infectivity measurement, 0.2 mL of S. aureus (3 x 10^7 c.f.u) were injected intravenously into mice. Liver, spleen and kidney were harvested at day 2 and day 4 post infection. These organs were perfused with 0.1% Triton-X100 and homogenous suspension was prepared. Appropriate dilutions were made and 50 µL of suspension was plated onto Tryptic Soy Agar plates. Plates were incubated at 37^0C for 12-16 hours and colonies were counted.

Colitis-associated Carcinogenesis (CAC) model

The AOM-DSS model for colorectal tumorigenesis has been described previously (*53*). Briefly, 8-week-old mice were injected intraperitoneally with a single dose of 10 mg/kg AOM (Sigma) in sterile 0.9% saline and maintained on a regular diet and water for 5 days. Then, 2.0% DSS (MW 36-40 kDa; MP Biologicals) was given in drinking water over a 5-day period followed by regular drinking water for 2 weeks and subjected to two more DSS treatment cycles. The clinical course

of the disease was followed daily by measurement of body weight. At day 80, mice were sacrificed, colons were removed and flushed with PBS for subsequent analysis.

Tumor xenograft models

MC38 and B16-F10 cells were injected subcutaneously into the flanks of mice of 6 to 8 weeks of age (1×10^6 cells per injection in 100 µL PBS). Tumor volume was determined by measuring the length and width of the tumor with a caliper, and calculated by (Length x Width^2) x 1/2. The mice were euthanized on indicated days. Tumors were resected and transferred to 5 mL PBS on ice. Tumor weight was measured on a scale by transferring the specimen to a sterile Petri dish after removal of surface moisture with Kimwipes. The tumors from all experiments were then processed for flow cytometry analysis or FACS-sorting on the same day. The resected mouse tumors were mechanically dissociated with surgical scissors and digested with Collagenase IV (Roche) and DNase I (Roche) in complete RPMI1640 medium for 30 min in a 37^0C shaking incubator (150 rpm). After enzymatic dissociation, the samples were transferred to ice to stop the reaction. The tumor suspension was then filtered using a 70 µm cell strainer (Becton Dickinson) and washed with the MACS buffer (0.5% FBS and 2mM EDTA in PBS) and centrifuged at 1100 rpm at 4^0C. Red blood cells were lysed with RBC lysis buffer (Thermo Fisher) followed by washing with the FACS buffer. The samples were then re-suspended in the FACS buffer and kept on ice throughout the staining procedure.

Flow cytometry

Flow cytometric analyses and cell sorting were performed using BD FACSVerse™ or FACSAria™ II and SH800S Cell Sorter (Sony Biotechnology), respectively. Cells were pre-incubated with Fc block CD16/32 (clone 2.4G2) prior to cell-specific staining protocols as designated gating strategy. Antibodies staining was done in FACS buffer for 20 min at 4^0C. For Ki-67 staining, cells were further fixed and permeabilized using fixation/Permeabilization buffer (Invitrogen) prior to antibody staining. For TAM sorting, cells were first blocked using Fc block/ CD16/32 (clone 2.4G2) in FACS buffer for 20 min at 4^0C, followed by cell-specific staining with Anti-CD45.2, Anti-Ly6G, Anti-Ly6C, Anti-F4/80, and Anti-CD11b for 30 min at 4^0C prior to sorting.

Immunoblotting

All cells were briefly rinsed with ice-cold PBS before harvesting with indicated lysis buffers. For whole-cell lysates, the cells were re-suspended in NP-40 lysis buffer (50 mM Tris–HCl pH 7.4, 1% (vol/vol) Nonidet P–40, 150 mM sodium chloride, 1mM EDTA) containing protease and phosphatase inhibitors. For cytosolic and nuclear fractions, the cells were lysed in 500 µL Cytoplasmic lysis buffer (20mM HEPES, 0.25M sucrose, 1.5mM $MgCl_2$, 10mM KCl, 10% Glycerol, 0.5% (vol/vol) NP-40) containing protease and phosphatase inhibitors followed by 10 min incubation on ice and centrifugation at 1000g for 10 min at 4^0C. The supernatant (cytosolic fraction) was transferred to a fresh tube. The remaining nuclear pellet was then rinsed once with Cytoplasmic lysis buffer and spun down at 1000g for 10 min at 4^0C. The supernatant was discarded and the pellet was resuspended in 200 µL RIPA buffer (50 mM Tris pH 8.0, 1% (vol/vol) NP-40, 150 mM sodium chloride, 1mM EDTA, 1mM EGTA, 0.1% SDS, 0.5% Sodium deoxycholate) containing protease and phosphatase inhibitors. After centrifugation, protein

concentrations were measured by the Bradford method, analyzed by SDS–PAGE and transferred onto 0.2 μm pore size Immun-Blot® PVDF membranes (Bio-Rad Laboratories, Inc.). Membranes were then incubated with indicated primary antibodies and HRP-coupled secondary antibodies (NA9310 and NA9340; GE Healthcare). Membranes were treated with Luminata™ Forte Western HRP substrate (Millipore) and luminescence was detected with a luminescent image analyzer (Amersham Imager 600; GE Healthcare).

For co-immunoprecipitation experiments and Silver staining, cells were lysed using 1% (vol/vol) NP-40 lysis buffer and proteins were then immunoprecipitated overnight at 4^0C with respective antibody, Protein G Dynabeads (Invitrogen), followed by frequent wash before subjected to SDS-PAGE. Gel was then proceeded to Immunoblot or silver staining using EzStain Silver Kit (ATTO) according to the manufacturer's recommendations.

Immunofluorescence

Cells were seeded onto glass coverslips overnight (or otherwise described) and fixed with 4% formaldehyde (Nacalai Tesque, Japan) for 10 min at room temperature, followed by quenching with 0.1M glycine for 10 min and permeabilizing with PBS plus 0.2% Triton X-100 for 15 min. After washing, cells were then blocked in 1% BSA for 30 min at room temperature prior to first antibody incubation. Subsequently, cells were stained with secondary antibodies coupled to AlexaFluor 488 (Life Technologies), AlexaFluor 568 (Life Technologies) and Hoechst 33258 (Life Technologies), mounted on the glass slide using ProLong Gold anti-fade reagent (Molecular Probes), and visualized using Leica TCS SPE microscopy system. For mitochondria staining, cells were first incubated with medium containing 150nM MitoSpy™ Red CMXRos for 20 min prior to fixation without proceed to permeabilization, followed by staining with Hoechst

33258 before mounting onto glass slide. Mitochondrial interconnectivity was measured as described previously (*54*).

Lentiviral-construction and transduction

pFUGW-EF1α-Flag-Ccnj (and mutant) and pINDUCER20-Flag-Ccnj were constructed by cloning Flag-tag Ccnj coding sequence from pre-existing plasmid (pFLAG-CMV2-Ccnj-FL and mutant) into the pFUGW-EF1α vector and pINDUCER20 vector respectively using In-Fusion® HD Cloning Kit. pFUGW-EF1α is a modified version of lentiCas9-Blast (addgene #52962) that contains a Blasticidin resistance cassette and EF1α promoter while Cas9 sequence was removed. pINDUCER20 is modified from pInducer20 (addgene #44012) and pENTR1A no ccDB (w48-1) (addgene #17398) through recombination using Gateway Cloning system using LR Clonase™ II from Thermo Fisher Scientific (Waltham, MA, USA). The shRNA lentiviral vectors pLKO.3 Thy1.1 were used for gene knockdown experiment in macrophage by incorporating short hairpin constructs for targeting *Foxk1, Dnm1l* (Drp1), *Gorasp2* (Gors2), and *Nfat5* together with negative control (listed in Table S3). Lentiviral particles were produced in HEK293T cells by co-transfecting third generation lentiviral packaging vectors and lentiviral vectors containing the gene-of-interest. Supernatants were collected after 48 hour and filtered through a 0.45 μm filter. RAW264.7 cells were then transduced with the supernatant for 48 hour with 5 μg/mL polybrene, prior to spin-infection at 1000g for 2 hour at 33^0C. Transduced cells were selected with 5 μg/mL Blasticidin (Sigma) starting 48 hour after transduction. After 5-7 days, resistant polyclonal colonies were further expanded and expression was assessed by RT-qPCR and Immunoblotting. For shRNA knockdown, lentiviral transduced cells were sorted using fluorochrome-labelled Thy1.1 antibody and assessed by RT-qPCR and/or Immunoblotting. Control cells were

transduced as followed with pFUGW-EF1α-luc (in which it contains luciferase coding sequence instead of Flag-tagged cyclin J) and pINDUCER20-empty vector respectively.

Isolation of DNA and RNA for qPCR

Total RNA was isolated using TRIzol (Thermo Fisher), followed by genomic DNA removal and reverse transcription using ReverTra Ace reverse transcription kit with gDNA removal (Toyobo Co., Ltd.) according to the manufacturer's instructions. For quantitative PCR, cDNA fragments were amplified using StepOnePlus™ Real-Time PCR System (Applied Biosystems™) with SYBR® Green Realtime PCR Master Mix (Toyobo Co., Ltd.). 18S rRNA was used to normalize relative mRNA expression. For mtDNA measurement, DNA was extracted from cell pellets using QIAGEN DNA extraction kit according to manufacturer's instructions. Quantification of mitochondrial DNA copy number was performed by qPCR of two nuclear encoded genes (18s and Pecam-1), and 3 mitochondrial genes (*MT-COX1*, *MT-COX2* and *MT-ND3*). Mitochondrial DNA copy number was calculated by averaging the ΔCt values of each gene categories in the calculation: mtDNA copy number = $2*(2\text{^}(Ct^{\text{Nuclear genes}} - Ct^{\text{Mitochondrial genes}}))$. The qPCR primers used in this study is listed in Table S2.

ELISA assay

Concentrations of cytokines in supernatant collected from macrophage cultures were measured by ELISA according to the manufacturers' instructions. The ELISA kit includes: IL-6, IL-12p40, TNF, and IL-10 (Thermo Fisher).

Electron microscopy

Cells were fixed with 2.5% glutaraldehyde in 0.1M cacodylate buffer for 1 hour at 4 °C and postfixed with 1% osmium tetroxide in the same buffer for 1 hour at 4°C. After dehydration with a series of ethanol gradients followed by propylene oxide, the cells were embedded in Epon 812 Resin mixture, which were polymerized at 70°C for 2 days. Ultrathin sections were stained with uranyl acetate and lead citrate and examined with a Hitachi-HT7700 electron microscope at 80 kV.

ECAR and OCR analysis

The OCR and ECAR were measured using an XFp Extracellular Flux Analyzer (Agilent Technologies, Inc). For OCR, macrophages were seeded at 2.5×10^4 cells/well density in 96-well plates overnight to allow adherence to the plate. After 6 hours of LPS (1 μg/mL) administration, the cells were changed to unbuffered assay media (base medium supplemented with 10 mM glucose, 1 mM pyruvate, 2 mM glutamine, pH 7.4) and incubated in a non-CO_2 incubator for 1 hour. Four baseline measurements were taken before sequential injection of mitochondrial inhibitors oligomycin (OM), Carbonyl cyanide-4 (trifluoromethoxy) phyenylhydrazone (FCCP), and antimycin A plus rotenone (AR). For ECAR, after overnight incubation, the cells were changed to unbuffered assay media without 10mM glucose and incubated in non-CO_2 incubator for 1 hour. Four baseline measurements were taken before sequential injection of glucose (GLU), OM, and 2-Deoxy-D-glucose (2-DG). OCR and ECAR were automatically calculated using the Seahorse XFp Analyzer software.

Measurement of mitochondrial membrane potential and ROS

Cells were seeded in non-tissue culture plates and stimulated with LPS, prior to staining with Mitospy NIR DliC(5) (for mitochondrial membrane potential), Mitospy Red CMXRos (for visualisation), MitoSOX Red (for mitochondrial ROS) and DCFDA (for cellular ROS) according to manufacturer's instructions. For flow cytometry analysis, data were acquired with BD FACSVerse™ and analyzed with FlowJo software (Tree Star). Immunofluorescent analysis was performed as described above.

Phosphoproteomics: Mass spectrometry and data analysis

Protein digestion was performed according to the phase transfer surfactant (PTS) protocol (*55*). Briefly, cells were first treated with 5μM Nocodazole for 12 hours. Prior to harvest, cells were further treated with 100nM Flavopiridol for 4 hours, or 10nM Roscovitine for 30 minutes. Cells were then lysed in PTS buffer (12 mM SDC, 12 mM SLS, 1% protease inhibitor, and 1% phosphatase inhibitor 2 and 3 in 100 mM Tris-HCl, pH 9.0). Protein concentration was determined by BCA protein assay kit. Proteins were reduced with 10 mM DTT and alkylated with 50 mM IAA. After 5-fold dilution with 50 mM ammonium bicarbonate, Lys-C and trypsin were added at a 1:100 (w/w) protease-to-protein ratio, followed by incubation overnight at 37^0C. Then an equal volume of ethyl acetate was added, and the solution was acidified with TFA. After removing the organic phase, the samples were dried by SpeedVac concentrator and reconstituted in 5% ACN and 0.1% TFA. The peptides were desalted using SDB-XC StageTips (*56, 57*). Phosphopeptides enrichment was performed by hydroxy acid-modified metal-oxide chromatography (HAMMOC) as described previously(*58*). For both proteome and phosphoproteome samples, peptides were labeled with TMT reagents. The combined peptide

samples were fractionated into 5 fractions for the CDK inhibitors experiment and 6 fractions for the cyclin J expression experiment by StageTip-based high-pH reversed-phase LC.

The peptides were analyzed by Orbitrap Fusion Lumos mass spectrometry (Thermo Fisher Scientific) coupled with an Ultimate 3000 (Thermo Fisher Scientific) pump and an HTC-PAL autosampler (CTC Analytics). An in-house analytical column (100 μm × 150 mm) was packed with ReproSil-Pur C18-AQ (3 μm, Dr. Maisch, Ammerbuch, Germany). The injection volume was 5 μL and the flow rate was 500 nL/min. The mobile phases consisted of 0.5% acetic acid (A) and 0.5% acetic acid in 80% ACN (B). The gradient program was as follows: 5-15% B (5 min), 15-40% B (145 min), 40-99% B (5 min), 99% B (10 min), 99-5% B (0.1 min), and 5% B (29.9 min) for the CDK inhibitors experiment, and 5-15% B (5 min), 15-40% B (115 min), 40-99% B (5 min), 99% B (10 min), 99-5% B (0.1 min), and 5% B (29.9 min) for the cyclin J-expressing experiment. Both MS1 and MS2 scans were acquired by Orbitrap. The MS1 survey scan was performed at a resolution of 120,000 in the scan range of m/z 375-1,500 with an AGC target value of $4e^5$. The MS2 scan was performed at a resolution of 50,000 and 15,000 for the CDK inhibitors experiment and the Cyclin J expression experiment, respectively. The AGC target value was 1e5 and the scan cycle was 3 sec. Dynamic exclusion was set to 30 sec and normalized collision energy for HCD was 38%.

Peak lists were generated from the raw MS/MS spectra using MaxQuant (v1.6.2.10) (*59*). Then the resulting .mgf files were searched against SwissProt *Mus musculus* database (17,042 entries, downloaded on July, 2020) using Mascot v2.7 (Matrix Science) with a precursor mass tolerance of 5 ppm and a fragment ion mass tolerance of 20 ppm. Carbamidomethylation on cysteine and TMT6plex on lysine and N-terminus were set as fixed modifications. Oxidation on methionine was set as a variable modification. For phosphoproteomics experiments, phosphorylation on

serine, threonine, and tyrosine as well as methionine oxidation were set as variable modifications. Up to two missed cleavages were allowed for trypsin and Lys-C digestion. The results were filtered at 1% peptide-level false discovery rate (FDR). The obtained TMT reporter ion intensities were used for protein and phosphopeptide quantification. Missing values were imputed by the minimum intensity across the corresponding channel. For each channel, reporter ion intensities were normalized so that the median peptide quantification ratio to the lowest channel was 1. Each protein was quantified by summing all peptide intensities attributed to the protein. For phosphoproteomics, we applied an additional cutoff that required at least three successive y- or b-ions with a further two or more y-, b- and/or precursor-origin neutral loss ions, based on the error-tolerant peptide sequence tag concept (*60*). Phosphosite localization was confirmed using a site-determining ion combination method as described previously (*61*) .

RNA-seq and data analysis

For RNA-seq of lentiviral-transduced stable RAW264.7 cells, the cells were first harvested and lysed using Trizol, followed by generation of the RNA library via the NEBNext® Ultra™ II Directional RNA Library Prep Kit (Illumina) and sequenced on the NextSeq system using NextSeq 500 High-Output v2 Kit (Illumina) according to the manufacturer's instructions. The sequenced data was uploaded to the Galaxy web platform (usegalaxy.org) for pre-processing (*62*). Briefly, the reads were trimmed, mapped against the human genome (hg38) and counted. Filtering of the reads was performed using the R package, 'edgeR'(*63*). The counts for each sample were used as input. Genes that had counts less than 1 CPM (counts per million reads mapped) were filtered out. The libraries were then normalized for RNA composition bias via the trimmed mean of M-values (TMM) method. The mean-variance relationship in the data was

calculated and a linear model was applied to the data using the 'limma-Voom' R package(*64*). Finally, the Voom-transformed data was used to test for differentially expressed genes.

Gene-ontology (GO) analysis were performed on differential gene lists using GO enrichment analysis platform from PANTHER specifically on biological processes. Ranked GSEA from Broad Institute was performed with software version 4.0.3. GSEA pre-ranked analysis (GseaPreranked) was performed using default settings except for "Collapse dataset to gene symbols" set to "False". Prior to analysis, a ranked list was calculated with each gene assigned a score based on the $-Log_{10}$(Adjusted P-value) and the direction of the log fold-change ("+" or "–").

Homology modeling of mouse cyclin J/CDK2 complex

To build a homology model of mouse cyclin J protein, structural templates were first screened against the Protein Data Bank (PDB)(*65*) by HHpred (*66*). One of the best templates (PDB ID: 3ddp, chain B(*67*)) was human cyclin A2, with a sequence identity of 28%, bound to human CDK2 (chain A). Mouse CDK2 has a long insertion, and PSIPRED(*68*) was used to predict the secondary structure of this insertion, which was then used as a structural constraint and a 3D model of the HHpred alignment was rendered by MODELLER (*69*). Mouse and human CDK2 proteins are highly conserved at their cyclin binding sites, however there are no mouse cyclin-CDK2 complex structures reported. From the complex model, the conservation of interface residues was analyzed using representative complexes of human CDK2 and various cyclins. 3D structure of the complex model was visualized by Pymol [The PyMOL Molecular Graphics System, Version 2.4.0 Schrödinger, LLC.].

Statistical analysis

Data are presented as means ± SEM of at least two independent experiments. All analyses were performed using GraphPad Prism 9 (GraphPad). Statistical analyses were performed includes unpaired *t*-test, one-way ANOVA with Dunnett's test; or two-way ANOVA, with Holm–Sidak correction method for pairwise multiple comparisons. Survival rate was analyzed using Kaplan-Meier log-rank test. No statistical methods were used to pre-determine sample size. $P < 0.05$ considered statistically significant. $*P < 0.05$, $**P < 0.01$, $***P < 0.001$ and $****P < 0.0001$; NS, not significant or stated otherwise.

Supplementary Materials

Figs. S1 to S11.

Tables S1 to S3.

Data files S1 to S5.

References and Notes

1. P. J. Murray, J. E. Allen, S. K. Biswas, E. A. Fisher, D. W. Gilroy, S. Goerdt, S. Gordon, J. A. Hamilton, L. B. Ivashkiv, T. Lawrence, M. Locati, A. Mantovani, F. O. Martinez, J. L. Mege, D. M. Mosser, G. Natoli, J. P. Saeij, J. L. Schultze, K. A. Shirey, A. Sica, J. Suttles, I. Udalova, J. A. van Ginderachter, S. N. Vogel, T. A. Wynn, Macrophage activation and polarization: nomenclature and experimental guidelines. *Immunity* **41**, 14-20 (2014).
2. T. A. Wynn, A. Chawla, J. W. Pollard, Macrophage biology in development, homeostasis and disease. *Nature* **496**, 445-455 (2013).
3. B. Z. Qian, J. W. Pollard, Macrophage diversity enhances tumor progression and metastasis. *Cell* **141**, 39-51 (2010).
4. K. A. Fitzgerald, J. C. Kagan, Toll-like Receptors and the Control of Immunity. *Cell* **180**, 1044-1066 (2020).
5. L. A. O'Neill, E. J. Pearce, Immunometabolism governs dendritic cell and macrophage function. *J Exp Med* **213**, 15-23 (2016).
6. M. A. Lauterbach, J. E. Hanke, M. Serefidou, M. S. J. Mangan, C. C. Kolbe, T. Hess, M. Rothe, R. Kaiser, F. Hoss, J. Gehlen, G. Engels, M. Kreutzenbeck, S. V. Schmidt, A. Christ, A. Imhof, K. Hiller, E. Latz, Toll-like Receptor Signaling Rewires Macrophage Metabolism and Promotes Histone Acetylation via ATP-Citrate Lyase. *Immunity* **51**, 997-1011 e1017 (2019).
7. A. Palazon, A. W. Goldrath, V. Nizet, R. S. Johnson, HIF transcription factors, inflammation, and immunity. *Immunity* **41**, 518-528 (2014).
8. S. E. Corcoran, L. A. O'Neill, HIF1alpha and metabolic reprogramming in inflammation. *J Clin Invest* **126**, 3699-3707 (2016).
9. G. M. Tannahill, A. M. Curtis, J. Adamik, E. M. Palsson-McDermott, A. F. McGettrick, G. Goel, C. Frezza, N. J. Bernard, B. Kelly, N. H. Foley, L. Zheng, A. Gardet, Z. Tong, S. S. Jany, S. C. Corr, M. Haneklaus, B. E. Caffrey, K. Pierce, S. Walmsley, F. C. Beasley, E. Cummins, V. Nizet, M. Whyte, C. T. Taylor, H. Lin, S. L. Masters, E. Gottlieb, V. P. Kelly, C. Clish, P. E. Auron, R. J. Xavier, L. A. J. O'Neill, Succinate is an inflammatory signal that induces IL-1 beta through HIF-1 alpha. *Nature* **496**, 238-+ (2013).
10. R. Kapetanovic, S. F. Afroz, D. Ramnath, G. M. Lawrence, T. Okada, J. E. Curson, J. de Bruin, D. P. Fairlie, K. Schroder, J. C. St John, A. Blumenthal, M. J. Sweet, Lipopolysaccharide promotes Drp1-dependent mitochondrial fission and associated inflammatory responses in macrophages. *Immunol Cell Biol* **98**, 528-539 (2020).
11. A. P. West, I. E. Brodsky, C. Rahner, D. K. Woo, H. Erdjument-Bromage, P. Tempst, M. C. Walsh, Y. Choi, G. S. Shadel, S. Ghosh, TLR signalling augments macrophage bactericidal activity through mitochondrial ROS. *Nature* **472**, 476-480 (2011).
12. S. J. Forrester, D. S. Kikuchi, M. S. Hernandes, Q. Xu, K. K. Griendling, Reactive Oxygen Species in Metabolic and Inflammatory Signaling. *Circ Res* **122**, 877-902 (2018).
13. O. Takeuchi, S. Akira, Pattern recognition receptors and inflammation. *Cell* **140**, 805-820 (2010).
14. E. Quandt, M. P. C. Ribeiro, J. Clotet, Atypical cyclins: the extended family portrait. *Cell Mol Life Sci* **77**, 231-242 (2020).

15. D. O. Morgan, Cyclin-dependent kinases: engines, clocks, and microprocessors. *Annu Rev Cell Dev Biol* **13**, 261-291 (1997).
16. S. Lim, P. Kaldis, Cdks, cyclins and CKIs: roles beyond cell cycle regulation. *Development* **140**, 3079-3093 (2013).
17. M. L. Schmitz, M. Kracht, Cyclin-Dependent Kinases as Coregulators of Inflammatory Gene Expression. *Trends Pharmacol Sci* **37**, 101-113 (2016).
18. S. Choudhary, K. P. Rosenblatt, L. Fang, B. Tian, Z. H. Wu, A. R. Brasier, High throughput short interfering RNA (siRNA) screening of the human kinome identifies novel kinases controlling the canonical nuclear factor-kappaB (NF-kappaB) activation pathway. *J Biol Chem* **286**, 37187-37195 (2011).
19. R. S. Jhou, K. H. Sun, G. H. Sun, H. H. Wang, C. I. Chang, H. C. Huang, S. Y. Lu, S. J. Tang, Inhibition of cyclin-dependent kinases by olomoucine and roscovitine reduces lipopolysaccharide-induced inflammatory responses via down-regulation of nuclear factor kappaB. *Cell Prolif* **42**, 141-149 (2009).
20. O. Cingoz, S. P. Goff, Cyclin-dependent kinase activity is required for type I interferon production. *Proc Natl Acad Sci U S A* **115**, E2950-E2959 (2018).
21. H. J. Lee, G. H. Chua, A. Krishnan, D. P. Lane, C. S. Verma, Substrate specificity of cyclins determined by electrostatics. *Cell Cycle* **6**, 2219-2226 (2007).
22. M. P. Swaffer, A. W. Jones, H. R. Flynn, A. P. Snijders, P. Nurse, CDK Substrate Phosphorylation and Ordering the Cell Cycle. *Cell* **167**, 1750-1761 e1716 (2016).
23. A. Dey, W. Yang, A. Gegonne, A. Nishiyama, R. Pan, R. Yagi, A. Grinberg, F. D. Finkelman, K. Pfeifer, J. Zhu, D. Singer, J. Zhu, K. Ozato, BRD4 directs hematopoietic stem cell development and modulates macrophage inflammatory responses. *EMBO J* **38**, (2019).
24. L. Liu, Y. Lu, J. Martinez, Y. Bi, G. Lian, T. Wang, S. Milasta, J. Wang, M. Yang, G. Liu, D. R. Green, R. Wang, Proinflammatory signal suppresses proliferation and shifts macrophage metabolism from Myc-dependent to HIF1alpha-dependent. *Proc Natl Acad Sci U S A* **113**, 1564-1569 (2016).
25. P. K. Vadiveloo, H. Christopoulos, U. Novak, I. Kola, P. J. Hertzog, J. A. Hamilton, Type I interferons mediate the lipopolysaccharide induction of macrophage cyclin D2. *J Interferon Cytokine Res* **20**, 355-359 (2000).
26. P. K. Vadiveloo, G. Vairo, A. K. Royston, U. Novak, J. A. Hamilton, Proliferation-independent induction of macrophage cyclin D2, and repression of cyclin D1, by lipopolysaccharide. *J Biol Chem* **273**, 23104-23109 (1998).
27. R. L. Finley, Jr., B. J. Thomas, S. L. Zipursky, R. Brent, Isolation of Drosophila cyclin D, a protein expressed in the morphogenetic furrow before entry into S phase. *Proc Natl Acad Sci U S A* **93**, 3011-3015 (1996).
28. M. Malumbres, Cyclin-dependent kinases. *Genome Biol* **15**, 122 (2014).
29. T. J. Gibson, J. D. Thompson, A. Blocker, T. Kouzarides, Evidence for a protein domain superfamily shared by the cyclins, TFIIB and RB/p107. *Nucleic Acids Res* **22**, 946-952 (1994).
30. S. R. Himes, S. Cronau, C. Mulford, D. A. Hume, The Runx1 transcription factor controls CSF-1-dependent and -independent growth and survival of macrophages. *Oncogene* **24**, 5278-5286 (2005).
31. V. Sukonina, H. Ma, W. Zhang, S. Bartesaghi, S. Subhash, M. Heglind, H. Foyn, M. J. Betz, D. Nilsson, M. E. Lidell, J. Naumann, S. Haufs-Brusberg, H. Palmgren, T. Mondal,

M. Beg, M. P. Jedrychowski, K. Tasken, A. Pfeifer, X. R. Peng, C. Kanduri, S. Enerback, FOXK1 and FOXK2 regulate aerobic glycolysis. *Nature* **566**, 279-283 (2019).
32. C. J. Bowman, D. E. Ayer, B. D. Dynlacht, Foxk proteins repress the initiation of starvation-induced atrophy and autophagy programs. *Nat Cell Biol* **16**, 1202-1214 (2014).
33. H. Nakatsumi, M. Matsumoto, K. I. Nakayama, Noncanonical Pathway for Regulation of CCL2 Expression by an mTORC1-FOXK1 Axis Promotes Recruitment of Tumor-Associated Macrophages. *Cell Rep* **21**, 2471-2486 (2017).
34. T. B. Fonseca, A. Sanchez-Guerrero, I. Milosevic, N. Raimundo, Mitochondrial fission requires DRP1 but not dynamins. *Nature* **570**, E34-E42 (2019).
35. N. Taguchi, N. Ishihara, A. Jofuku, T. Oka, K. Mihara, Mitotic phosphorylation of dynamin-related GTPase Drp1 participates in mitochondrial fission. *J Biol Chem* **282**, 11521-11529 (2007).
36. D. G. DeNardo, B. Ruffell, Macrophages as regulators of tumour immunity and immunotherapy. *Nat Rev Immunol* **19**, 369-382 (2019).
37. I. Vitale, G. Manic, L. M. Coussens, G. Kroemer, L. Galluzzi, Macrophages and Metabolism in the Tumor Microenvironment. *Cell Metab* **30**, 36-50 (2019).
38. O. R. Colegio, N. Q. Chu, A. L. Szabo, T. Chu, A. M. Rhebergen, V. Jairam, N. Cyrus, C. E. Brokowski, S. C. Eisenbarth, G. M. Phillips, G. W. Cline, A. J. Phillips, R. Medzhitov, Functional polarization of tumour-associated macrophages by tumour-derived lactic acid. *Nature* **513**, 559-563 (2014).
39. K. Z. Lee, M. Lestradet, C. Socha, S. Schirmeier, A. Schmitz, C. Spenle, O. Lefebvre, C. Keime, W. M. Yamba, R. Bou Aoun, S. Liegeois, Y. Schwab, P. Simon-Assmann, F. Dalle, D. Ferrandon, Enterocyte Purge and Rapid Recovery Is a Resilience Reaction of the Gut Epithelium to Pore-Forming Toxin Attack. *Cell Host Microbe* **20**, 716-730 (2016).
40. H. Wang, B. N. Nicolay, J. M. Chick, X. Gao, Y. Geng, H. Ren, H. Gao, G. Yang, J. A. Williams, J. M. Suski, M. A. Keibler, E. Sicinska, U. Gerdemann, W. N. Haining, T. M. Roberts, K. Polyak, S. P. Gygi, N. J. Dyson, P. Sicinski, The metabolic function of cyclin D3-CDK6 kinase in cancer cell survival. *Nature* **546**, 426-430 (2017).
41. Y. Lee, J. E. Dominy, Y. J. Choi, M. Jurczak, N. Tolliday, J. P. Camporez, H. Chim, J. H. Lim, H. B. Ruan, X. Yang, F. Vazquez, P. Sicinski, G. I. Shulman, P. Puigserver, Cyclin D1-Cdk4 controls glucose metabolism independently of cell cycle progression. *Nature* **510**, 547-551 (2014).
42. I. C. Lopez-Mejia, S. Lagarrigue, A. Giralt, L. Martinez-Carreres, N. Zanou, P. D. Denechaud, J. Castillo-Armengol, C. Chavey, M. Orpinell, B. Delacuisine, A. Nasrallah, C. Collodet, L. Zhang, B. Viollet, D. G. Hardie, L. Fajas, CDK4 Phosphorylates AMPKalpha2 to Inhibit Its Activity and Repress Fatty Acid Oxidation. *Mol Cell* **68**, 336-349 e336 (2017).
43. L. He, A. P. Gomes, X. Wang, S. O. Yoon, G. Lee, M. J. Nagiec, S. Cho, A. Chavez, T. Islam, Y. Yu, J. M. Asara, B. Y. Kim, J. Blenis, mTORC1 Promotes Metabolic Reprogramming by the Suppression of GSK3-Dependent Foxk1 Phosphorylation. *Mol Cell* **70**, 949-960 e944 (2018).
44. M. Sakaguchi, W. Cai, C. H. Wang, C. T. Cederquist, M. Damasio, E. P. Homan, T. Batista, A. K. Ramirez, M. K. Gupta, M. Steger, N. J. Wewer Albrechtsen, S. K. Singh, E. Araki, M. Mann, S. Enerback, C. R. Kahn, FoxK1 and FoxK2 in insulin regulation of cellular and mitochondrial metabolism. *Nat Commun* **10**, 1582 (2019).

45. D. G. Russell, L. Huang, B. C. VanderVen, Immunometabolism at the interface between macrophages and pathogens. *Nat Rev Immunol* **19**, 291-304 (2019).
46. M. Liesa, O. S. Shirihai, Mitochondrial dynamics in the regulation of nutrient utilization and energy expenditure. *Cell Metab* **17**, 491-506 (2013).
47. L. Simula, I. Pacella, A. Colamatteo, C. Procaccini, V. Cancila, M. Bordi, C. Tregnago, M. Corrado, M. Pigazzi, V. Barnaba, C. Tripodo, G. Matarese, S. Piconese, S. Campello, Drp1 Controls Effective T Cell Immune-Surveillance by Regulating T Cell Migration, Proliferation, and cMyc-Dependent Metabolic Reprogramming. *Cell Rep* **25**, 3059-3073 e3010 (2018).
48. S. Park, J. H. Won, I. Hwang, S. Hong, H. K. Lee, J. W. Yu, Defective mitochondrial fission augments NLRP3 inflammasome activation. *Sci Rep* **5**, 15489 (2015).
49. Z. Gao, Y. Li, F. Wang, T. Huang, K. Fan, Y. Zhang, J. Zhong, Q. Cao, T. Chao, J. Jia, S. Yang, L. Zhang, Y. Xiao, J. Y. Zhou, X. H. Feng, J. Jin, Mitochondrial dynamics controls anti-tumour innate immunity by regulating CHIP-IRF1 axis stability. *Nat Commun* **8**, 1805 (2017).
50. J. Tur, S. Pereira-Lopes, T. Vico, E. A. Marin, J. P. Munoz, M. Hernandez-Alvarez, P. J. Cardona, A. Zorzano, J. Lloberas, A. Celada, Mitofusin 2 in Macrophages Links Mitochondrial ROS Production, Cytokine Release, Phagocytosis, Autophagy, and Bactericidal Activity. *Cell Rep* **32**, 108079 (2020).
51. A. L. Doedens, C. Stockmann, M. P. Rubinstein, D. Liao, N. Zhang, D. G. DeNardo, L. M. Coussens, M. Karin, A. W. Goldrath, R. S. Johnson, Macrophage expression of hypoxia-inducible factor-1 alpha suppresses T-cell function and promotes tumor progression. *Cancer Res* **70**, 7465-7475 (2010).
52. B. E. Clausen, C. Burkhardt, W. Reith, R. Renkawitz, I. Forster, Conditional gene targeting in macrophages and granulocytes using LysMcre mice. *Transgenic Res* **8**, 265-277 (1999).
53. F. R. Greten, L. Eckmann, T. F. Greten, J. M. Park, Z. W. Li, L. J. Egan, M. F. Kagnoff, M. Karin, IKKbeta links inflammation and tumorigenesis in a mouse model of colitis-associated cancer. *Cell* **118**, 285-296 (2004).
54. R. K. Dagda, S. J. Cherra, 3rd, S. M. Kulich, A. Tandon, D. Park, C. T. Chu, Loss of PINK1 function promotes mitophagy through effects on oxidative stress and mitochondrial fission. *J Biol Chem* **284**, 13843-13855 (2009).
55. T. Masuda, M. Tomita, Y. Ishihama, Phase transfer surfactant-aided trypsin digestion for membrane proteome analysis. *J Proteome Res* **7**, 731-740 (2008).
56. J. Rappsilber, Y. Ishihama, M. Mann, Stop and go extraction tips for matrix-assisted laser desorption/ionization, nanoelectrospray, and LC/MS sample pretreatment in proteomics. *Anal Chem* **75**, 663-670 (2003).
57. J. Rappsilber, M. Mann, Y. Ishihama, Protocol for micro-purification, enrichment, pre-fractionation and storage of peptides for proteomics using StageTips. *Nat Protoc* **2**, 1896-1906 (2007).
58. N. Sugiyama, T. Masuda, K. Shinoda, A. Nakamura, M. Tomita, Y. Ishihama, Phosphopeptide enrichment by aliphatic hydroxy acid-modified metal oxide chromatography for nano-LC-MS/MS in proteomics applications. *Mol Cell Proteomics* **6**, 1103-1109 (2007).

59. J. Cox, M. Mann, MaxQuant enables high peptide identification rates, individualized p.p.b.-range mass accuracies and proteome-wide protein quantification. *Nat Biotechnol* **26**, 1367-1372 (2008).
60. M. Mann, M. Wilm, Error-tolerant identification of peptides in sequence databases by peptide sequence tags. *Anal Chem* **66**, 4390-4399 (1994).
61. H. Nakagami, N. Sugiyama, K. Mochida, A. Daudi, Y. Yoshida, T. Toyoda, M. Tomita, Y. Ishihama, K. Shirasu, Large-scale comparative phosphoproteomics identifies conserved phosphorylation sites in plants. *Plant Physiol* **153**, 1161-1174 (2010).
62. E. Afgan, D. Baker, B. Batut, M. van den Beek, D. Bouvier, M. Cech, J. Chilton, D. Clements, N. Coraor, B. A. Gruning, A. Guerler, J. Hillman-Jackson, S. Hiltemann, V. Jalili, H. Rasche, N. Soranzo, J. Goecks, J. Taylor, A. Nekrutenko, D. Blankenberg, The Galaxy platform for accessible, reproducible and collaborative biomedical analyses: 2018 update. *Nucleic Acids Res* **46**, W537-W544 (2018).
63. M. D. Robinson, D. J. McCarthy, G. K. Smyth, edgeR: a Bioconductor package for differential expression analysis of digital gene expression data. *Bioinformatics* **26**, 139-140 (2010).
64. C. W. Law, Y. Chen, W. Shi, G. K. Smyth, voom: Precision weights unlock linear model analysis tools for RNA-seq read counts. *Genome Biol* **15**, R29 (2014).
65. H. M. Berman, J. Westbrook, Z. Feng, G. Gilliland, T. N. Bhat, H. Weissig, I. N. Shindyalov, P. E. Bourne, The Protein Data Bank. *Nucleic Acids Res* **28**, 235-242 (2000).
66. L. Zimmermann, A. Stephens, S. Z. Nam, D. Rau, J. Kubler, M. Lozajic, F. Gabler, J. Soding, A. N. Lupas, V. Alva, A Completely Reimplemented MPI Bioinformatics Toolkit with a New HHpred Server at its Core. *J Mol Biol* **430**, 2237-2243 (2018).
67. K. Bettayeb, N. Oumata, A. Echalier, Y. Ferandin, J. A. Endicott, H. Galons, L. Meijer, CR8, a potent and selective, roscovitine-derived inhibitor of cyclin-dependent kinases. *Oncogene* **27**, 5797-5807 (2008).
68. D. W. A. Buchan, D. T. Jones, The PSIPRED Protein Analysis Workbench: 20 years on. *Nucleic Acids Res* **47**, W402-W407 (2019).
69. B. Webb, A. Sali, Comparative Protein Structure Modeling Using MODELLER. *Curr Protoc Bioinformatics* **54**, 5 6 1-5 6 37 (2016).

Acknowledgments: We thank all the colleagues in our laboratory for helpful discussion and suggestions. We thank Yoshimi Okumoto for secretarial assistance, and Takefumi Kondo and Yukari Sando for technical assistance. We thank the Medical Research Support Center, Graduate School of Medicine, Kyoto University for the use of Seahorse XF96 Extracellular Flux Analyzer.

Funding:
Grant-in-Aid for Scientific Research (S) 18H05278N (OT)
Grant-in-Aid for Scientific Research on Innovative Areas "Genome Science" (221S0002 and 16H06279) of the Japan Society for the Promotion of Science (JSPS) (OT)
Grant-in-Aid by JSPS Core-to-Core Program, A. Advanced Research Networks (OT)
National Cancer Center Research and Development Fund (28-A-7) (OT)
Takeda Science Foundation (OT)

Author contributions: Experiments design and result analysis: YKC, ST, OT. Animal and cell cultures experiments: YKC, ST, LKH. Proteome profiling assays and phosphoproteomic analysis: YY, KI, YI. Performing electron microscopy and analysis: AH, TN. Bioinformatics analysis: YS, AV, FH. Structural modeling: SL, DMS *Drosophila* Cyclin J information: DF. Discussion and suggestions: MY, TU, TM. Writing – review & editing: YKC, ST, OT.

Competing interests: The authors declare that they have no competing interests.

Data and materials availability: All RNA-seq data have been deposited in DNA Data Bank of Japan (DDBJ) data repository (www.ddbj.nig.ac.jp) under accession number DRA010730 (Cyclin J expressing RAW264.7 cells) and DRA010729 (TAMs lacking Cyclin J). Previously published data re-analyzed for this study are found under the reference accessions GSE16755, GSE104641, GSE81291, and GSE35825. The proteomics data have been deposited to the ProteomeXchange Consortium the jPOST partner repository (https://repository.jpostdb.org/) with the dataset identifier PXD021176. All other data needed to evaluate the conclusions in the paper are present in the paper or the Supplementary Materials. *Ccnj*$^{fl/fl}$ mice require a material transfer agreement from Kyoto University, Kyoto, Japan.

Figure Legends

Fig. 1. *Ccnj* is a TLR- and IFN-inducible gene. (**A**) Heatmap showing expression of genes encoding cyclin family members in mouse BMDMs upon LPS or IL-4 stimulation for 4 hours. Data represent $\log_2$ fold change of treated over unstimulated BMDMs and are derived from a public database (GSE104641). **(B)** Expression of *Ccnj* and *Ccna2* in BMDMs, peritoneal macrophages, (PM) and RAW 264.7 macrophages upon LPS or IL-4 stimulation at indicated time points by RT-qPCR ($n = 3$). **(C)** Expression of *Il6*, *Il1b*, *Cxcl1*, *Il23a*, *Ifnb*, and *Il10* in cyclin J–expressing or control RAW264.7 macrophages upon stimulation with LPS or media alone (Med) for 6 hours by qPCR ($n = 3$). **(D)** Quantification of IL-6 and IL-10 by ELISA in media from cyclin J–expressing RAW264.7 cells stimulated with LPS for the indicated amounts of time ($n = 3$). **(E)** RT-qPCR analysis of *Ccnj* expression in sorted peritoneal immune cells from *Ccnj*$^{fl/fl}$ and *Ccnj*$^{fl/fl}$LyzM-Cre^{+} mice ($n \geq 3$). **(F)** Expression of *Il6*, *Cxcl1*, *Ifnb*, and *Il10* expression upon in vitro stimulation of PMs from *Ccnj*$^{fl/fl}$ and *Ccnj*$^{fl/fl}$LyzM-Cre^{+} mice with LPS for the indicated amounts of time points ($n \geq 3$). **(G)** Quantification of IL-6 and IL-12p40 secretion by ELISA in supernatant collected from PM cells of *Ccnj*$^{fl/fl}$ and *Ccnj*$^{fl/fl}$LyzM-Cre^{+} mice upon Pam_3CSK_4 or LPS stimulation for 24 hours ($n \geq 3$). All values are means ± SEM, where *n* indicates biological replicates for (B) to (D) and numbers of mice per genotype for (E) to (G). Statistical significance was determined by unpaired *t*-test (E) and two-way ANOVA with correction for multiple testing by Holm–Sidak method (B-D, F and G).

Fig. 2. Cyclin J suppresses activation-induced metabolic changes in macrophages. (**A and B**) GSEA analysis in hallmark and KEGG pathways derived from MSigDB collections in transcriptomic data of RAW264.7 macrophages transduced with control lentivirus encoding luciferase (Lenti-Ctrl) or cyclin J (Lenti-*Ccnj*) ($n = 3$). Normalized enrichment scores (NES) and

false discovery rate (FDR) are shown. Representative GSEA enrichment plots (B) of transcripts related to glycolysis and hypoxia. **(C)** Expression of genes related to glycolysis and cell cycle in Lenti-Ctrl and Lenti-*Ccnj* RAW264.7 macrophages by RT-qPCR (n = 3). **(D)** ECAR of Lenti-Ctrl and Lenti-*Ccnj* RAW264.7 macrophages with histogram showing basal and maximal ECAR (n = 6). **(E and F)** Immunoblot (IB) analysis and quantification of HIF-1α in RAW264.7 macrophages stably expressing cyclin J (E) and in PMs from *Ccnj*$^{fl/fl}$ and *Ccnj*$^{fl/fl}$LyzM-Cre^{+} mice (F) stimulated with LPS for indicated time points. β-actin is a loading control. Blot is representative of n = 3 independent experiments. (**G**) Mitochondrial stress tests of Lenti-Ctrl and Lenti-*Ccnj* RAW264.7 macrophages under resting conditions. Histogram shows basal respiration and maximal respiration (n = 6). (**H**) Spare respiratory capacity of macrophages in (G). (**I**) Flow cytometric histogram of mitochondrial membrane potential (Δψm) in Lenti-Ctrl and Lenti-*Ccnj* RAW264.7 macrophages (n = 6). (**J and K**) Representative flow cytometry plots and histograms of mtROS (J) and cellular ROS (K) in Lenti-Ctrl and Lenti-*Ccnj* RAW264.7 macrophages upon stimulation with LPS or media alone (Med) . Mean fluorescence intensity (MFI) values are noted on the flow cytometry plots. Histograms show the percentage of ROS^{+} cells (n = 3). Histograms represent mean ± SEM, where n indicates biological replicates. Statistical significance was determined by unpaired t-test (H and I) and two-way ANOVA with correction for multiple testing by Holm–Sidak method (C, D, G, J and K) .

Fig. 3. Cyclin J suppresses inflammatory gene expression in macrophages through CDKs. **(A)** Schematic representation of protein domains in cyclin A2, cyclin B1 and cyclin J. **(B)** Representative image of silver-stained gel of Flag immunoprecipitates (IP) from whole-cell extracts of Flag-Cyclin J–expressing HEK293T and HeLa cells. Arrows indicate proteins identified in the mass spectrometric analysis (Table S2). Image is representative of 2 independent

experiments. **(C)** Immunoblot (IB) analysis for HA and Flag in Flag immunoprecipitates from lysates of HEK293T cells coexpressing Flag-tagged CCNJ (cyclin J) or CCNA2 and HA-tagged CDK2. Blot is representative of 3 independent experiments. **(D)** Immunoblot analysis of Flag immunoprecipitates from lysates of HEK293T cells coexpressing Flag-tagged CCNJ and HA-tagged CDK3 or CDK5.Blot is representative of 3 independent experiments. **(E)** Schematic representation of cyclin J CBDs and full-length and deletion mutant constructs. **(F)** Immunoblot analysis of Flag immunoprecipitates from lysates of HEK293T cells coexpressing Flag-tagged full length and mutant CCNJ and HA-tagged CDK2. Blot is representative of 3 independent experiments. **(G)** Expression of *Il6*, *Ifnb*, *Il1b*, and *Il10* in RAW264.7 macrophages expressing full-length and CBD-lacking (ΔΔ) cyclin J and stimulated with LPS or media alone (Med) for 6 hours (n = 3). **(H)** Homology modeling of the mouse cyclin J and CDK2 complex using MODELLER. The CDK2 chain is shown in green, and the N-terminal and C-terminal CBDs of Cyclin J are in blue and yellow, respectively. Conserved residues of cyclin J on the binding interface are represented as red spheres. **(I)** Schematic representation of full-length cyclin J construct with a point mutation in the KFEE motif (K95R). **(J)** Immunoblot analysis of Flag immunprecipitates from lysates of HEK293T cells coexpressing of Flag-tagged WT or K95R cyclin J, together with HA-tagged CDK2. Blot is representative of 3 independent experiments. For (G), values are means ± SEM, where n indicates biological replicates. Statistical significance was determined by two-way ANOVA with correction for multiple testing by Holm–Sidak method.

Fig. 4. Cyclin J induces phosphorylation of CDK substrates in macrophages. (**A**) Immunoblot analysis of lysates from LPS-stimulated BMDMs using an antibody that recognizes

phosphorylated serine in the CDK substrate consensus motif, (K/H)pSP. β-actin is a loading control. Blot is representative of 2 independent experiments. **(B)** Immunoblot analysis of RAW264.7 macrophages constitutively expressing cyclin J (Lenti-*ccnj*) for proteins serine-phosphorylated on the CDK substrate motif (K/H)pSP or on motifs that are phosphorylated by both MAPK and CDK, PXpSP or pSX(R/K). Blot is representative of 2 independent experiments. **(C)** *Ccnj* expression in RAW264.7 macrophages expressing DOX-inducible cyclin J 24 hours post DOX treatment ($n = 3$). **(D)** Immunoblotting (IB) for Flag in RAW264.7 macrophages expressing DOX-inducible cyclin J 24 hours post-DOX treatment. Blot is representative of 2 independent experiments. **(E)** Immunoblot analysis of RAW264.7 macrophages expressing DOX-inducible cyclin J 8 hours post DOX treatment using antibodies recognizing serine phosphorylation in CDK substrate motifs and motifs targets by both MAPK and CDK. Blot is representative of 3 independent experiments. **(F)** Schematic view of acquisition of proteomic and phosphoproteomic data from RAW264.7 cells expressing DOX-inducible cyclin J 8 hours post DOX treatment. Cell extracts were collected and checked by immunoblotting (E) before phosphopeptide enrichment by hydroxy acid-modified metal-oxide chromatography (HAMMOC) prior to liquid chromatography with tandem mass spectrometry (LC/MS/MS). **(G and H)** Volcano plots showing peptide changes (G) and phosphopeptide changes (H) in DOX-induced RAW264.7 macrophages versus uninduced controls. **(I)** Logo analysis of 61 targeted phosphorylation sites identified in (H). **(J)** Expression of *Il6* and *Ifnb* in RAW264.7 macrophages treated with the indicated shRNAs and stimulated with LPS for 6 hours ($n = 3$). Values for histograms are means ± SEM, where *n* indicates biological replicates. Statistical significance was determined by one-way ANOVA with Dunnett's multiple test (J) and two-way ANOVA with correction for multiple testing by Holm–Sidak method (C).

Fig. 5. FoxK1 and Drp1 are targets of cyclin J–CDK–mediated immunometabolic regulation in macrophages. (**A**) Immunoblotting (IB) for FoxK1 in cytoplasmic and nuclear fractions and whole cell lysates (WCL) from RAW264.7 macrophages expressing DOX-inducible cyclin J 8 hours post-DOX treatment. The histograms indicate FoxK1 abundance as nucleus to cytoplasm ratio (n = 5) and total FoxK1 abundance (n = 3). Lamin B is a nuclear marker, tubulin is a cytoplasmic marker, and β-actin is a loading control. (**B**) Immunoblot analysis of FoxK1 in cytoplasmic and nuclear fractions of RAW264.7 macrophages stably expressing cyclin J following 4 hours of LPS stimulation. The histogram indicates FoxK1 abundance as nucleus to cytoplasm ratio (n = 3). **(C)** Expression of *Il1b*, *Il23a*, *Cxcl10*, and *Il10* in control or shFoxK1 KD RAW264.7 macrophages upon 6 hours of LPS stimulation (n = 3). **(D)** Immunoblot analysis and quantification of HIF-1α in control or shFoxK1 KD RAW264.7 macrophages. Blot is representative of n = 2. (**E**) Expression of *Il6* in control or shFoxK1 RAW264.7 macrophages expressing cyclin J and stimulated with LPS for 6 hours (n = 3). (**F**) Immunofluorescence microscopy showing mitochondria and nuclei in control and Drp1 KD RAW264.7 macrophages. The histogram represents mitochondrial interconnectivity (n = 10). Scale bar, 20 μm. (**G and H**) Representative flow cytometry histograms of mtROS (G) and cellular ROS (H) in control and shDrp1 KD macrophages upon LPS stimulation. Mean fluorescence intensity (MFI) values are noted in the flow cytometry plots. The histograms represents percentage of ROS^+ cells (n = 3). (**I**) *Il1b*, *Il23a*, *Cxcl10*, and *Il10* expression in control and shDrp1 KD RAW264.7 macrophages upon 6 hours of LPS stimulation (n = 3). (**J**) Immunoblot analysis and quantification of HIF-1α in control or shDrp1 KD RAW264.7 macrophages stimulated with LPS. Blot is representative of n = 2. **(K)** *Il6* expression in control and shDrp1 RAW264.7 macrophages constitutively expressing cyclin J after 6 hours of LPS

stimulation (*n* = 3). (**L**) Immunofluorescence microscopy showing mitochondria and nuclei in control and cyclin J–expressing RAW264.7 macrophages. The histogram represents mitochondrial interconnectivity (*n* = 6-7 independent experiments per group). Scale bar, 20 μm. Values are means ± SEM, where *n* indicates independent experiments (A, B, D, J), biological replicates (C, E, G, H, I, K), and individual cells per microscopy view (F and L). Statistical significance was determined by unpaired *t*-test (A, F, L), one-way ANOVA with Dunnett's multiple test (E and K) and two-way ANOVA with correction for multiple testing by Holm–Sidak method (B, C, G, H, I).

Fig. 6. Myeloid cell-intrinsic cyclin J suppresses host defense against bacterial infection. (A) Experimental design for LPS-induced endotoxic shock model. **(B)** Survival rate of *Ccnj*$^{fl/fl}$ and *Ccnj*$^{fl/fl}$LyzM-Cre^{+} mice intraperitoneally injected with LPS (*n* = 7). **(C)** Quantification of IL-6, IL-12p40, and TNF in sera collected from mice at indicated time points post-LPS injection, as measured by ELISA (*n* = 7). **(D)** Experimental design for *S. aureus* infection model. **(E)** Survival rate of *Ccnj*$^{fl/fl}$ and *Ccnj*$^{fl/fl}$LyzM-Cre^{+} mice intravenously inoculated with *S. aureus* (*n* = 7). **(F)** Quantification of IL-6, IL-12p40, and TNF in sera collected from mice at indicated time points post-*S. aureus* infection, as measured by ELISA (*n* = 7). **(G)** Bacterial burdens in liver, spleen, and kidney 2 and 4 days after *S. aureus* infection (*n* = 4). Values for (G) are means ± SEM; values for (C) and (F) are showed as means. *n* indicates the number of mice per genotype. Statistical significance was determined by Kaplan-Meier log-rank test for (B) and (E), while others were determined by two-way ANOVA with correction for multiple testing by Holm–Sidak method.

Fig. 7. Mice lacking Cyclin J in myeloid cells aggravates tumor growth in vivo. (A) Representative images of MC38 tumors harvested from *Ccnj*$^{fl/fl}$ and *Ccnj*$^{fl/fl}$LyzM-Cre^{+} mice and quantification of mean tumor volume (*n* = 6). **(B)** Representative images of B16-F10 tumors harvested from *Ccnj*$^{fl/fl}$ and *Ccnj*$^{fl/fl}$LyzM-Cre^{+} mice and quantification of mean tumor volume (*n* = 6). **(C)** Weights of MC38 tumors (*n* = 5 per group) and percentage of CD45^{+} tumor-infiltrating cells (*n* = 9 per group) in tumors harvested from *Ccnj*$^{fl/fl}$ and *Ccnj*$^{fl/fl}$LyzM-Cre^{+} mice 15 days after tumor cell injection. **(D)** Representative flow cytometry plots showing F4/80^{+}CD11b^{+} TAMs within the tumor. **(E)** Percentages of indicated immune cell subsets among CD45^{+} cells in the tumors (*n* = 4). **(F)** RT-qPCR analysis of the indicated transcripts in TAMs from *Ccnj*$^{fl/fl}$ and *Ccnj*$^{fl/fl}$LyzM-Cre^{+} mice (*n* = 3–5). **(G)** Comparison of differentially expressed genes from transcriptome analysis of TAMs (*Ccnj*$^{fl/fl}$ versus *Ccnj*$^{fl/fl}$LyzM-Cre^{+} mice). **(H)** GSEA analysis in hallmark and KEGG pathways derived from MSigDB collections in transcriptomic data from (G) and representative plots of the transcripts related to glycolysis and hypoxia. **(I)** Representative flow cytometry plot and mean fluorescence intensity (MFI) histogram of intracellular Glut1 protein in TAMs (*n* = 5). All values are means ± SEM, where *n* indicates the number of mice per genotype. Statistical significance was determined by unpaired *t*-test (C and I) and two-way ANOVA with correction for multiple testing by Holm–Sidak method (A, B, E, F).

Fig. 8. Schematic representation of the role of cyclin J in macrophages. In macrophages, TLR and IFN α/β receptor (IFNAR) stimulation induce the expression of *Ccnj*, which encodes cyclin J. Cyclin J interacts with CDK promote the phosphorylation of a set of substrates that includes FoxK1 and Drp1. Cyclin J–dependent FoxK1 phosphorylation excludes FoxK1 from the nucleus, thereby impeding its transcriptional control on genes encoding glycolytic enzymes.

Cyclin J–dependent Drp1 phosphorylation promotes mitochondrial fragmentation, thereby impairing mitochondrial activity and reducing ROS-induced Hif1α production. The dual modulation of glycolysis and mitochondrial activity by cyclin J reduces inflammatory responses, including antibacterial responses and antitumor immunity mediated by tumor-associated macrophages (TAMs).

Figure 1

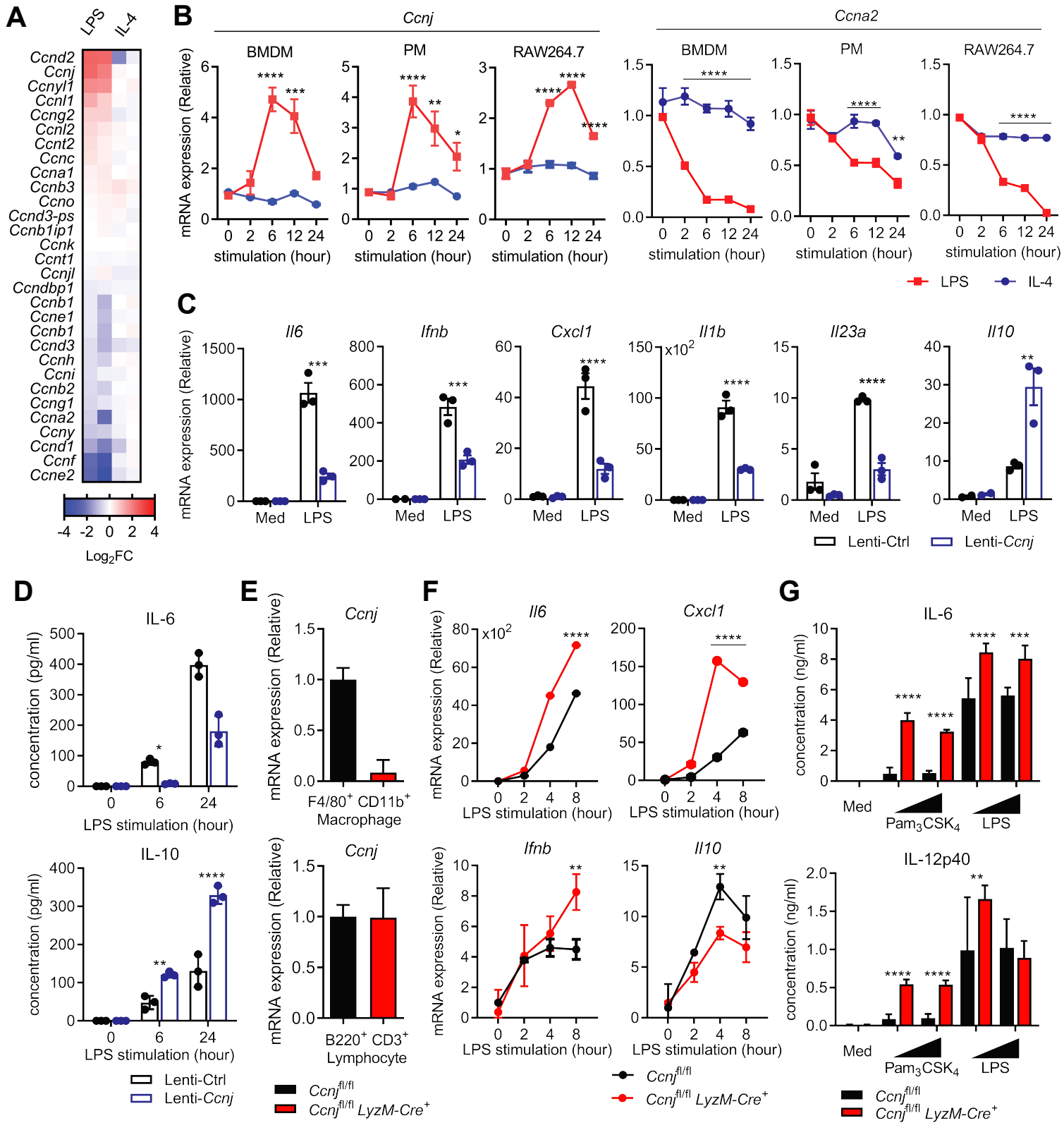
A
LPS
IL-4
Ccnd2
Ccnj
Ccnyl1
Ccnl1
Ccng2
Ccnl2
Ccnt2
Ccnc
Ccna1
Ccnb3
Ccno
Ccnd3-ps
Ccnb1ip1
Ccnk
Ccnt1
Ccnjl
Ccndbp1
Ccnb1
Ccne1
Ccnb1
Ccnd3
Ccnh
Ccni
Ccnb2
Ccng1
Ccna2
Ccny
Ccnd1
Ccnf
Ccne2
-4 -2 0 2 4
Log2FC
B
Ccnj
Ccna2
BMDM
PM
RAW264.7
mRNA expression (Relative)
stimulation (hour)
LPS
IL-4
C
Il6
Ifnb
Cxcl1
Il1b
Il23a
Il10
mRNA expression (Relative)
Med
LPS
Lenti-Ctrl
Lenti-Ccnj
D
IL-6
IL-10
concentration (pg/ml)
LPS stimulation (hour)
Lenti-Ctrl
Lenti-Ccnj
E
Ccnj
mRNA expression (Relative)
F4/80+ CD11b+
Macrophage
B220+ CD3+
Lymphocyte
Ccnjfl/fl
Ccnjfl/fl LyzM-Cre+
F
Il6
Cxcl1
Ifnb
Il10
mRNA expression (Relative)
LPS stimulation (hour)
Ccnjfl/fl
Ccnjfl/fl LyzM-Cre+
G
IL-6
IL-12p40
concentration (ng/ml)
Med
Pam3CSK4
LPS
Ccnjfl/fl
Ccnjfl/fl LyzM-Cre+

Figure 2

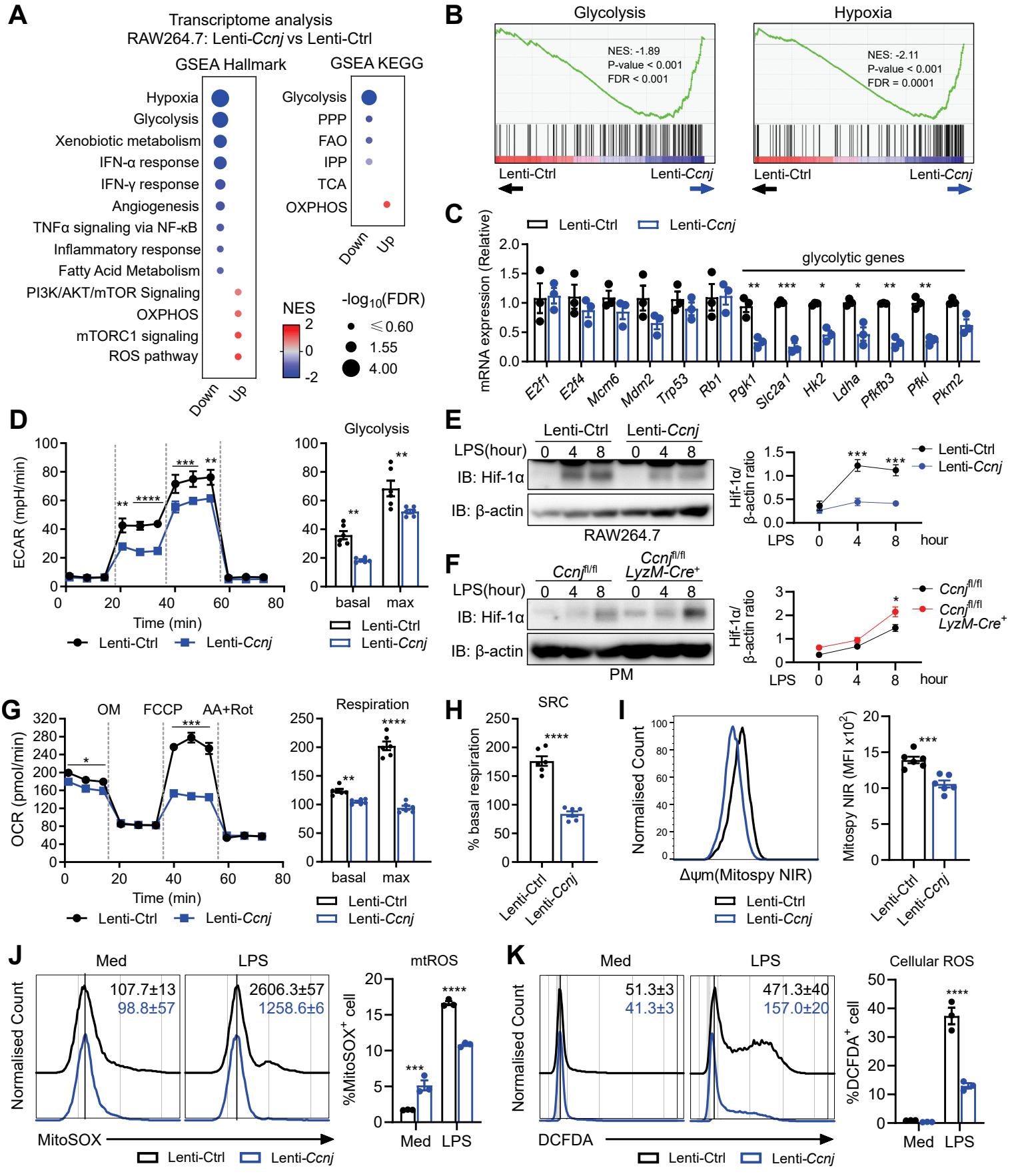
A
Transcriptome analysis
RAW264.7: Lenti-Ccnj vs Lenti-Ctrl
GSEA Hallmark
GSEA KEGG
Hypoxia
Glycolysis
Xenobiotic metabolism
IFN-α response
IFN-γ response
Angiogenesis
TNFα signaling via NF-κB
Inflammatory response
Fatty Acid Metabolism
PI3K/AKT/mTOR Signaling
OXPHOS
mTORC1 signaling
ROS pathway
PPP
FAO
IPP
TCA
OXPHOS
Down
Up
NES
-log10(FDR)
B
Glycolysis
NES: -1.89
P-value < 0.001
FDR < 0.001
Hypoxia
NES: -2.11
P-value < 0.001
FDR = 0.0001
Lenti-Ctrl
Lenti-Ccnj
C
mRNA expression (Relative)
glycolytic genes
E2f1
E2f4
Mcm6
Mdm2
Trp53
Rb1
Pgk1
Slc2a1
Hk2
Ldha
Pfkfb3
Pfkl
Pkm2
D
ECAR (mpH/min)
Time (min)
Glycolysis
basal
max
E
LPS(hour)
IB: Hif-1α
IB: β-actin
RAW264.7
Hif-1α/ β-actin ratio
hour
F
PM
G
OM
FCCP
AA+Rot
OCR (pmol/min)
Respiration
H
SRC
% basal respiration
I
Normalised Count
Δψm(Mitospy NIR)
Mitospy NIR (MFI x10²)
J
Med
LPS
107.7±13
98.8±57
2606.3±57
1258.6±6
MitoSOX
mtROS
%MitoSOX⁺ cell
K
51.3±3
41.3±3
471.3±40
157.0±20
DCFDA
Cellular ROS
%DCFDA⁺ cell

Figure 3

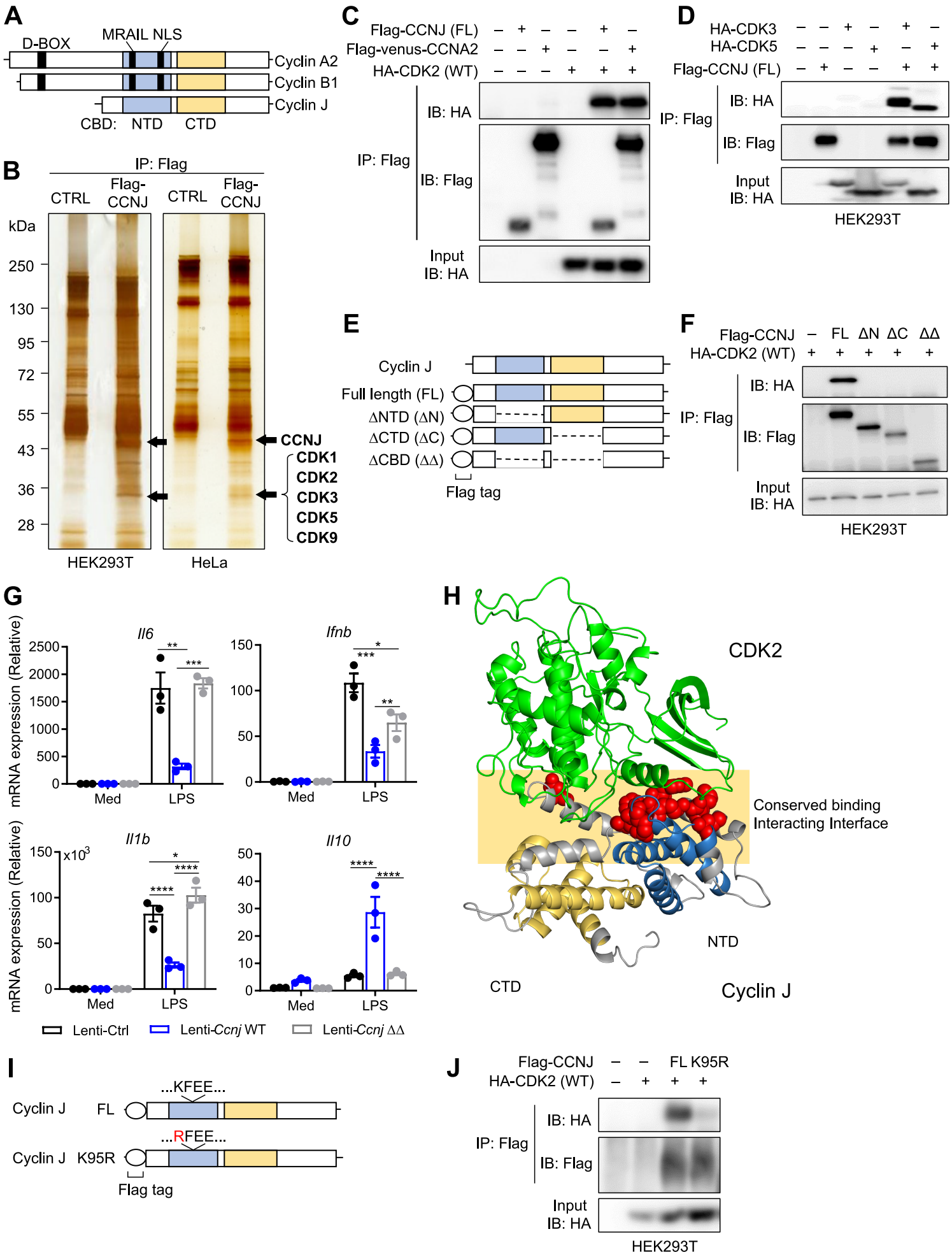
A
D-BOX
MRAIL NLS
Cyclin A2
Cyclin B1
Cyclin J
CBD: NTD CTD
B
IP: Flag
CTRL
Flag-CCNJ
CTRL
Flag-CCNJ
kDa
250
130
95
72
55
43
36
28
CCNJ
CDK1
CDK2
CDK3
CDK5
CDK9
HEK293T
HeLa
C
Flag-CCNJ (FL)
Flag-venus-CCNA2
HA-CDK2 (WT)
IP: Flag
IB: HA
IB: Flag
Input
IB: HA
D
HA-CDK3
HA-CDK5
Flag-CCNJ (FL)
IP: Flag
IB: HA
IB: Flag
Input
IB: HA
HEK293T
E
Cyclin J
Full length (FL)
ΔNTD (ΔN)
ΔCTD (ΔC)
ΔCBD (ΔΔ)
Flag tag
F
Flag-CCNJ
FL
ΔN
ΔC
ΔΔ
HA-CDK2 (WT)
IP: Flag
IB: HA
IB: Flag
Input
IB: HA
HEK293T
G
mRNA expression (Relative)
Il6
Ifnb
Il1b
Il10
x10^3
Med
LPS
Lenti-Ctrl
Lenti-Ccnj WT
Lenti-Ccnj ΔΔ
H
CDK2
Conserved binding
Interacting Interface
NTD
CTD
Cyclin J
I
Cyclin J FL
...KFEE...
Cyclin J K95R
...RFEE...
Flag tag
J
Flag-CCNJ
FL
K95R
HA-CDK2 (WT)
IP: Flag
IB: HA
IB: Flag
Input
IB: HA
HEK293T

Figure 4

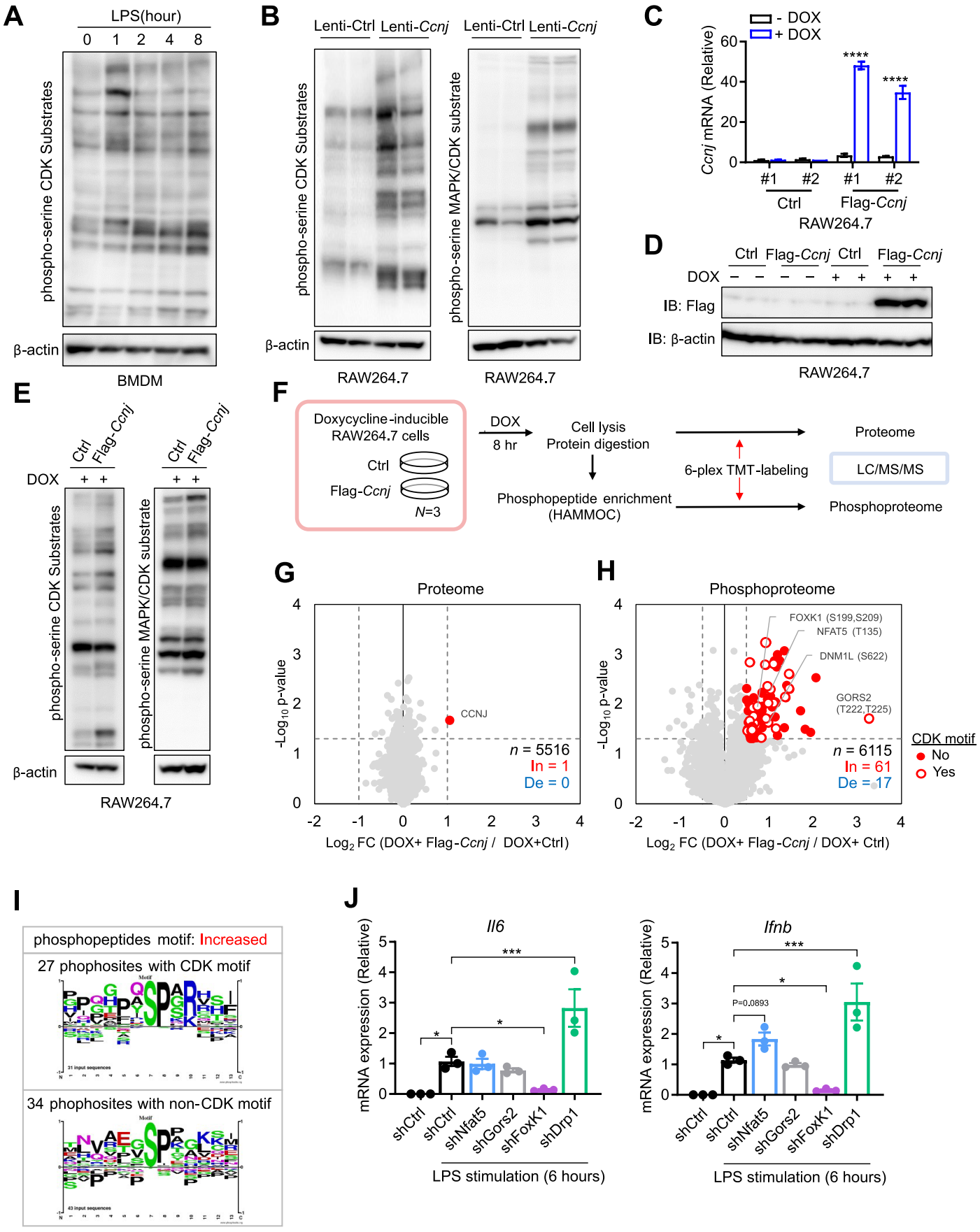
A
LPS(hour)
0 1 2 4 8
phospho-serine CDK Substrates
β-actin
BMDM
B
Lenti-Ctrl Lenti-Ccnj Lenti-Ctrl Lenti-Ccnj
phospho-serine CDK Substrates
phospho-serine MAPK/CDK substrate
β-actin
RAW264.7
RAW264.7
C
- DOX
+ DOX
Ccnj mRNA (Relative)
60
40
20
0
****
****
#1 #2 #1 #2
Ctrl
Flag-Ccnj
RAW264.7
D
Ctrl Flag-Ccnj Ctrl Flag-Ccnj
DOX – – – – + + + +
IB: Flag
IB: β-actin
RAW264.7
E
Ctrl Flag-Ccnj Ctrl Flag-Ccnj
DOX + + + +
phospho-serine CDK Substrates
phospho-serine MAPK/CDK substrate
β-actin
RAW264.7
F
Doxycycline-inducible RAW264.7 cells
Ctrl
Flag-Ccnj
N=3
DOX
8 hr
Cell lysis
Protein digestion
Phosphopeptide enrichment (HAMMOC)
6-plex TMT-labeling
Proteome
LC/MS/MS
Phosphoproteome
G
Proteome
-Log10 p-value
CCNJ
n = 5516
In = 1
De = 0
Log2 FC (DOX+ Flag-Ccnj / DOX+Ctrl)
H
Phosphoproteome
FOXK1 (S199,S209)
NFAT5 (T135)
DNM1L (S622)
GORS2 (T222,T225)
n = 6115
In = 61
De = 17
Log2 FC (DOX+ Flag-Ccnj / DOX+ Ctrl)
CDK motif
No
Yes
I
phosphopeptides motif: Increased
27 phophosites with CDK motif
34 phophosites with non-CDK motif
J
Il6
Ifnb
mRNA expression (Relative)
***
*
P=0.0893
shCtrl
shCtrl
shNfat5
shGors2
shFoxK1
shDrp1
LPS stimulation (6 hours)

Figure 5

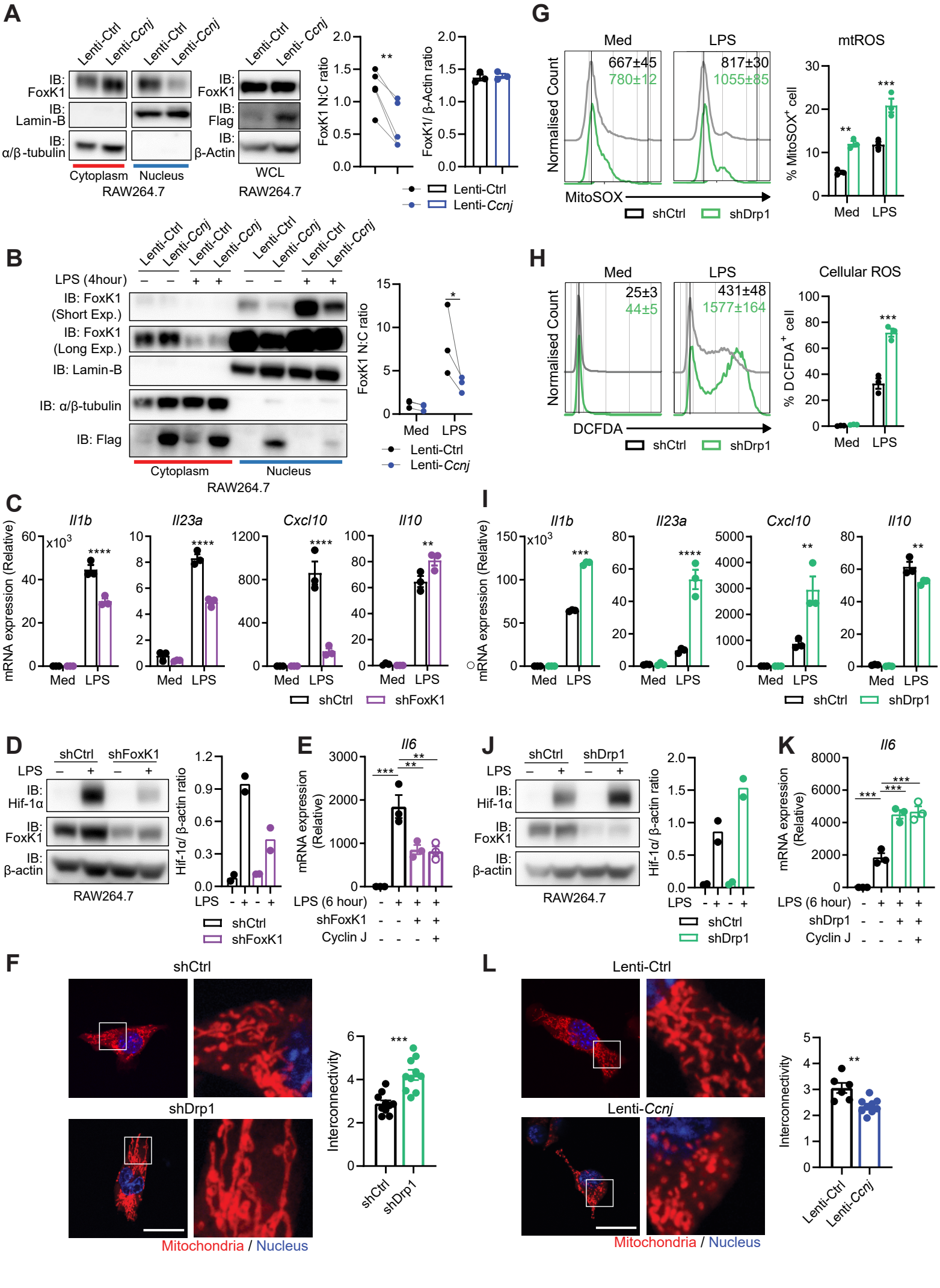
A
Lenti-Ctrl
Lenti-Ccnj
IB: FoxK1
IB: Lamin-B
IB: α/β-tubulin
Cytoplasm
Nucleus
RAW264.7
IB: FoxK1
IB: Flag
IB: β-Actin
WCL
RAW264.7
FoxK1 N:C ratio
FoxK1/ β-Actin ratio
Lenti-Ctrl
Lenti-Ccnj
B
LPS (4hour)
IB: FoxK1 (Short Exp.)
IB: FoxK1 (Long Exp.)
IB: Lamin-B
IB: α/β-tubulin
IB: Flag
Cytoplasm
Nucleus
RAW264.7
FoxK1 N:C ratio
Med
LPS
Lenti-Ctrl
Lenti-Ccnj
C
Il1b
Il23a
Cxcl10
Il10
mRNA expression (Relative)
x10^3
Med
LPS
shCtrl
shFoxK1
D
shCtrl
shFoxK1
LPS
IB: Hif-1α
IB: FoxK1
IB: β-actin
RAW264.7
Hif-1α/ β-actin ratio
shCtrl
shFoxK1
E
Il6
mRNA expression (Relative)
LPS (6 hour)
shFoxK1
Cyclin J
F
shCtrl
shDrp1
Mitochondria / Nucleus
Interconnectivity
shCtrl
shDrp1
G
Med
LPS
667±45
780±12
817±30
1055±85
Normalised Count
MitoSOX
shCtrl
shDrp1
mtROS
% MitoSOX+ cell
H
Med
LPS
25±3
44±5
431±48
1577±164
Normalised Count
DCFDA
shCtrl
shDrp1
Cellular ROS
% DCFDA+ cell
I
Il1b
Il23a
Cxcl10
Il10
mRNA expression (Relative)
x10^3
Med
LPS
shCtrl
shDrp1
J
shCtrl
shDrp1
LPS
IB: Hif-1α
IB: FoxK1
IB: β-actin
RAW264.7
Hif-1α/ β-actin ratio
shCtrl
shDrp1
K
Il6
mRNA expression (Relative)
LPS (6 hour)
shDrp1
Cyclin J
L
Lenti-Ctrl
Lenti-Ccnj
Mitochondria / Nucleus
Interconnectivity
Lenti-Ctrl
Lenti-Ccnj

Figure 6

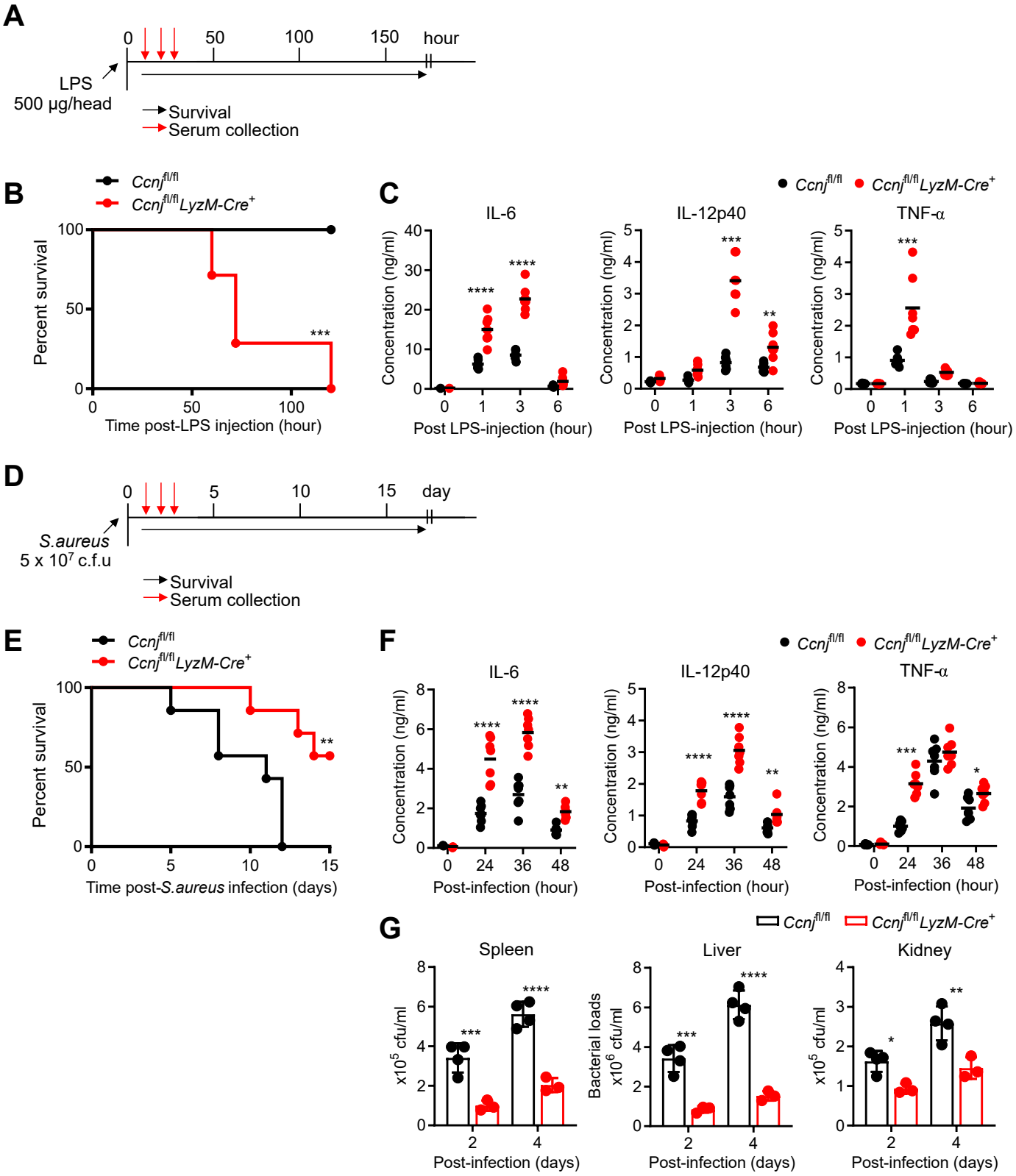
A
0
50
100
150
hour
LPS
500 µg/head
Survival
Serum collection
B
Ccnj fl/fl
Ccnj fl/fl LyzM-Cre+
Percent survival
Time post-LPS injection (hour)
C
Ccnj fl/fl
Ccnj fl/fl LyzM-Cre+
IL-6
IL-12p40
TNF-α
Concentration (ng/ml)
Post LPS-injection (hour)
D
0
5
10
15
day
S.aureus
5 x 10^7 c.f.u
Survival
Serum collection
E
Ccnj fl/fl
Ccnj fl/fl LyzM-Cre+
Percent survival
Time post-S.aureus infection (days)
F
Ccnj fl/fl
Ccnj fl/fl LyzM-Cre+
IL-6
IL-12p40
TNF-α
Concentration (ng/ml)
Post-infection (hour)
G
Ccnj fl/fl
Ccnj fl/fl LyzM-Cre+
Spleen
Liver
Kidney
x10^5 cfu/ml
Bacterial loads x10^6 cfu/ml
Post-infection (days)

Figure 7

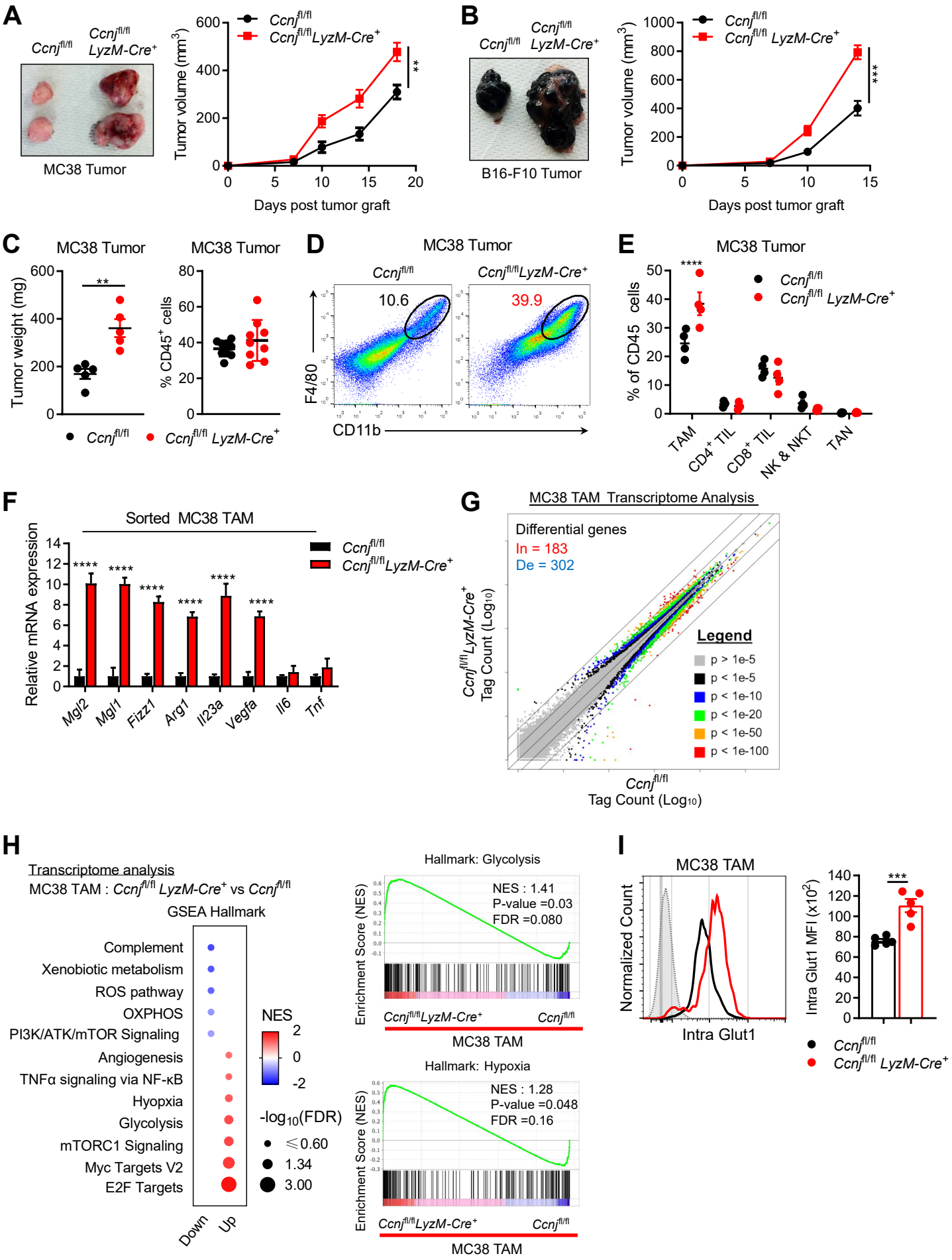
A
Ccnj fl/fl
Ccnj fl/fl LyzM-Cre+
MC38 Tumor
Tumor volume (mm3)
Days post tumor graft
B
B16-F10 Tumor
C
MC38 Tumor
Tumor weight (mg)
% CD45+ cells
D
10.6
39.9
F4/80
CD11b
E
% of CD45 cells
TAM
CD4+ TIL
CD8+ TIL
NK & NKT
TAN
F
Sorted MC38 TAM
Relative mRNA expression
Mgl2
Mgl1
Fizz1
Arg1
Il23a
Vegfa
Il6
Tnf
G
MC38 TAM Transcriptome Analysis
Differential genes
In = 183
De = 302
Legend
p > 1e-5
p < 1e-5
p < 1e-10
p < 1e-20
p < 1e-50
p < 1e-100
Tag Count (Log10)
H
Transcriptome analysis
MC38 TAM : Ccnj fl/fl LyzM-Cre+ vs Ccnj fl/fl
GSEA Hallmark
Complement
Xenobiotic metabolism
ROS pathway
OXPHOS
PI3K/ATK/mTOR Signaling
Angiogenesis
TNFα signaling via NF-κB
Hyopxia
Glycolysis
mTORC1 Signaling
Myc Targets V2
E2F Targets
Down
Up
NES
-log10(FDR)
Hallmark: Glycolysis
NES : 1.41
P-value =0.03
FDR =0.080
Enrichment Score (NES)
MC38 TAM
Hallmark: Hypoxia
NES : 1.28
P-value =0.048
FDR =0.16
I
MC38 TAM
Normalized Count
Intra Glut1
Intra Glut1 MFI (x10²)

Figure 8

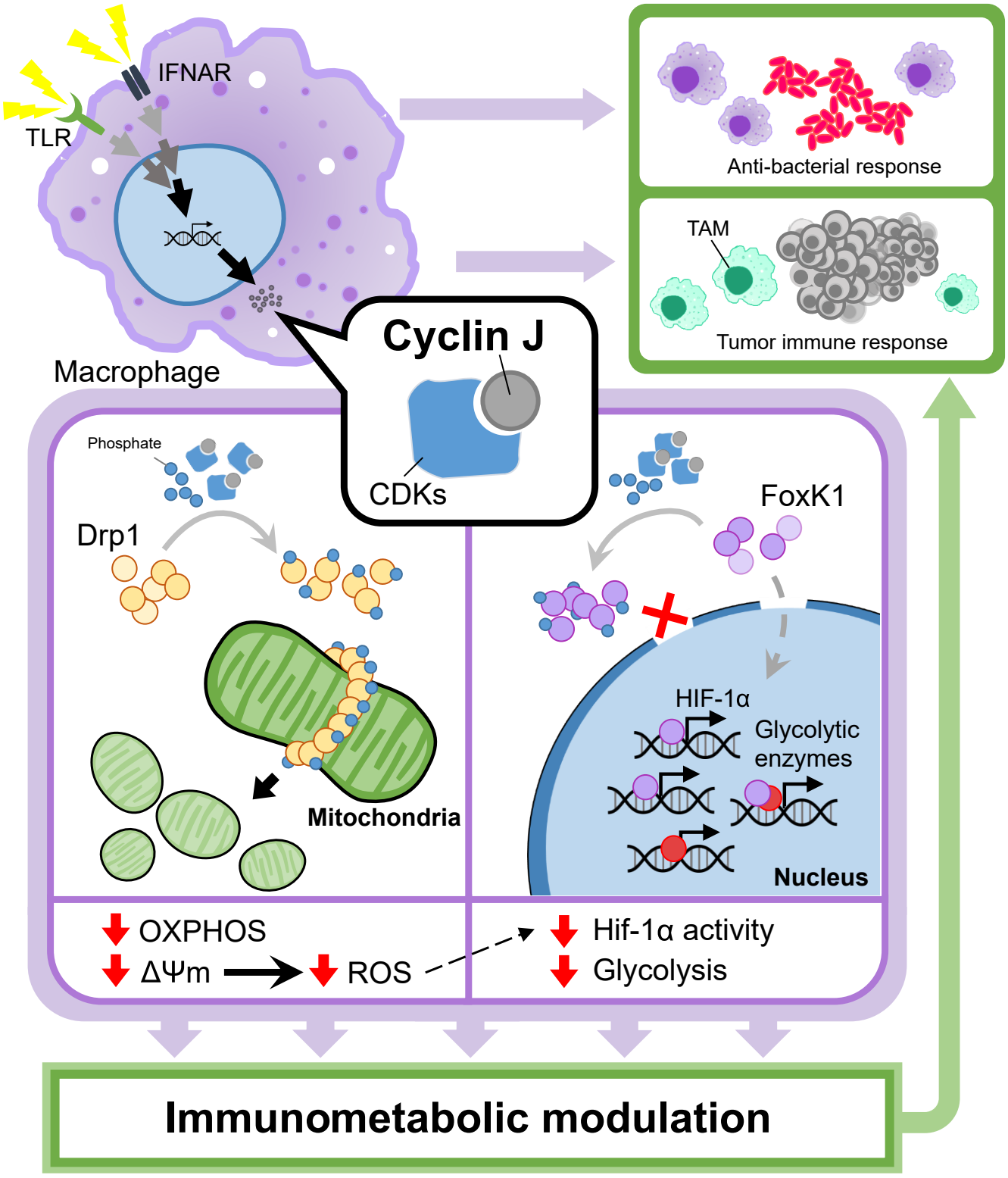
IFNAR
TLR
Macrophage
Cyclin J
CDKs
Anti-bacterial response
TAM
Tumor immune response
Phosphate
Drp1
Mitochondria
FoxK1
HIF-1α
Glycolytic enzymes
Nucleus
OXPHOS
ΔΨm
ROS
Hif-1α activity
Glycolysis
Immunometabolic modulation

Supplementary Materials

Fig. S1. *Ccnj* induction in macrophages. (**A**) Expression of *Ccnj* in BMDMs with different stimulations or media alone (Med) at indicated time points by RT-qPCR (n =3). (**B**) Heatmap showing expression of genes encoding cyclin family members in BMDMs upon LPS (100 ng/mL), Pam_3CSK_4 (100 ng/mL) and Poly(I:C) (20 ng/mL) stimulation. Data represent log_2 fold change of treated over unstimulated BMDM and are derived from public database (GSE81291). (**C**) Expression of *Ccnj* in PMs upon stimulation with indicated TLR ligands or media alone (Med), and in increasing dose of stimulants by RT-qPCR (n =3). (**D and E**) Expression of *Ccnj* and *Il6* in PMs (D) and BMDMs (E) harvested from WT and *MyD88*$^{-/-}$ mice with LPS stimulation or media alone (Med) for 6 hours by RT-qPCR (n = 2). (**F**) Heatmap showing gene expression of genes encoding cyclin family members in BMDM upon IFN-α or IFN-γ stimulation for 2.5 hours. Data represent log_2 fold change of treated over unstimulated BMDMs and are derived from public database (GSE35825). (**G**) Expression of *Ccnj* in macrophages upon IFN-α (20ng/ml) or IFN-γ (20ng/ml) stimulation at indicated time points by RT-qPCR (n = 3). (**H**) Comparison of differentially expressed genes in human macrophage (control versus IFN-α). Data are derived from public database (GSE16755). (**I**) Representative flow cytometry histogram of cell cycle in HeLa cells upon release from Thymidine-induced mitotic arrest and expression of gene encoding various cyclin members at indicated time point upon release post-mitotic arrest (n =3). (**J**) Representative flow cytometry histogram of cell cycle in RAW264.7 macrophages upon release from nocodazole-induced mitotic arrest and expression of encoding various cyclin members at indicated time point upon release post-mitotic arrest (n =3). Value shown mean ± SEM, where n indicates biological replicates. For (A) and (G), statistical significance was determined by two-way ANOVA with correction for multiple testing by Holm–Sidak method. For (C), one-way ANOVA with Dunnett's multiple test was used.

Fig. S2. Establishment and characterization of cyclin J overexpressing RAW264.7 cell line. (**A**) Construct of Lentiviral plasmid for establishment of stable RAW264.7 cell line with luciferase gene act as control and mouse cyclin J gene with flag protein attached. (**B and C**) Confirmation of cyclin J expression in selected clones through RT-qPCR (n = 2) (B) and Immunoblot analysis (C). (**D**) Expression of *Il6* in selected clones of RAW264.7 macrophages upon LPS stimulations for 6 hours by RT-qPCR (n = 2). (**E**) *Isg15* and *Cxcl10* gene expression in cyclin J–expressing or control RAW264.7 macrophages upon stimulation with LPS or media alone (Med) for 6 hours by RT-qPCR (n = 3). (**F**) *Ifnb* and *Cxcl10* gene expression in cyclin J–expressing or control RAW264.7 macrophages upon stimulation with Poly (I:C) or media alone (Med) for 6 hours by RT-qPCR (n = 3). (**G and H**) Expression of gene encoding Interferon-stimulate genes (ISGs) in in cyclin J–expressing or control RAW264.7 macrophages upon stimulation with IFN-γ (G) or IFN-α (H) in comparison to media alone (Med) for 6 hours by RT-qPCR (n = 3). All values are means ± SEM, where n indicates biological replicates. Statistical significance was determined by two-way ANOVA with correction for multiple testing by Holm–Sidak method.

Fig. S3. Generation and characterization of Myeloid-specific cyclin J knockout mice. (**A**) Schematic representation of the targeting strategy. A targeting construct was designed to flank exon 3 of the cyclin J gene and the Neo^r gene with loxP sites (triangles). (**B**) Southern blot analysis of *PstI*-digested genomic DNA from the positive clones. (**C**) Expression of indicated genes in BMDMs harvested from *Ccnj*$^{fl/fl}$ and *Ccnj*$^{fl/fl}$LyzM-Cre$^+$ mice upon 6 hours of LPS stimulation or media alone (Med) by RT-qPCR (n = 3). (**D**) Expression of pro-inflammatory

cytokine genes in peritoneal neutrophils from *Ccnj*$^{fl/fl}$ and *Ccnj*$^{fl/fl}$LyzM-Cre^{+} mice upon LPS stimulation at indicated time point by RT-qPCR (*n* = 3). (**E**) Quantification of IL-6 and IL-10 by ELISA in media of peritoneal neutrophils from *Ccnj*$^{fl/fl}$ and *Ccnj*$^{fl/fl}$LyzM-Cre^{+} mice upon in vitro Pam_3CSK_4 or LPS stimulation for 24 hours by ELISA (*n* = 3). (**F**) Flow cytometric analysis of Ki-67^{+} PM and BMDMs from *Ccnj*$^{fl/fl}$ and *Ccnj*$^{fl/fl}$LyzM-Cre^{+} mice cultured with media alone or M-CSF (20ng/ml). (**G**) Expression of genes encoding cyclin family member in BMDMs upon LPS or M-CSF stimulation at indicated time points by RT-qPCR (*n* = 3). All values are means ± SEM, where *n* indicates biological replicates. Statistical significance was determined by two-way ANOVA with correction for multiple testing by Holm–Sidak method.

Fig. S4. Effect of cyclin J in the TLR-related signaling. (**A and B**) Immunoblot analysis of Lentiviral-transduced RAW264.7 macrophages (A) and PM (B) upon LPS stimulation at indicated time points with antibody against p-JNK, p-p38, JNK, p38, and IκBα. β-actin is a loading control. Blots are representative of *n* = 2.

Fig. S5. Effect of cyclin J on glycolysis and OXPHOS. (A) Expression heatmap showing expression of genes related to glycolysis in Lenti-Ctrl and Lenti-*Ccnj* RAW264.7 macrophage from Fig 3A. Data represent log_2 expression value transformed into z-score **(B)** ATP quantification in Lenti-Ctrl and Lenti-*Ccnj* RAW264.7 macrophages (*n* = 6). **(C)** Number of mitochondrial DNA (mtDNA) copy number in Lenti-Ctrl and Lenti-*Ccnj* RAW264.7 macrophages (*n* = 3). **(D)** *Sod1*. *Sod2*, and *Cat* gene expression in Lenti-Ctrl and Lenti-*Ccnj* RAW264.7 macrophages upon stimulated with LPS or media alone (Med) for 6 hours by RT-qPCR (*n* = 3). Value shown mean ± SEM where *n* indicates biological replicates. Statistical significance was determined by unpaired t-test for (B and C), and two-way ANOVA with correction for multiple testing by Holm–Sidak method (D).

Fig. S6. Cyclin J molecular characterization. (**A**) Immunoblot (IB) analysis for HA and Flag in Flag immunoprecipitates from lysates of HeLa and HEK293T cells coexpressing Flag-tagged CCNJ (cyclin J) and HA-tagged CDKs. Blot is representative of 3 independent experiments. (**B**) Immunofluorescence microscopy showing localization of Flag-tagged CCNJ in transfected HEK293T cells by co-staining with antibody against □/β-tubulin, Hoechst 33258, and Flag. Scale bar, 20 μm. (**C**) Alignment of cyclin proteins which are reported to bind CDK2. Conserved binding interface residues of the mouse cyclin J (those identical to any aligned residues from the representative structures known on CDK2 binding interface) were identified and boxed. The boxed residues are indicated as red spheres in Fig. 3H. Sequence alignment was visualized by UCSF Chimera program. Immunoblot is representative of two independent experiments.

Fig. S7. Verification of experimental approach in capturing CDK substrate using cell cycle-synchronization and CDK inhibition approaches. (**A and B**) Schematic view of acquisition of phosphoproteomic data from RAW264.7 macrophages after cell cycle synchronization with or without CDK inhibitor (A). Cell extracts were collected and checked with immunoblot using an antibody that recognizes phosphorylated serine in the CDK substrate consensus motif, (K/H)pSP (B) and proceed to phosphopeptide enrichment by hydroxy acid-modified metal-oxide chromatography (HAMMOC) prior to liquid chromatography with tandem mass spectrometry (LC/MS/MS). Blot is representative of 2 independent experiments. (**C**) Scatter plots showing phosphopeptide changes in Log_2FC (Nocodazole treated/ untreated) and Log_2FC

(FVP+Nocodazole treated/ Nocodazole treated) (upper) or Log_2FC (ROS+Nocodazole treated/ Nocodazole treated) (bottom). Blue dot indicates activated phosphopeptides that can be suppressed by CDK inhibitors. (**D**) Logo analysis of activated phosphorylation sites in nocodazole treated sample in C. (**E**) Logo analysis of suppressed phosphorylation sites in CDK inhibitors + nocodazole treated sample in C.

Fig. S8. Verification of lentiviral knockdown in RAW264.7 macrophages. Expression of *Nfat5*, *Gorasp2*, *Foxk1*, and *Dnm1l* in control or lentiviral knockdown RAW264.7 macrophages by RT-qPCR ($n = 3$). Values represent mean ± SEM, where *n* indicates biological replicates. Statistical significance was determined by one-way ANOVA with Dunnett's multiple test.

Fig. S9. Roles of FoxK1 in macrophage under cyclin J influence. (**A**) Schematic view of phosphosites on FoxK1 and homology comparison with multiple species. (**B**) Immunoblot analysis of phosphoserine FoxK1 protein in RAW264.7 macrophages expressing inducible cyclin J 8 hours post DOX treatment. Quantification of phosphorylation state relative to non-DOX stimulation was shown in the histogram ($n = 2$). (**C**) Immunoblotting for FoxK1 in subcellular fractions and whole cell extract (WCL) harvested from RAW264.7 macrophages constitutively expressing cyclin J. The histograms indicate FoxK1 abundance as nucleus to cytoplasm ratio ($n = 3$) and total FoxK1 abundance ($n = 3$). Lamin B is a nuclear marker, tubulin is a cytoplasmic marker, and β-actin is a loading control. (**D**) Immunoblot analysis of Myc-tagged WT and mutant (Mut) FoxK1 proteins in cytoplasmic and nuclear fractions with or without co-expression of Flag-tagged Cyclin J in HEK293T cells. The histogram indicates FoxK1 abundance as nucleus to cytoplasm ratio ($n = 3$). (**E**) Immunoblot of Hif-1α and FoxK1 subcellular abundance in RAW264.7 macrophages at indicated time point post LPS stimulation. Blot is representative of $n = 2$. (**F**) Expression of HIF-1α gene in control or shFoxK1 KD RAW264.7 macrophages by RT- qPCR ($n = 3$). (**G**) Expression of HIF-1α target genes expression in control or shFoxK1 KD RAW264.7 macrophages upon 6 hours of LPS stimulation by RT-qPCR ($n = 3$). (**H**) Cyclin J gene expression in control or lentiviral knockdown macrophages by RT-qPCR ($n = 3$). Values for histograms represent mean ± SEM, where *n* indicates independent experiments (C and D) or biological replicates in (B, F, G, H), respectively. Statistical significance was determined by unpaired t-test (C and B) or two-way ANOVA with correction for multiple testing by Holm–Sidak method (D, F, G).

Fig. S10. Roles of Drp1 in macrophage under cyclin J influence. (**A**) Schematic view of phosphosites on Drp1 and homology comparison with multiple species across various species. (**B and C**) Immunoblot analysis of Drp1 phosphorylation in in RAW264.7 cells treated with DOX to induce expression of Flag-tagged cyclin J (Flag-*Ccnj*) (B) and HEK293T cells transfected with Flag-CCNJ constructs (C), histograms show quantification of Drp1 phosphorylation state in respective immunoblots ($n = 3$ for each panel). (**D**) Mitochondrial morphology of control and shDrp1 KD RAW264.7 macrophages with electron microscopy. Arrows indicate mitochondria. Scale bar, 1 μm. (**E and F**) Mitochondrial stress test of control and shDrp1 KD macrophages ($n = 6$), histogram represents spare respiratory capacity (F). (**G**) *Il6* and *Dnm1l* gene expression in control or shDrp1 KD RAW264.7 clones by RT-qPCR ($n = 3$). (**H**) Mitochondrial morphology of Lenti-Ctrl and Lenti-*Ccnj* RAW264.7 macrophages with electron microscopy. Arrows indicate mitochondria. Scale bar, 1 μm. Values represent mean ± SEM. For (B) and (C), *n* represent individual experiments. For (E) to (G), *n* indicates biological replicate. Statistical significance was determined by unpaired t-test (F), one-way ANOVA with Dunnett's multiple

test (B and C), or two-way ANOVA with correction for multiple testing by Holm–Sidak method (E).

Fig. S11. Cyclin J role in macrophage-mediated tumor immune response. (**A**) The gating strategy in sorting TAMs from tumor sample by flow cytometry. (**B**) RT-qPCR analysis for *Ccnj*, *Arg1*, and *Vegfa* expression in indicated macrophages (n = 3 - 4). BMDMs and PMs were harvested from tumor-free mice, while TAMs were sorted from WT mice 15 days after subcutaneous injection of MC38 tumor cells. (**C**) Schematics for MC38 and B16-F10 tumor xenograft model in Fig. 7. (**D**) Scheme for AOM-DSS tumor induction model. (**E**) Body weight change in mice throughout the course of AOM-DSS (n = 6 - 7). (**F**) Representative images of the colon from both *Ccnj*$^{fl/fl}$ and *Ccnj*$^{fl/fl}$LyzM-Cre^{+} mice at the end of AOM-DSS treatment. (**G**) Tumor number and tumor burden in mice at the end of AOM-DSS treatment (n = 6 - 7). (**H**) Representative flow cytometry plots showing Ki-67 level in F4/80^{+}CD11b^{+} TAMs within tumor. Histogram panel shows the percentage of Ki-67^{+} cells in TAMs (n = 5). (**I**) Gene-set enrichment analysis showing normalized enrichment score of 3368 gene sets from the curated collection (C2) of the GSEA molecular signatures database v3.0, where solid red circles highlight gene-sets involving hypoxia and Hif-1α targets. Dotted line represents threshold of FDR value (0.25). Representative plot of the transcripts related Hif-1α targets (ELVIDGE_HIF1A_AND_HIF2A_TARGETS_DN). (**J**) Expression heatmap showing expression of DEGs related to hypoxia and glycolysis in MC38 TAM. Data represent rpkm value transformed into z-score. All values are means ± SEM where n indicates biological replicates (B) or number of mice per genotype (E to H). Statistical significance was determined by two-way ANOVA with correction for multiple testing by Holm–Sidak method.

Figure S1

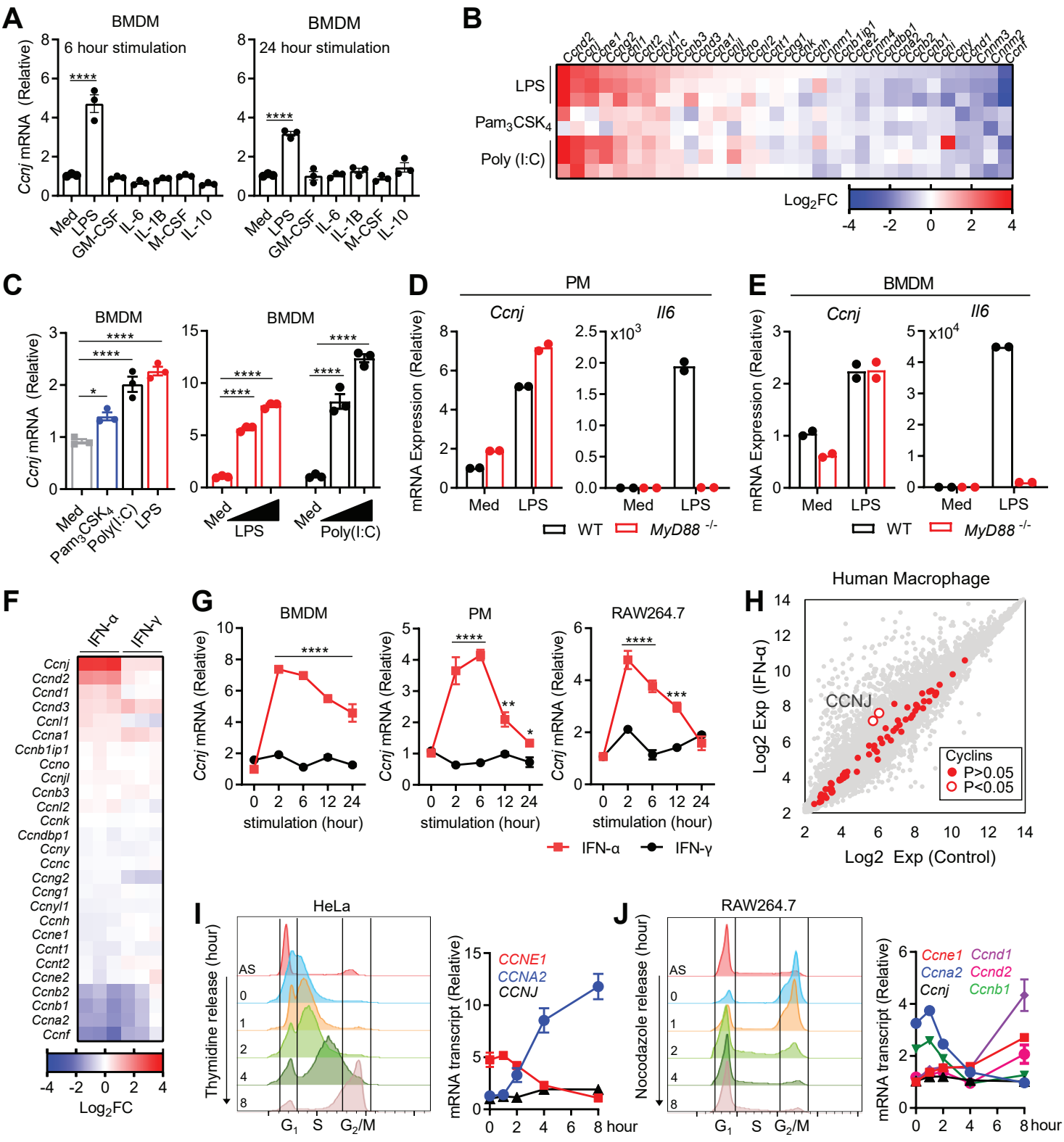
A
BMDM
6 hour stimulation
24 hour stimulation
Ccnj mRNA (Relative)
Med
LPS
GM-CSF
IL-6
IL-1B
M-CSF
IL-10
B
LPS
Pam3CSK4
Poly (I:C)
Log2FC
C
BMDM
Ccnj mRNA (Relative)
Pam3CSK4
Poly(I:C)
D
PM
Ccnj
Il6
mRNA Expression (Relative)
WT
MyD88 -/-
E
BMDM
F
IFN-α
IFN-γ
G
BMDM
PM
RAW264.7
Ccnj mRNA (Relative)
stimulation (hour)
H
Human Macrophage
Log2 Exp (IFN-α)
Log2 Exp (Control)
CCNJ
Cyclins
P>0.05
P<0.05
I
HeLa
Thymidine release (hour)
mRNA transcript (Relative)
CCNE1
CCNA2
CCNJ
J
RAW264.7
Nocodazole release (hour)
Ccne1
Ccnd1
Ccna2
Ccnd2
Ccnj
Ccnb1
hour

Figure S2

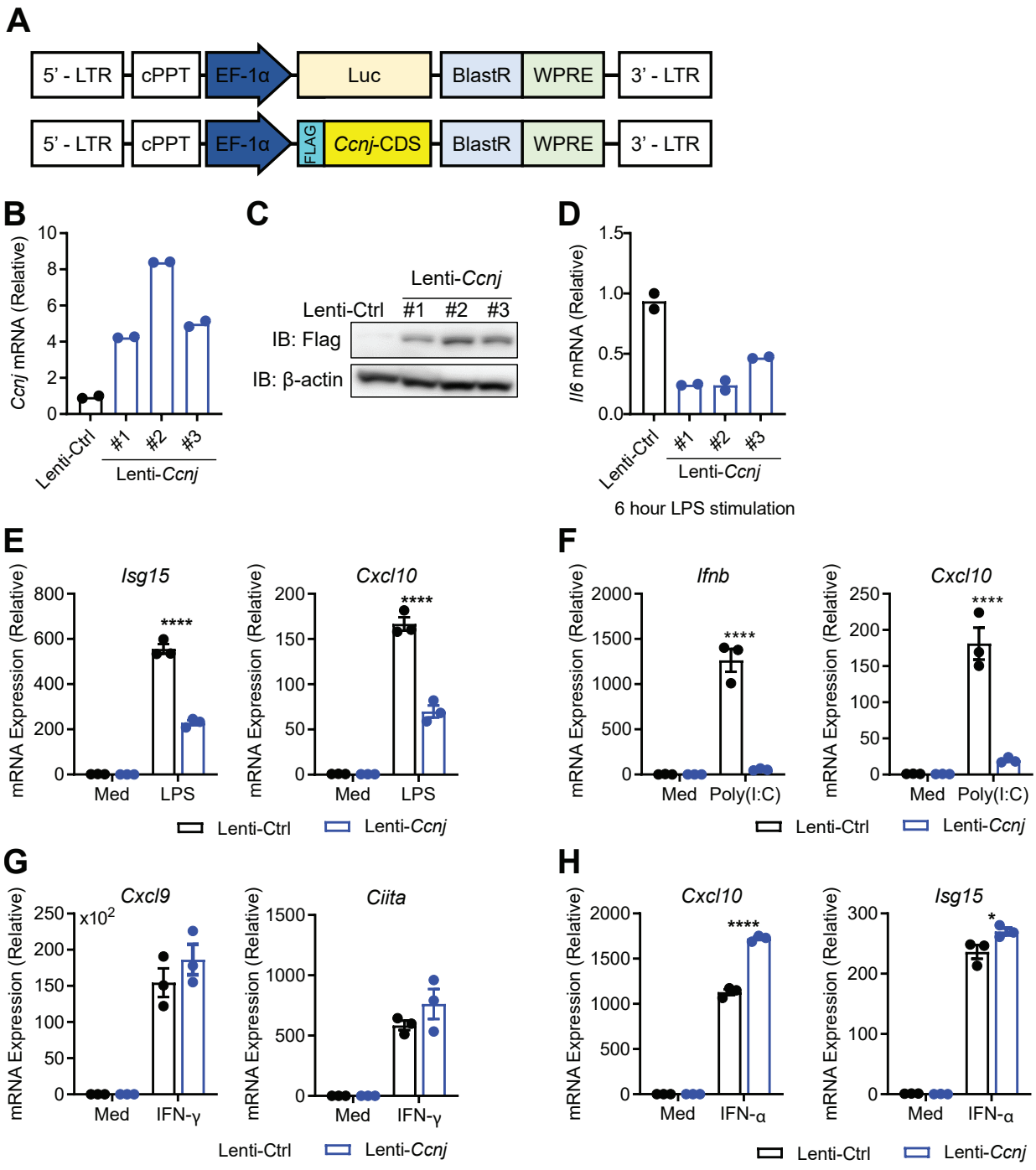
A
5' - LTR
cPPT
EF-1α
Luc
BlastR
WPRE
3' - LTR
5' - LTR
cPPT
EF-1α
FLAG
Ccnj-CDS
BlastR
WPRE
3' - LTR
B
Ccnj mRNA (Relative)
Lenti-Ctrl
#1
#2
#3
Lenti-Ccnj
C
Lenti-Ccnj
Lenti-Ctrl
#1
#2
#3
IB: Flag
IB: β-actin
D
Il6 mRNA (Relative)
Lenti-Ctrl
#1
#2
#3
Lenti-Ccnj
6 hour LPS stimulation
E
Isg15
Cxcl10
mRNA Expression (Relative)
****
Med
LPS
Lenti-Ctrl
Lenti-Ccnj
F
Ifnb
Cxcl10
mRNA Expression (Relative)
****
Med
Poly(I:C)
Lenti-Ctrl
Lenti-Ccnj
G
Cxcl9
Ciita
mRNA Expression (Relative)
x10^2
Med
IFN-γ
Lenti-Ctrl
Lenti-Ccnj
H
Cxcl10
Isg15
mRNA Expression (Relative)
****
*
Med
IFN-α
Lenti-Ctrl
Lenti-Ccnj

Figure S3

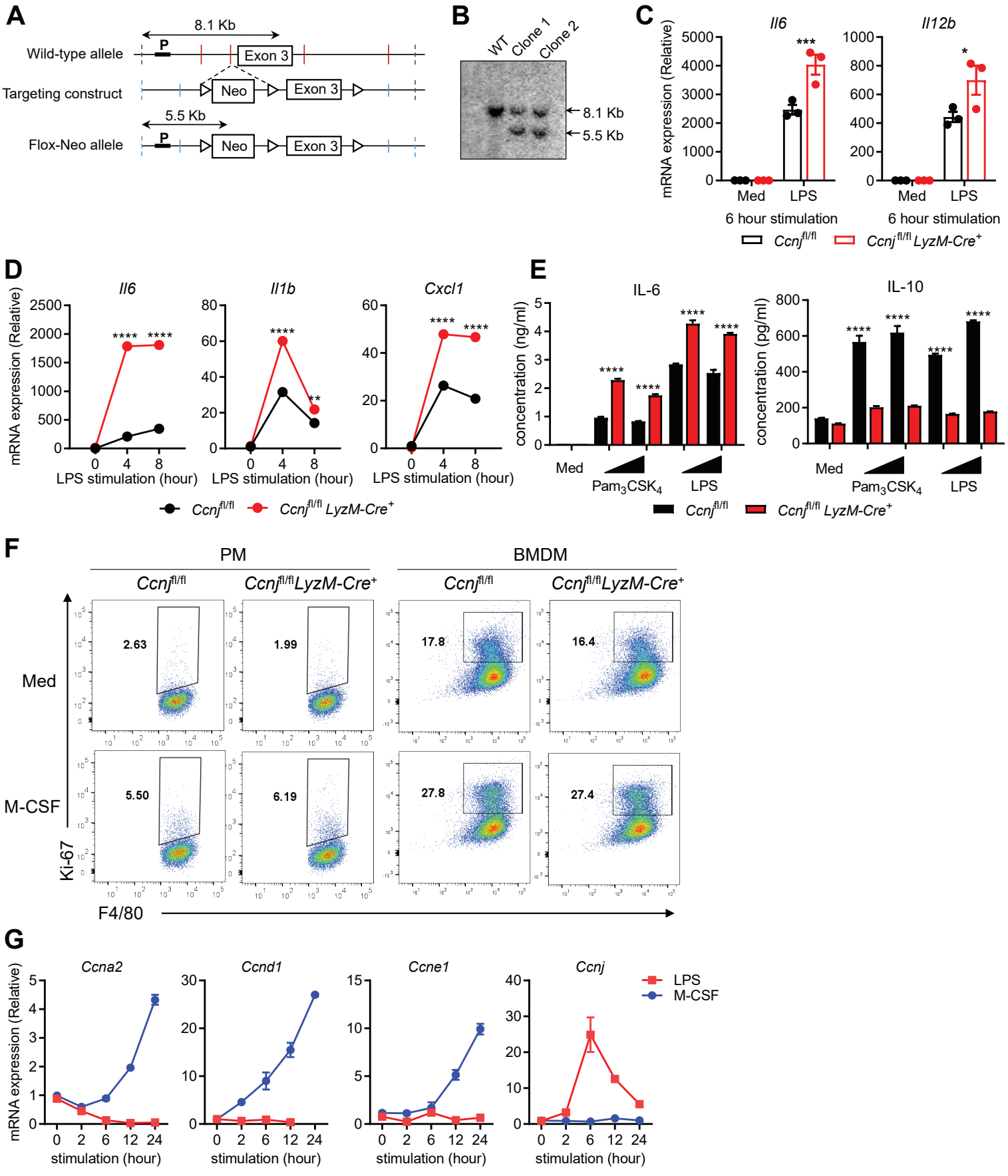
A
8.1 Kb
Wild-type allele
P
Exon 3
Targeting construct
Neo
Exon 3
5.5 Kb
Flox-Neo allele
P
Neo
Exon 3
B
WT
Clone 1
Clone 2
8.1 Kb
5.5 Kb
C
Il6
Il12b
mRNA expression (Relative)
Med
LPS
6 hour stimulation
Ccnj fl/fl
Ccnj fl/fl LyzM-Cre+
D
Il6
Il1b
Cxcl1
mRNA expression (Relative)
LPS stimulation (hour)
Ccnj fl/fl
Ccnj fl/fl LyzM-Cre+
E
IL-6
IL-10
concentration (ng/ml)
concentration (pg/ml)
Med
Pam3CSK4
LPS
Ccnj fl/fl
Ccnj fl/fl LyzM-Cre+
F
PM
BMDM
Ccnj fl/fl
Ccnj fl/fl LyzM-Cre+
Med
M-CSF
2.63
1.99
17.8
16.4
5.50
6.19
27.8
27.4
Ki-67
F4/80
G
Ccna2
Ccnd1
Ccne1
Ccnj
mRNA expression (Relative)
stimulation (hour)
LPS
M-CSF

Figure S4

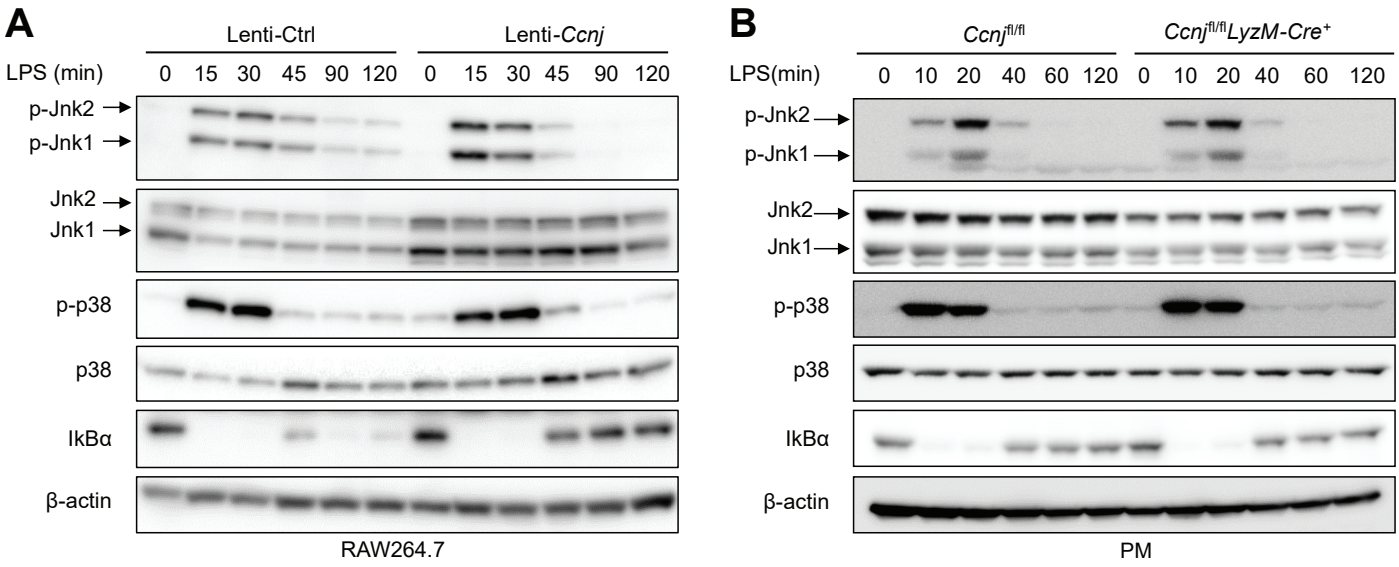
A
Lenti-Ctrl
Lenti-Ccnj
LPS (min)
0 15 30 45 90 120 0 15 30 45 90 120
p-Jnk2
p-Jnk1
Jnk2
Jnk1
p-p38
p38
IkBα
β-actin
RAW264.7
B
Ccnj fl/fl
Ccnj fl/fl LyzM-Cre+
LPS(min)
0 10 20 40 60 120 0 10 20 40 60 120
p-Jnk2
p-Jnk1
Jnk2
Jnk1
p-p38
p38
IkBα
β-actin
PM

Figure S5

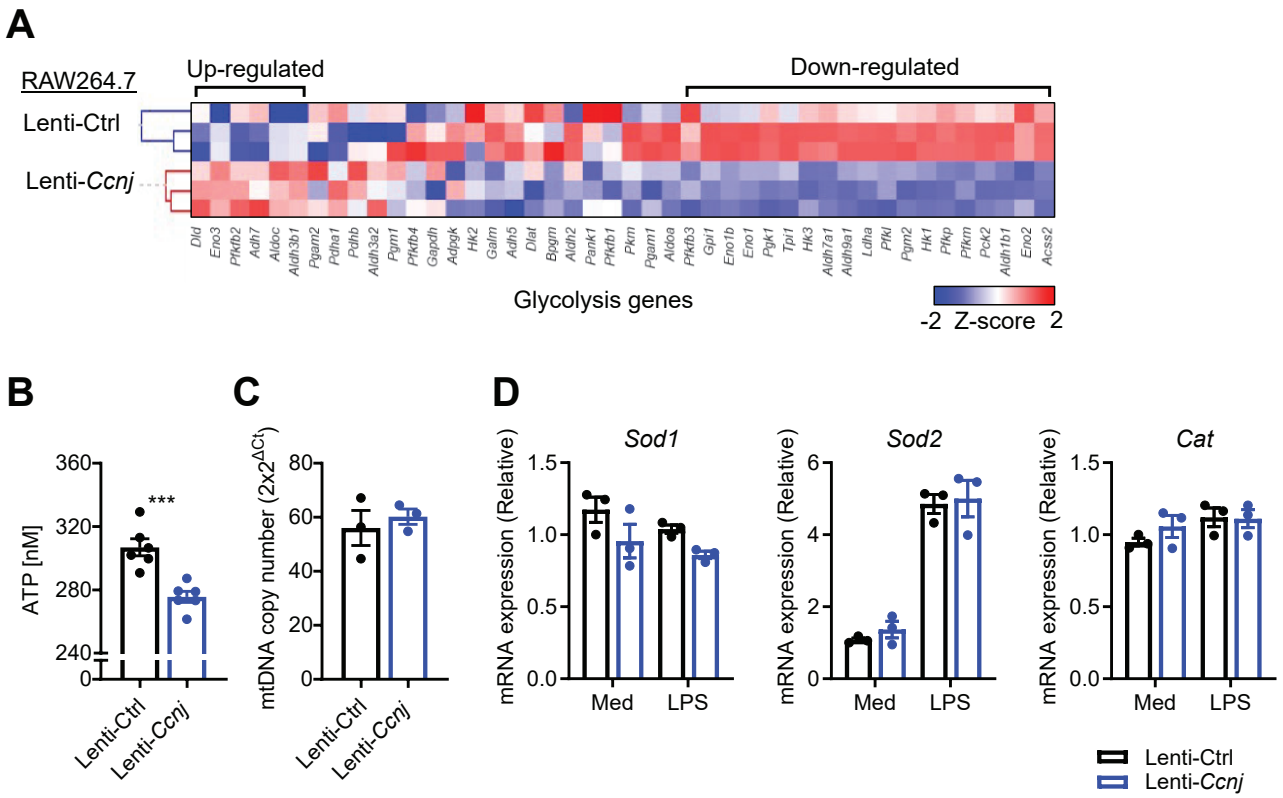
A
RAW264.7
Up-regulated
Down-regulated
Lenti-Ctrl
Lenti-Ccnj
Dld Eno3 Pfkfb2 Adh7 Aldoc Aldh3b1 Pgam2 Pdha1 Pdhb Aldh3a2 Pgm1 Pfkfb4 Gapdh Adpgk Hk2 Galm Adh5 Dlat Bpgm Aldh2 Pank1 Pfkfb1 Pkm Pgam1 Aldoa Pfkfb3 Gpi1 Eno1b Eno1 Pgk1 Tpi1 Hk3 Aldh7a1 Aldh9a1 Ldha Pfkl Pgm2 Hk1 Pfkp Pfkm Pck2 Aldh1b1 Eno2 Acss2
Glycolysis genes
-2 Z-score 2
B
ATP [nM]
360
320
280
240
0
***
Lenti-Ctrl
Lenti-Ccnj
C
mtDNA copy number (2x2^ΔCt)
80
60
40
20
0
Lenti-Ctrl
Lenti-Ccnj
D
Sod1
Sod2
Cat
mRNA expression (Relative)
1.5
1.0
0.5
0.0
6
4
2
0
Med
LPS
Lenti-Ctrl
Lenti-Ccnj

Figure S6

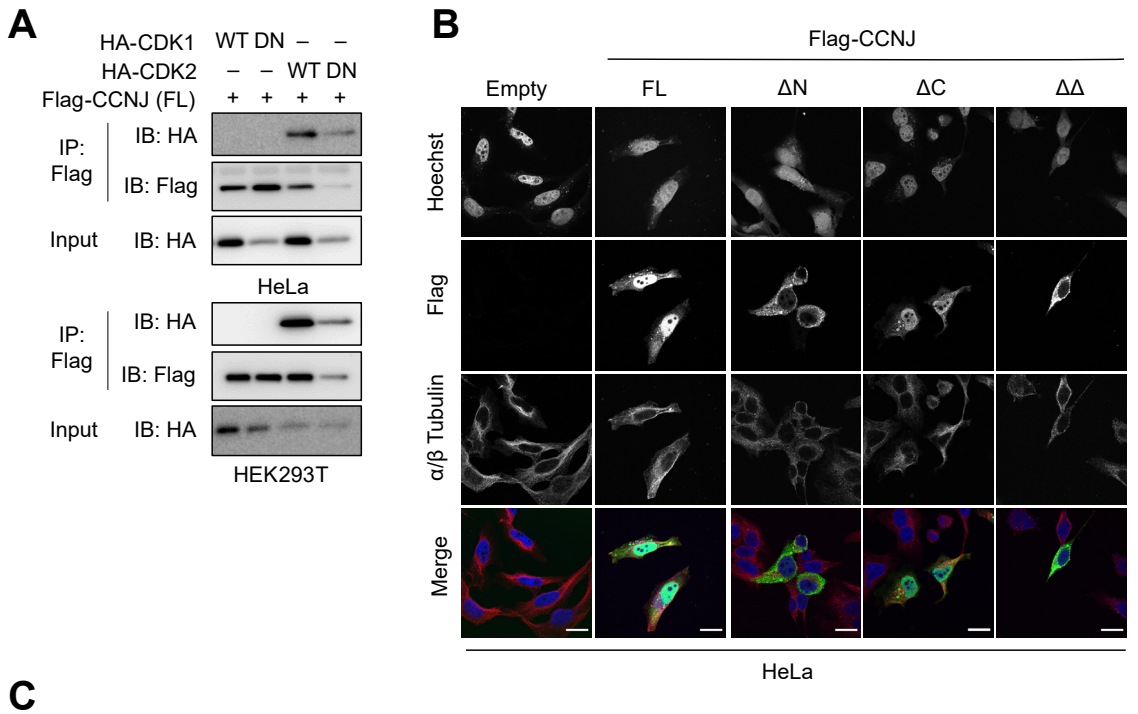
A
HA-CDK1 WT DN – –
HA-CDK2 – – WT DN
Flag-CCNJ (FL) + + + +
IP: Flag
IB: HA
IB: Flag
Input
IB: HA
HeLa
IP: Flag
IB: HA
IB: Flag
Input
IB: HA
HEK293T
B
Flag-CCNJ
Empty
FL
ΔN
ΔC
ΔΔ
Hoechst
Flag
α/β Tubulin
Merge
HeLa

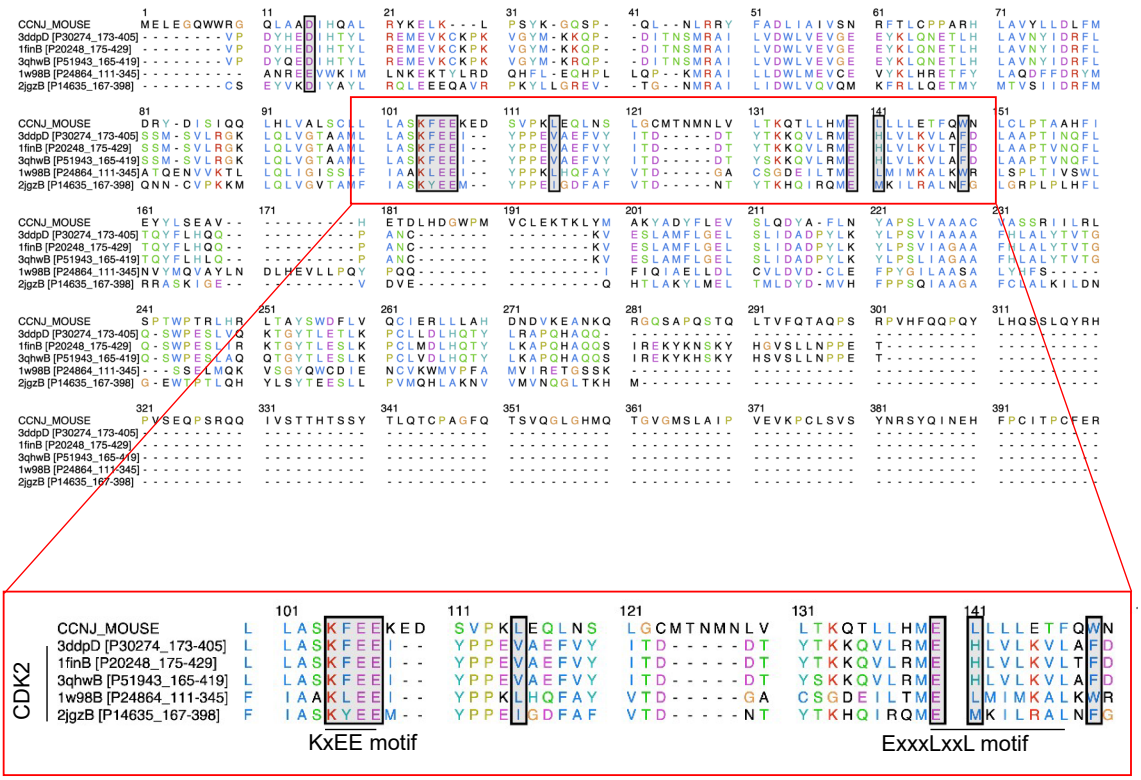
C
CDK2
CCNJ_MOUSE
3ddpD [P30274_173-405]
1finB [P20248_175-429]
3qhwB [P51943_165-419]
1w98B [P24864_111-345]
2jgzB [P14635_167-398]
KxEE motif
ExxxLxxL motif

Figure S7

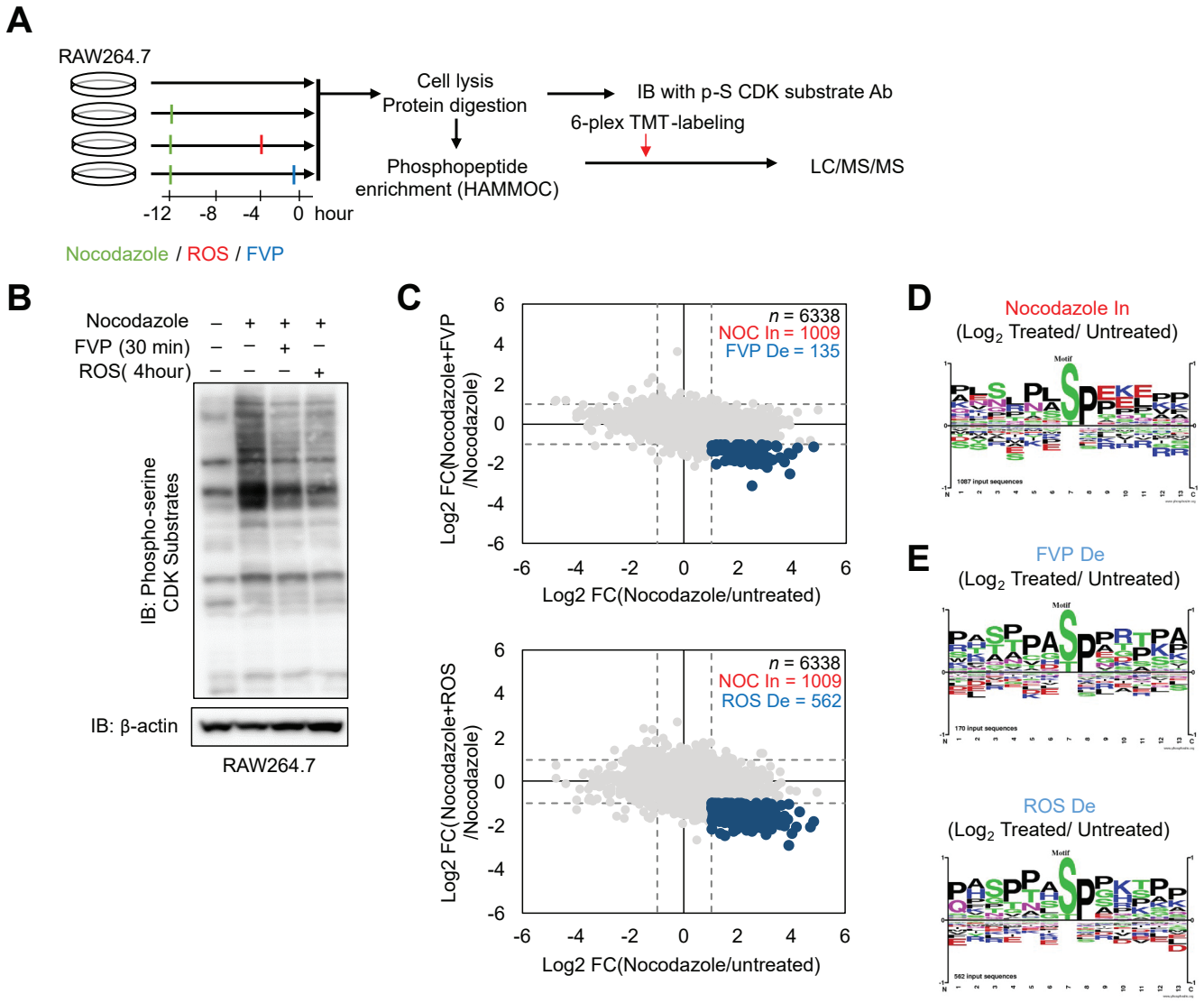
A
RAW264.7
-12
-8
-4
0 hour
Cell lysis
Protein digestion
Phosphopeptide
enrichment (HAMMOC)
IB with p-S CDK substrate Ab
6-plex TMT-labeling
LC/MS/MS
Nocodazole / ROS / FVP
B
Nocodazole – + + +
FVP (30 min) – – + –
ROS(4hour) – – – +
IB: Phospho-serine
CDK Substrates
IB: β-actin
RAW264.7
C
n = 6338
NOC In = 1009
FVP De = 135
Log2 FC(Nocodazole+FVP
/Nocodazole)
Log2 FC(Nocodazole/untreated)
n = 6338
NOC In = 1009
ROS De = 562
Log2 FC(Nocodazole+ROS
/Nocodazole)
Log2 FC(Nocodazole/untreated)
D
Nocodazole In
(Log2 Treated/ Untreated)
Motif
1087 input sequences
E
FVP De
(Log2 Treated/ Untreated)
Motif
170 input sequences
ROS De
(Log2 Treated/ Untreated)
Motif
562 input sequences

Figure S8

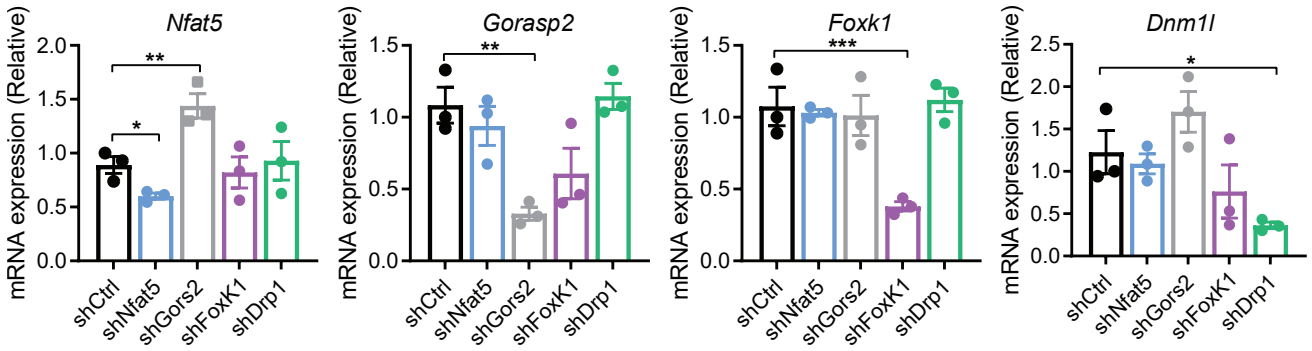
Nfat5
Gorasp2
Foxk1
Dnm1l
mRNA expression (Relative)
shCtrl
shNfat5
shGors2
shFoxK1
shDrp1

Figure S9

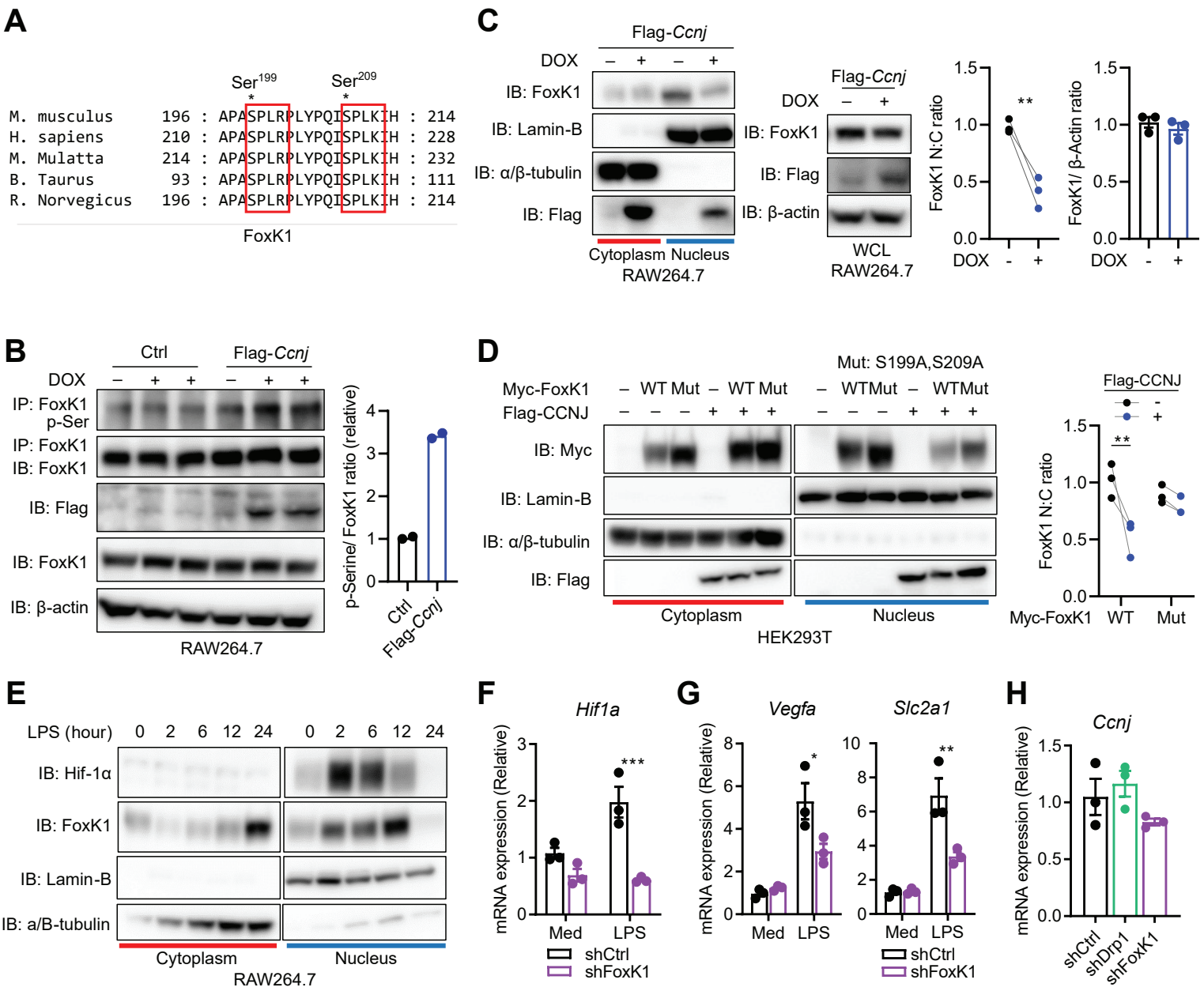
A
Ser199
Ser209
M. musculus 196 : APASPLRPLYPQISPLKIH : 214
H. sapiens 210 : APASPLRPLYPQISPLKIH : 228
M. Mulatta 214 : APASPLRPLYPQISPLKIH : 232
B. Taurus 93 : APASPLRPLYPQISPLKIH : 111
R. Norvegicus 196 : APASPLRPLYPQISPLKIH : 214
FoxK1
B
Ctrl
Flag-Ccnj
DOX
IP: FoxK1 p-Ser
IP: FoxK1
IB: FoxK1
IB: Flag
IB: FoxK1
IB: β-actin
RAW264.7
p-Serine/ FoxK1 ratio (relative)
Ctrl
Flag-Ccnj
C
Flag-Ccnj
DOX
IB: FoxK1
IB: Lamin-B
IB: α/β-tubulin
IB: Flag
Cytoplasm Nucleus
RAW264.7
IB: FoxK1
IB: Flag
IB: β-actin
WCL
RAW264.7
FoxK1 N:C ratio
FoxK1/ β-Actin ratio
D
Mut: S199A,S209A
Myc-FoxK1
Flag-CCNJ
IB: Myc
IB: Lamin-B
IB: α/β-tubulin
IB: Flag
Cytoplasm
Nucleus
HEK293T
Flag-CCNJ
FoxK1 N:C ratio
Myc-FoxK1 WT Mut
E
LPS (hour) 0 2 6 12 24 0 2 6 12 24
IB: Hif-1α
IB: FoxK1
IB: Lamin-B
IB: a/B-tubulin
Cytoplasm
Nucleus
RAW264.7
F
Hif1a
mRNA expression (Relative)
Med LPS
shCtrl
shFoxK1
G
Vegfa
Slc2a1
mRNA expression (Relative)
Med LPS
shCtrl
shFoxK1
H
Ccnj
mRNA expression (Relative)
shCtrl
shDrp1
shFoxK1

Figure S10

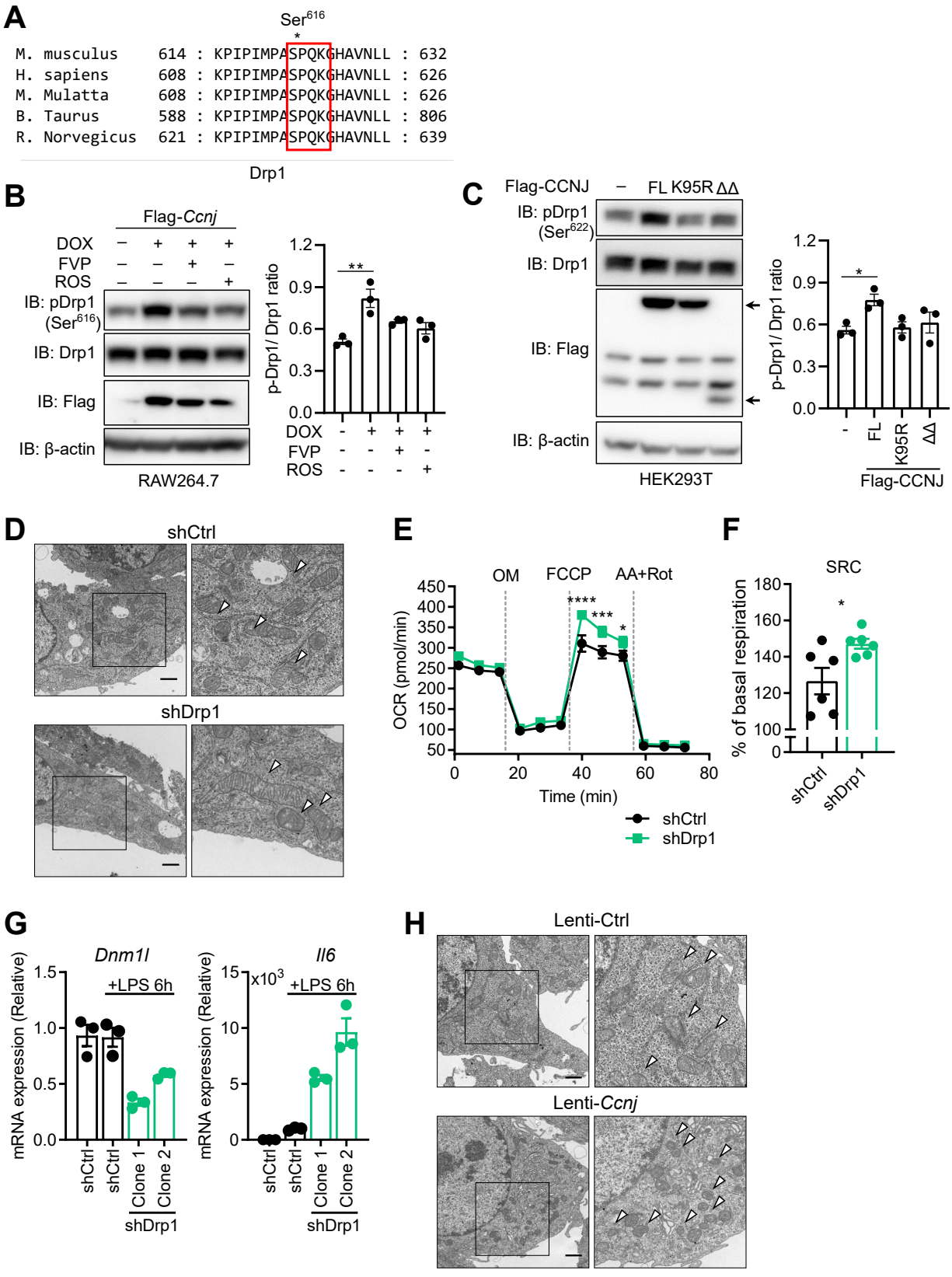
A
Ser616
M. musculus 614 : KPIPIMPASPQKGHAVNLL : 632
H. sapiens 608 : KPIPIMPASPQKGHAVNLL : 626
M. Mulatta 608 : KPIPIMPASPQKGHAVNLL : 626
B. Taurus 588 : KPIPIMPASPQKGHAVNLL : 806
R. Norvegicus 621 : KPIPIMPASPQKGHAVNLL : 639
Drp1
B
Flag-Ccnj
DOX
FVP
ROS
IB: pDrp1 (Ser616)
IB: Drp1
IB: Flag
IB: β-actin
RAW264.7
p-Drp1/ Drp1 ratio
C
Flag-CCNJ
FL K95R ΔΔ
IB: pDrp1 (Ser622)
IB: Drp1
IB: Flag
IB: β-actin
HEK293T
p-Drp1/ Drp1 ratio
Flag-CCNJ
D
shCtrl
shDrp1
E
OM
FCCP
AA+Rot
OCR (pmol/min)
Time (min)
shCtrl
shDrp1
F
SRC
% of basal respiration
G
Dnm1l
+LPS 6h
mRNA expression (Relative)
Il6
x10^3
Clone 1
Clone 2
H
Lenti-Ctrl
Lenti-Ccnj

Figure S11

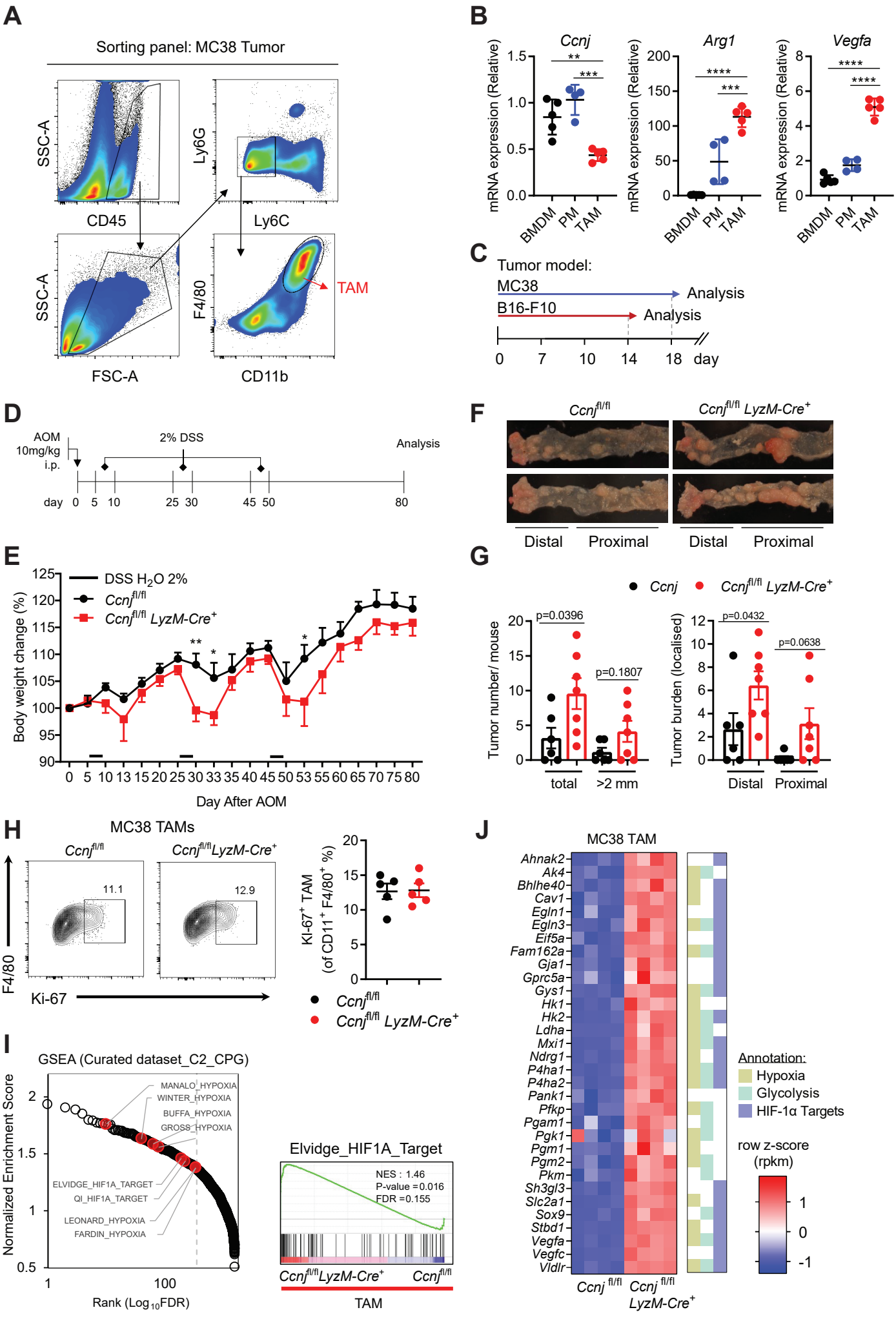
A
Sorting panel: MC38 Tumor
SSC-A
CD45
Ly6G
Ly6C
SSC-A
FSC-A
F4/80
CD11b
TAM
B
Ccnj
Arg1
Vegfa
mRNA expression (Relative)
BMDM
PM
TAM
C
Tumor model:
MC38
Analysis
B16-F10
Analysis
0 7 10 14 18 day
D
AOM
10mg/kg
i.p.
2% DSS
Analysis
day 0 5 10 25 30 45 50 80
E
DSS H2O 2%
Ccnj fl/fl
Ccnj fl/fl LyzM-Cre+
Body weight change (%)
Day After AOM
F
Ccnj fl/fl
Ccnj fl/fl LyzM-Cre+
Distal
Proximal
G
Ccnj
Ccnj fl/fl LyzM-Cre+
Tumor number/ mouse
p=0.0396
p=0.1807
total
>2 mm
Tumor burden (localised)
p=0.0432
p=0.0638
Distal
Proximal
H
MC38 TAMs
Ccnj fl/fl
Ccnj fl/fl LyzM-Cre+
11.1
12.9
F4/80
Ki-67
KI-67+ TAM
(of CD11+ F4/80+ %)
Ccnj fl/fl
Ccnj fl/fl LyzM-Cre+
I
GSEA (Curated dataset_C2_CPG)
Normalized Enrichment Score
MANALO_HYPOXIA
WINTER_HYPOXIA
BUFFA_HYPOXIA
GROSS_HYPOXIA
ELVIDGE_HIF1A_TARGET
QI_HIF1A_TARGET
LEONARD_HYPOXIA
FARDIN_HYPOXIA
Rank (Log10FDR)
Elvidge_HIF1A_Target
NES : 1.46
P-value =0.016
FDR =0.155
Ccnj fl/fl LyzM-Cre+
Ccnj fl/fl
TAM
J
MC38 TAM
Ahnak2
Ak4
Bhlhe40
Cav1
Egln1
Egln3
Eif5a
Fam162a
Gja1
Gprc5a
Gys1
Hk1
Hk2
Ldha
Mxi1
Ndrg1
P4ha1
P4ha2
Pank1
Pfkp
Pgam1
Pgk1
Pgm1
Pgm2
Pkm
Sh3gl3
Slc2a1
Sox9
Stbd1
Vegfa
Vegfc
Vldlr
Ccnj fl/fl
Ccnj fl/fl LyzM-Cre+
Annotation:
Hypoxia
Glycolysis
HIF-1α Targets
row z-score
(rpkm)

Table S1. Mass Spectrometry analysis for cyclin J–interacting proteins

NCBI protein database

Band 1 (size : 43kDa)		
Identified protein	**Score**	**# of peptides**
cyclin-J isoform 1 [Homo sapiens]	1305	124
Chain B, Electron Cryo-microscopy Of Dngr-1 In Complex With F-actin	782	75
phosphoglycerate kinase 1 [Homo sapiens]	674	54
Chain B, Crystal Structure Of A Complex Of Sse1p And Hsp70, Selenomethionine- Labeled Crystals	567	42
creatine kinase [Homo sapiens]	404	33
actin, alpha skeletal muscle [Homo sapiens]	391	56
PREDICTED: cyclin-J isoform X2 [Homo sapiens]	325	59
NF45 protein [Homo sapiens]	324	28
phosphoglycerate kinase 2 [Homo sapiens]	207	13
Chain A, Structure Of T255e, E376g Mutant Of Human Medium Chain Acyl- CoA Dehydrogenase	153	15
Band 2 (size : 34kDa)		
Identified protein	**Score**	**# of peptides**
Chain A, Phosphorylated Cyclin-Dependent Kinase-2 Bound To Cyclin A	1424	216
Chain A, Crystal Structure Of Human Cyclin-dependent Kinase 2 Complexed With A Nucleoside Inhibitor	1424	216
cdk2 [Homo sapiens]	1424	214
cyclin-dependent kinase 1 isoform 1 [Homo sapiens]	1338	181
d-HSCDK2 [Homo sapiens]	823	144
14-3-3 protein epsilon [Homo sapiens]	618	69
cyclin-dependent kinase 3 [Homo sapiens]	547	60
orf [Homo sapiens]	120	17
cyclin-dependent-like kinase 5 isoform 1 [Homo sapiens]	93	20
cyclin-dependent kinase 6 [Homo sapiens]	92	16

Table S2. List of primer sequences used for RT-qPCR in this paper.

No	Name	Origin	Forward primer	Reverse primer
1	*Il6*	mouse	GTAGCTATGGTACTCCAGAAGAC	ACGATGATGCACTTGCAGAA
2	*Il10*	mouse	CTATGCTGCCTGCTCTTACTG	AACCCAAGTAACCCTTAAAGTC
3	*Cxcl10*	mouse	ACTGCATCCATATCGATGAC	TTCATCGTGGCAATGATCTC
4	*Tnf*	mouse	CCCTCACACTCAGATCATCTTCT	GCTACGACGTGGGCTACAG
5	*Ifnb1*	mouse	CAGCTCCAAGAAAGGACGAAC	GGCAGTGTAACTCTTCTGCAT
6	*18s*	mouse	CGGACAGGATTGACAGATTG	CAAATCGCTCCACCAACTAA
7	*Il1b*	mouse	GCAACTGTTCCTGAACTCAACT	ATCTTTTGGGGTCCGTCAACT
8	*Ifng*	mouse	TGAGTATTGCCAAGTTTGAGGTCA	CGGCAACAGCTGGTGGAC
9	*Hif1a*	mouse	AATACATTTTCTCTGCCAGTTTTCTG	TTGCTGCATCTCTAGACTTTTCTTTT
10	*Il23a*	mouse	GACCCACAAGGACTCAAGGAC	ATGGGCTATCAGGGAGTAGAG
11	*Cxcl1*	mouse	CTGCACCCAAACCGAAGTC	AGCTTCAGGGTCAAGGCAAG
12	*Arg1*	mouse	CCACAGTCTGGCAGTTGGAAG	GGTTGTCAGGGGAGTGTTGATG
13	*Fizz1*	mouse	CCTGCTGGGATGACTGCTA	TGGGTTCTCCACCTCTTCAT
14	*Mgl1*	mouse	CAGAATCGCTTAGCCAATGTGG	TCCCAGTCCGTGTCCGAAC
15	*Mgl2*	mouse	TTCAAGAATTGGAGGCCACT	CAGACATCGTCATTCCAACG
16	*Vegfa*	mouse	CCACGACAGAAGGAGAGCAGAAGTCC	CGTTACAGCAGCCTGCACAGCG
17	*Ym1*	mouse	GCCACTGAGGTCTGGGATGC	TCCTTGAGCCACTGAGCCTTC
18	*Mmp9*	mouse	TAAGGACGGCAAATTTGGTT	CTTTAGTGGTGCAGGCAGAG
19	*Trp53*	mouse	CCCCGCAAAAGAAAAAACCAC	AGCTGGAGTGAGCCCTGC
20	*Mdm2*	mouse	TTAGTGGCTGTAAGTCAGCAAGA	CCTTCAGATCACTCCCACCT
21	*Mcm6*	mouse	CCTGTGAATAGGTTCAACGGC	CATTTTCCTGAGGTGGAGCAC
22	*Rb1*	mouse	AAACAGAGAGAACGCCACGA	ACTGGAGTGTGTGGAGTAACC
23	*E2f1*	mouse	GCCCTTGACTATCACTTTGGTCTC	CCTTCCCATTTTGGTCTGCTC
24	*E2f4*	mouse	CTTCTACCTCCTTTGAGCCCATC	TCACAGACACCTTCACTCTCGTCC
25	*Isg15*	mouse	TGACTGTGAGAGCAAGCAGC	CCCCAGCATCTTCACCTTTA
26	*Cxcl9*	mouse	CCGAGGCACGATCCACTACA	CGAGTCCGGATCTAGGCAGGT
27	*Ciita*	mouse	CCCTGCGTGTGATGGATGTC	ATCTCAGACTGATCCTGGCAT
28	*Csf1r*	mouse	TGTCATCGAGCCTAGTGGC	CGGGAGATTCAGGGTCCAAG
29	*Pkm2*	mouse	GCCGCCTGGACATTGACTC	CCATGAGAGAAATTCAGCCGAG
30	*Ldha*	mouse	CATTGTCAAGTACAGTCCACACT	TTCCAATTACTCGGTTTTTGGGA
31	*Pfkfb3*	mouse	CCCAGAGCCGGGTACAGAA	GGGGAGTTGGTCAGCTTCG
32	*Slc2a1*	mouse	CAGTTCGGCTATAACACTGGTG	GCCCCCGACAGAGAAGATG
33	*Hk2*	mouse	TGATCGCCTGCTTATTCACGG	AACCGCCTAGAAATCTCCAGA
34	*Pfkl*	mouse	GGAGGCGAGAACATCAAGCC	CGGCCTTCCCTCGTAGTGA

35	*Pgk1*	mouse	ATGTCGCTTTCCAACAAGCTG	GCTCCATTGTCCAAGCAGAAT
36	*Ccna2*	mouse	CTTCTTCCTTTTCCCTTGGC	TTTCAGAGTCCCAGTGACCC
37	*Ccnd1*	mouse	GTTCATTTCCAACCCACCCTC	AGAAAGTGCGTTGTGCGGTAG
38	*Ccne1*	mouse	AGCGAGGATAGCAGTCAGCC	GGTGGTCTGATTTTCCGAGG
39	*Ccnj*	mouse	AGCTGAAGCTGCCTTCTTAC	CTGAATGGAGATGTCATAGC
40	*Ccnb1*	mouse	AAAGGGAAGCAAAAACGCTAGG	TGTTCAAGTTCAGGTTCAGGCTC
41	*Foxk1*	mouse	AAGAACGGCGTCTTCGTGG	TGGGGCCTCCTCTTTATGGTA
42	*Nfat5*	mouse	CAGCGCCCAATAGTTGGCA	TGCTGGTGAAAAATTGACTGGT
43	*Gorasp2*	mouse	GTTCTCAGTACAGGCGTACC	TGTGGTAGCTGGGTTCATTG
44	*Dnm1l*	mouse	GGGCACTTAAATTGGGCTCC	TGTATTCTGTTGGCGTGGAAC
45	*Pecam-1*	mouse	ATGGAAAGCCTGCCATCATG	TCCTTGTTGTTCAGCATCAC
46	*MT-COX1*	mouse	GCCCCAGATATAGCATTCCC	GTTCATCCTGTTCCTGCTCC
47	*MT-COX2*	mouse	ATAACCGAGTCGTTCTGCCAAT	TTTCAGAGCATTGGCCATAGAA
48	*MT-ND3*	mouse	AAGCAAATCCATATGAATGCGG	GCTCATGGTAGTGGAAGTAGAAG
49	*Sod1*	mouse	GGAACCATCCACTTCGAGCA	CCCATGCTGGCCTTCAGTTA
50	*Sod2*	mouse	AGGAGAAGTACCACGAGGCT	GCAGGCAGCAATCTGTAAGC
51	*Cat*	mouse	AGCGACCAGATGAAGCAGTG	TCCGCTCTCTGTCAAAGTGTG
52	*CCNA2*	human	GAAACTGCAGCTCGTAGGAA	ACTTTCAGAAGCAAGTGTTCCA
53	*CCNE1*	human	AGCACTTTCTTGAGCAACACC	CGCCATATACCGGTCAAAGA
54	*CCNJ*	human	TGCGCTTTCCTGCCTGCTTC	AGGCTGTTGAGCTGCTCCAG

Table S3. List of shRNA oligonucleotide sequences used in this paper.

No	Name	Targeting gene	Origin	ID	Sequence
1	scramble	Non-targeting		SHC002	CAACAAGATGAAGAGCACCAA
2	shFoxK1	*Foxk1*	RNAi Consortium	TRCN0000085686	GATCCAGTTCACATCGCTATA
3	shDrp1	*Dnm1l*	RNAi Consortium	TRCN0000321170	CTATAATGCATGCACTATTTA
4	shNfat5	*Nfat5*	RNAi Consortium	TRCN0000229557	TGCGGACAGTATCCGGTTAAA
5	shGors2	*Gorasp2*	RNAi Consortium	TRCN0000077520	GCTATGGTTATTTGCACCGAA

Data file S1. Transcriptomic analysis of RAW264.7 cells stably expressing cyclin J. The RNA-seq data is provided as an Excel file.

Data file S2. Phosphoproteomic analysis of RAW264.7 cells under nocodazole treatment with or without CDK inhibitors. This data is provided as an Excel file.

Data file S3. Proteomic analysis of cyclin J doxycycline-inducible RAW264.7 cells. This data is provided as an Excel file.

Data file S4. Phosphoproteomic analysis of cyclin J doxycycline-inducible RAW264.7 cells. This data is provided as an Excel file.

Data file S5. Transcriptomic analysis of tumor-associated macrophages from *Ccnj*$^{fl/fl}$LyzM-Cre^{+} mice. The RNA-seq data is provided as an Excel file.